

# Wave dissipation in a permeable structure

Experimental research on the physical processes causing energy dissipation inside an array of cylinders

W.J. Jansen



# Wave dissipation in a permeable structure

Experimental research on the physical processes causing energy dissipation inside an array of cylinders

by

W.J. Jansen

in partial fulfillment of the requirements for the degree of

**Master of Science**  
in Civil Engineering

at the Delft University of Technology,  
to be defended publicly on Wednesday, October 30, 2019 at 16:00.

Student number: 4313151  
Project duration: September 25, 2018 – October 30, 2019  
Thesis committee: Prof. dr. ir. W. S. J. Uijtewaal, Delft University of Technology, Chairman  
Ir. A. Gijón Mancheño, Delft University of Technology, Supervisor  
Ir. E. E. Sirks, Witteveen + Bos, Supervisor  
Ing. C. Kuiper, Delft University of Technology  
Dr.ir. R. C. Lanzafame, Delft University of Technology  
Prof. dr. ir. J. C. Winterwerp, Delft University of Technology

An electronic version of this thesis is available at <http://repository.tudelft.nl/>.



# Preface

With the finalizing of this thesis, also my time of studying in Delft comes to an end. It was a great time of 6 years, in which I have learned a lot and had many great opportunities. Learning from my fellow students in group exercises, travelling to Colombia to perform a multidisciplinary project and having the possibility to have a look inside the company of Witteveen + Bos during my graduation project. Looking back at the journey of my study and this research, I want to thank some people who made it possible.

First of all, I want to thank the members of my graduation committee, who each had his or her own contribution to the process and final product. I would like to thank Prof. Uijtewaal, for his guidance during the progress meetings and the startup of this research. I also want to thank Alejandra Gijón Mancheño, who was my daily supervisor during my research. As it was part of your PhD research, we spent many hours discussing about the set up of the experiments, the approach and the results. Thank you for all the time and effort you put into it, it really improved the quality of this report. I wish you all the best with processing the remaining part of the data and finishing your research. I also want to thank Emma Sirks, for introducing me to Witteveen + Bos, inviting me for all the activities and your critical feedback on the report.

Another group of people I want to thank is the personnel of the fluid mechanics lab: Sander, Pieter, Frank, Jaap, Arno and Rob. Thank you for always trying to get the best results possible, for always making time if changes were required and for helping me with taking the model in and out of the flume an endless number of times.

Furthermore, I want to thank my family and friends for supporting and motivating me during the whole study, it made it a lot more fun. Especially I want to thank my parents, who always had faith in a good result and supported me unconditionally.

*W.J. Jansen  
Delft, October 2019*



# Abstract

Mangrove forests, which serve as a natural sea defence, have been degraded by human action during the last decades. To protect and recover these areas, different types of permeable structures consisting of bamboo have been proposed and applied. However, these structures are currently based on engineering judgement, as design rules are not available. The goal of this research is to make a step forward in the design optimization of permeable structures and gain a better understanding of the processes causing the wave dissipation inside the structure.

In this study, scale experiments are conducted in the wave flume at Delft University of Technology. An array of aluminum cylinders is used as a schematization of the structure, with an element diameter of  $4\text{cm}$  and a minimum spacing of  $2\text{cm}$ . The tested wave height is  $0.13\text{m}$ , with a water depth of  $0.6\text{m}$  for the first set of experiments. These experiments evaluated wave transformation through a selected number of configurations. The water depth was  $0.55\text{m}$  for the second set, where the velocities and forces were also measured inside the structure. As the applied wave periods are short ( $T = 1 - 2\text{s}$ ), the tested wave conditions are in the range of small  $KC$ -numbers ( $4 < KC < 13$ ).

The first part of this research focuses on effect of different configurations and arrangements on the amount of energy dissipation, by measuring the incoming and reflected wave heights in front of and behind the structure. For the short waves, the horizontal arrangements dissipate more energy, as energy is dissipated by both the vertical and horizontal drag forces. However, the effect diminishes with increasing wave period. Considering the total dissipation and the amount of dissipation per element, the placement of the elements in rows perpendicular to the direction of wave propagation is found to be the most effective.

To study the effect of the element diameter on the dissipation, the results are compared with previous research by Haage (2018) on a model with a diameter and spacing of  $2\text{cm}$ . As with the change in diameter also the structure porosity changed, a direct comparison was not possible and a comparison based on a simplified drag coefficient is done. No direct effect of the diameter is observed, as the obtained drag coefficients show the same trend and magnitude when plotted against an adapted Keulegan-Carpenter number ( $KC^*$ ), which is based on the element spacing instead of diameter. Small  $KC^*$ -numbers result in large drag coefficients, which decrease when  $KC^*$  increases.

The second part of this research focuses on the processes inside the structure that cause the energy dissipation. A force and velocity sensor are applied at three locations inside the structure in separate experiments, to determine the relation of the force and velocity inside the structure with the undisturbed values. Two methods are applied for the analysis, based on two different principles. Method 1 is based on the assumption of a constant pair of force coefficients and an increase in velocity inside the structure, method 2 is based on the assumption of a constant velocity and an increase in force coefficients inside the structure. By comparing both methods, it is found that an increase in velocity is the most important factor for the increase in drag force, which is the driving factor for the energy dissipation. It is also found that the amplification factor for the velocity is dependent on both the structure porosity and frontal porosity.



# Contents

<b>Preface</b>	<b>iii</b>
<b>Abstract</b>	<b>v</b>
<b>List of Figures</b>	<b>xi</b>
<b>List of Tables</b>	<b>xv</b>
<b>List of Symbols</b>	<b>xvii</b>
<b>1 Introduction</b>	<b>1</b>
1.1 Problem description . . . . .	1
1.2 Research goal . . . . .	5
1.3 Research question . . . . .	5
1.4 Scope and approach . . . . .	6
1.5 Reading guide . . . . .	7
<b>2 Theoretical background</b>	<b>9</b>
2.1 Application of permeable structures . . . . .	9
2.2 Wave action . . . . .	10
2.2.1 Wave characteristics . . . . .	10
2.2.2 Waves around a single cylinder . . . . .	11
2.2.3 Waves through an array of cylinders . . . . .	17
2.3 Previous experiments on wave dissipation . . . . .	20
2.4 Reference situation in the Demak region, Indonesia . . . . .	20
2.4.1 Hydrodynamic conditions . . . . .	20
2.4.2 Applied structures . . . . .	22
<b>3 Methodology: First set of experiments</b>	<b>25</b>
3.1 Set-up physical model . . . . .	25
3.1.1 Set-up wave flume . . . . .	25
3.1.2 Model dimensions . . . . .	25
3.1.3 Model configurations . . . . .	27
3.2 Wave conditions . . . . .	28
3.3 Data gathering . . . . .	29
3.4 Data processing . . . . .	30
3.4.1 Dissipation . . . . .	30
3.4.2 Computation interval . . . . .	30
3.4.3 Drag coefficient calibration from wave energy dissipation . . . . .	32
<b>4 Results: First set of experiments</b>	<b>33</b>
4.1 Energy balance . . . . .	33
4.2 Relationship between configuration and dissipation . . . . .	34
4.2.1 Total dissipation . . . . .	34
4.2.2 Dissipation per element . . . . .	36
4.2.3 Drag coefficient by Dalrymple . . . . .	37
4.3 Influence of element diameter . . . . .	38
4.3.1 Total dissipation vs. KC number (element diameter) . . . . .	38
4.3.2 Drag coefficient vs. KC number (element diameter) . . . . .	38
4.3.3 Drag coefficient vs. KC number (element spacing) . . . . .	39
4.3.4 Drag coefficient per configuration . . . . .	40

<b>5</b>	<b>Analysis of the results: First set</b>	<b>41</b>
5.1	Analysis of wave signal . . . . .	41
5.2	Effect of configuration on the dissipation . . . . .	42
5.2.1	Increasing the structure width . . . . .	42
5.2.2	Changing the orientation of the elements . . . . .	43
5.2.3	Changing the positions of the elements . . . . .	44
5.3	Effect of diameter . . . . .	46
5.4	Executive summary . . . . .	47
<b>6</b>	<b>Methodology: Second set of experiments</b>	<b>49</b>
6.1	Set-up . . . . .	49
6.1.1	Data gathering . . . . .	49
6.1.2	Model configurations . . . . .	50
6.2	Wave conditions . . . . .	51
6.3	Data processing . . . . .	51
6.3.1	Filtering of the measured signals . . . . .	52
6.3.2	Computation of the velocity profile over depth . . . . .	53
6.3.3	Computation of the force coefficients . . . . .	54
6.3.4	Asymmetry in velocity signal . . . . .	55
6.4	Approach with 2 methods . . . . .	56
<b>7</b>	<b>Results: Second set of experiments</b>	<b>57</b>
7.1	Presentation of the results . . . . .	57
7.2	Effects of increasing the number of rows . . . . .	58
7.2.1	Dissipation . . . . .	58
7.2.2	Velocity . . . . .	58
7.2.3	Force . . . . .	59
7.3	Effect of location in the model . . . . .	60
7.3.1	Velocity . . . . .	60
7.3.2	Force . . . . .	60
7.4	Results method 1 - Calibration from dissipation . . . . .	61
7.5	Results method 2 - Calibration from forces . . . . .	62
<b>8</b>	<b>Analysis of the results: Second set</b>	<b>65</b>
8.1	Dissipation and transmission . . . . .	65
8.1.1	Wave transmission . . . . .	67
8.2	Velocity and force signal . . . . .	68
8.2.1	Mean negative current . . . . .	68
8.2.2	Amplification factors for the velocity . . . . .	68
8.2.3	Amplification factor for the force . . . . .	69
8.3	Colour convention . . . . .	70
8.4	Method 1 - Calibration from dissipation . . . . .	71
8.4.1	Amplification factor for the velocity . . . . .	71
8.4.2	Cross-check: predicted forces . . . . .	72
8.5	Method 2 - Calibration from forces . . . . .	73
8.5.1	Force coefficients . . . . .	73
8.5.2	Velocity signal . . . . .	75
8.5.3	Cross-check: predicted energy dissipation . . . . .	76
8.6	Comparison of both methods . . . . .	76
8.7	Method 1 with measured velocity of empty flume . . . . .	78
8.8	Executive summary . . . . .	79
<b>9</b>	<b>Discussion</b>	<b>81</b>
9.1	Performance of experiments . . . . .	81
9.2	Data processing . . . . .	82
9.3	Relevance of the results . . . . .	86

---

<b>10 Conclusion and recommendations</b>	<b>89</b>
10.1 Conclusions on the research questions . . . . .	90
10.2 Recommendations for further research . . . . .	92
<b>Bibliography</b>	<b>95</b>
<b>A Method of Goda and Suzuki (1976)</b>	<b>97</b>
<b>B Instrument specifications</b>	<b>99</b>
B.1 Framework FT and ADV . . . . .	99
B.2 Wave gauges (WG) . . . . .	100
B.3 Acoustic doppler velocimeter (ADV) . . . . .	101
B.4 Force transducer (FT)* . . . . .	102
B.5 Electromagnetic Flowmeter (EMF) . . . . .	103
<b>C Dissipation for different intervals</b>	<b>105</b>
C.1 V035L . . . . .	105
C.2 H068L . . . . .	106
C.3 ADV velocity measurements . . . . .	107
<b>D List of performed experiments</b>	<b>109</b>
D.1 Experiments set 1 . . . . .	109
D.2 Experiments set 2 . . . . .	110
<b>E Results experiments: First set</b>	<b>111</b>
E.1 Results of reflected, dissipated and transmitted energy . . . . .	111
E.2 Effect of diameter . . . . .	118
<b>F Approach with two methods</b>	<b>121</b>
F.1 Method 1 - Calibration from dissipation . . . . .	121
F.2 Method 2 - Calibration from forces . . . . .	122
<b>G Results experiments: Second set</b>	<b>123</b>
G.1 Assessing the methods for their own quantity . . . . .	123
G.2 Force prediction method 1 . . . . .	125
G.3 Force prediction method 2 . . . . .	128
<b>H Analysis of experiments with only current</b>	<b>131</b>



# List of Figures

1.1	Mangrove areas around the world in the year 2000 . . . . .	1
1.2	Schematic view of the convex-up profile and concave-up profile. . . . .	2
1.3	Import and export of sediment . . . . .	2
1.4	Fish ponds replacing mangrove areas in the Philippines . . . . .	3
1.5	Feedback loop once erosion starts . . . . .	3
1.6	Construction of a permeable structure consisting of brushwood. . . . .	4
2.1	Impression of the application of the structure with some definitions. . . . .	9
2.2	Orbital motion under a harmonic wave for different water depths . . . . .	11
2.3	Boundary layer separation on a cylinder . . . . .	12
2.4	Symmetric vortex generation behind a cylinder . . . . .	12
2.5	Strouhal number for a smooth cylinder . . . . .	13
2.6	Travel distance relative to the element diameter . . . . .	13
2.7	Different flow regimes around a smooth cylinder in oscillatory flow . . . . .	13
2.8	Overview of the behaviour of different vortex-shedding regimes . . . . .	14
2.9	The pressure and friction component of a drag force on a submerged body. . . . .	15
2.10	Drag and lift force acting on a submerged element . . . . .	15
2.11	Drag coefficient for different shapes dependent on $Re$ . . . . .	15
2.12	Phase difference between velocity, acceleration, drag force and inertia force. . . . .	16
2.13	Effect of surface roughness on the in-line force coefficients . . . . .	17
2.14	Contours of the drag coefficient for a trailing cylinder. . . . .	18
2.15	Bulk drag coefficient as a function of the dimensionless density $ad$ . . . . .	18
2.16	Energy balance for an incoming wave . . . . .	18
2.17	Averaged wave heights for daily and storm conditions . . . . .	21
2.18	Field conditions as measured by the BioManCo project. . . . .	21
2.19	Different types of permeable structures . . . . .	22
3.1	Schematic overview of the model in the wave flume . . . . .	25
3.2	View of the complete model with different orientations. . . . .	26
3.3	Overview of the tested configurations . . . . .	27
3.4	Validity regions of different wave theories . . . . .	28
3.5	From a linear wave to a 2nd order Stokes wave . . . . .	28
3.6	Schematic overview of the location of the wave gauges . . . . .	29
3.7	Flow diagram of processing the results . . . . .	30
3.8	Dissipation for successive intervals - V040U064 . . . . .	31
3.9	Example of the interval taken for calculation . . . . .	32
3.10	Comparison of the theoretical and measured transmission . . . . .	32
4.1	Energy balance for all the different configurations . . . . .	33
4.2	Recap of the configurations, with colour indication . . . . .	34
4.3	Total dissipation for the vertical configurations . . . . .	34
4.4	Total dissipation for the horizontal configurations . . . . .	35
4.5	Dissipation per element for the vertical configurations . . . . .	36
4.6	Dissipation per element for the horizontal configurations . . . . .	36
4.7	Drag coefficient according to Dalrymple, for the vertical configurations . . . . .	37
4.8	Drag coefficient according to Dalrymple, for the horizontal configurations . . . . .	37
4.9	Dissipation compared with previous research on a $D = 2.0$ cm model. . . . .	38
4.10	Comparison of the simplified drag coefficient plotted against $KC$ . . . . .	39
4.11	Comparison of the simplified drag coefficient plotted against $KC^*$ . . . . .	40
4.12	Comparison of the drag coefficient for the uniform open configurations . . . . .	40

5.1	Signal of the water surface elevation for a short and a longer wave. . . . .	41
5.2	Comparison between dissipation in total and per element - Vertical . . . . .	44
5.3	A sketch of the mechanisms of vortex shedding and sheltering. . . . .	45
5.4	Comparison between dissipation in total and per element - Horizontal . . . . .	45
5.5	Comparison of the simplified drag coefficient plotted against $KC^*$ . . . . .	46
5.6	A sketch of the sheltering effect for a longer excursion . . . . .	46
5.7	A sketch of the influence of the diameter on $KC^*$ . . . . .	47
6.1	Distribution of ADV measurements over height . . . . .	49
6.2	Top view of the vertical test configurations . . . . .	50
6.3	Change in wave shape for increasing period. . . . .	51
6.4	Natural frequency of the system in water. . . . .	52
6.5	Examples of the filtered signals. . . . .	52
6.6	Example of the time shift in the velocity signals . . . . .	53
6.7	Computation of the depth averaged velocity . . . . .	54
6.8	Location of the ADV, visualizing measured asymmetry. . . . .	55
6.9	Workflow for the two-method approach. . . . .	56
7.1	Example for the calculation of the average value of the maximum amplitude. . . . .	57
7.2	Visualization of increasing the structure width . . . . .	58
7.3	Amount of energy dissipation for an increasing width. . . . .	58
7.4	Negative velocity for increasing structure width . . . . .	59
7.5	Negative force for increasing structure width . . . . .	59
7.6	Visualization of different measurement locations . . . . .	60
7.7	Negative velocities for different locations in the model. . . . .	60
7.8	Negative forces for different locations in the model. . . . .	61
7.9	Amplification factor ( $UF$ ) for the linear velocity. . . . .	61
7.10	Force coefficients determined for 3 locations in the longitudinal configuration. . . . .	62
7.11	Force coefficients determined for 3 locations in the uniform configuration. . . . .	63
8.1	Comparison of the energy dissipation with the results of the first set. . . . .	66
8.2	Comparison of the measured velocities for a wave period of $T = 1.75s$ . . . . .	66
8.3	Reduction of the wave height inside the structure. . . . .	67
8.4	Mean velocity profile over depth. . . . .	68
8.5	Amplification factor for the measured velocity. . . . .	69
8.6	Amplification factor for the force in relation to a single element. . . . .	70
8.7	Colour convention for the configurations. . . . .	70
8.8	Colour convention for the location within the structure. . . . .	70
8.9	Calibrated amplification factors for the velocity. . . . .	71
8.10	Comparing the calculated velocity with the measured velocity - method 1. . . . .	71
8.11	Comparing the amplitude of the calculated and measured force - method 1 . . . . .	72
8.12	Example of the shape of the force signal for a $T = 2.00$ second wave. . . . .	72
8.13	Comparison of the drag coefficient with the results of experiment set 1. . . . .	73
8.14	Comparison of the drag coefficients with the results of Ozeren et al. (2014). . . . .	74
8.15	Comparison with the results of Chen et al. (2018) - Longitudinal. . . . .	74
8.16	Comparison with the results of Chen et al. (2018) - Uniform dense. . . . .	75
8.17	Comparing the calculated velocity with the measured velocity - method 2. . . . .	75
8.18	Comparing the calculated dissipation with the measured dissipation - method 2. . . . .	76
8.19	Comparing the amplification factors of method 1 and 2. . . . .	77
8.20	Comparing the factor for linear wave theory with the factor for undisturbed flow. . . . .	78
9.1	The root-mean-square of the lift force plotted against $KC$ . . . . .	82
9.2	Example of a fitting of the velocity for which the deviations are larger. . . . .	83
9.3	Influence of the relative element distance on $C_d$ . . . . .	84
9.4	Instantaneous stream-wise velocity component contours at $KC = 15$ . . . . .	85
9.5	Sketch of possible sheltering processes. . . . .	85

---

B.1	Framework to place the force transducer in the model. . . . .	99
B.2	Framework to place the ADV in the model. . . . .	99
C.1	Dissipation for successive intervals - V035L . . . . .	105
C.2	Dissipation for successive intervals - H068L . . . . .	106
C.3	Development of transverse velocity . . . . .	107
E.1	Energy balance for the vertical configurations . . . . .	112
E.2	Energy balance for the horizontal configurations . . . . .	113
E.3	Comparison of the dimensionless drag coefficient - Half width . . . . .	118
E.4	Comparison of the dimensionless drag coefficient - Full width . . . . .	119
F.1	Visualization of different measurement locations . . . . .	121
F.2	Different methods to calculate the relevant velocity inside the model. . . . .	122
G.1	Comparing the calculated dissipation with the measured dissipation - method 1. . . . .	123
G.2	Comparing the calculated force with the measured force - method 2. . . . .	124
H.1	Configurations which are tested with a current-only condition. . . . .	131
H.2	The measured force vs. the measured velocities. . . . .	132
H.3	The measured force vs. the measured velocities with an amplification factor. . . . .	132



# List of Tables

1.1	Overview of the processes in reality and in the experiments . . . . .	6
2.1	Wave characteristics for different water depths . . . . .	10
2.2	Overview of the KC regimes . . . . .	13
2.3	Overview of relevant research . . . . .	20
2.4	Characteristic values for the reference wave conditions . . . . .	23
3.1	Comparison of real and model dimensions . . . . .	26
3.2	Tested configurations with their characteristics . . . . .	27
3.3	Overview of the environmental conditions for the reference and model case. . .	28
3.4	Tested wave conditions with their characteristic values . . . . .	29
4.1	Heart-to-heart distance of the elements . . . . .	39
5.1	The increase in dissipation for an increase in width - Vertical orientation. . . .	42
5.2	The increase in dissipation for an increase in width - Horizontal orientation. . .	43
5.3	Amplification factors for changing the orientation from vertical to horizontal . .	43
6.1	Tested wave conditions with their characteristic values . . . . .	51
D.1	Set 1 - Test conditions with combinations of configuration and wave period. . .	109
D.2	Set 2 - Test conditions with combinations of configuration and wave period/ current velocity. . . . .	110
E.1	Results - V040U064 . . . . .	114
E.2	Results - V040U089 . . . . .	114
E.3	Results - V040L . . . . .	114
E.4	Results - V040S . . . . .	114
E.5	Results - V076U064 . . . . .	115
E.6	Results - V076U089 . . . . .	115
E.7	Results - V076L . . . . .	115
E.8	Results - V076S . . . . .	115
E.9	Results - H040U064 . . . . .	116
E.10	Results - H040U089 . . . . .	116
E.11	Results - H040L . . . . .	116
E.12	Results - H040S . . . . .	116
E.13	Results - H076U064 . . . . .	117
E.14	Results - H076U089 . . . . .	117
E.15	Results - H076L . . . . .	117
E.16	Results - H076S . . . . .	117
G.1	Force prediction for the longitudinal configuration - Method 1. . . . .	125
G.2	Force prediction for the uniform dense configuration - Method 1. . . . .	126
G.3	Force prediction for the longitudinal configuration - Method 2. . . . .	128
G.4	Force prediction for the uniform dense configuration - Method 2. . . . .	129



# List of Symbols

Symbol	Unit	Definition
$A$	$m^2$	Cross-sectional area perpendicular to flow direction
$a$	$m$	Wave amplitude
$c$	$m/s$	Wave celerity
$c_g$	$m/s$	Wave group celerity
$C_a$	-	Added mass coefficient
$C_d$	-	Drag coefficient
$\overline{C_d}$	-	Bulk drag coefficient
$C_{diss}$	-	Dissipation coefficient
$C_m$	-	Inertia coefficient
$C_r$	-	Reflection coefficient
$C_t$	-	Transmission coefficient
$d$	$m$	Water depth
$D$	$m$	Cylinder diameter
$E_i$	$J/m^2$	Incoming energy
$E_{diss}$	$J/m^2$	Dissipated energy
$E_r$	$J/m^2$	Reflected energy
$E_t$	$J/m^2$	Transmitted energy
$\epsilon_v$	$kg/s^3$	Energy dissipation per unit horizontal area
$\eta$	$m$	Surface elevation
$f$	$Hz$	Frequency
$f_v$	$Hz$	Vortex shedding frequency
$F_d$	$N$	Drag force
$F_I$	$N$	Inertia force
$F_L$	$N$	Lift force
$g$	$m/s^2$	Acceleration of gravity
$\gamma_b$	-	Breaker parameter
$h_v$	$m$	Submerged cylinder height
$H$	$m$	Wave height
$H_b$	$m$	Breaker height
$H_i$	$m$	Incoming wave height
$H_r$	$m$	Reflected wave height
$H_t$	$m$	Transmitted wave height
$k$	$m^{-1}$	Wave number
$KC$	-	Keulegan Carpenter number
$KC^*$	-	Adapted Keulegan Carpenter number, based on element spacing
$K_v$	-	Transmission coefficient
$L$	$m$	Wave length
$L_m$	$m$	Length scale model
$L_p$	$m$	Length scale prototype
$\lambda$	-	Scaling factor
$\lambda_s$	$m$	Spacing between the elements
$\mu$	$Pa \cdot s$	Dynamic viscosity
$n$	-	Porosity
$n_f$	-	Frontal porosity
$N$	$\#/m^2$	Number of elements per unit area
$N_m$	$\#$	Number of measurement points over depth
$p$	$Pa$	Pressure
$\phi$	$^\circ$	Angle between the flow and the line perpendicular to the element surface

Symbol	Unit	Definition
$r_0$	$m$	Element radius
$Re$	-	Reynolds number
$\rho_w$	$kg/m^3$	Water density
$\Delta S$	$m$	Mean spacing
$t$	$s$	Time
$T$	$s$	Wave period
$\tau_0$	$Pa$	Shear stress
$u$	$m/s$	Horizontal velocity
$u_c$	$m/s$	Constricted horizontal velocity
$u_m$	$m/s$	Measured horizontal velocity
$u_l$	$m/s$	Velocity of linear theory
$\dot{u}$	$m^2/s$	Acceleration of horizontal velocity
$\hat{u}$	$m/s$	Amplitude of horizontal velocity
$v$	$m/s$	Vertical velocity
$\dot{v}$	$m^2/s$	Acceleration of vertical velocity
$\hat{v}$	$m/s$	Amplitude of vertical velocity
$\nu$	$m^2/s$	Kinematic viscosity
$\omega$	$rad/s$	Angular velocity
$x$	$m$	Horizontal distance along direction of propagation
$y$	$m$	Horizontal distance perpendicular to direction of propagation
$z$	$m$	Vertical distance

# Introduction

*This first chapter contains the introduction into the problem and the research approach. In section 1.1, the erosion problems present at mangrove coasts are described, followed by an explanation of the hydrodynamic processes within a permeable structure. Based on the knowledge gap that follows from the problem description, the goal of this research is presented in section 1.2, followed by the research questions in section 1.3. As this research can not include everything, the scope and approach of this research are presented in section 1.4, which will explain the chosen trajectory. The chapter concludes with the reading guide of the report in section 1.5.*

## 1.1. Problem description

For many people in tropical countries, mangrove forests serve as a natural sea defence against the effects of wind, waves and water currents (FAO, 2008). These forests flourish on flat and muddy coasts, protecting them from severe erosion and storm surge attack and providing communities with fish, timber and wood resources (FAO, 2008; Winterwerp et al., 2013). Also in view of sea level rise, the mangroves may play an important role, as they have the capacity to increase the bed level following the sea level (McIvor et al., 2013).

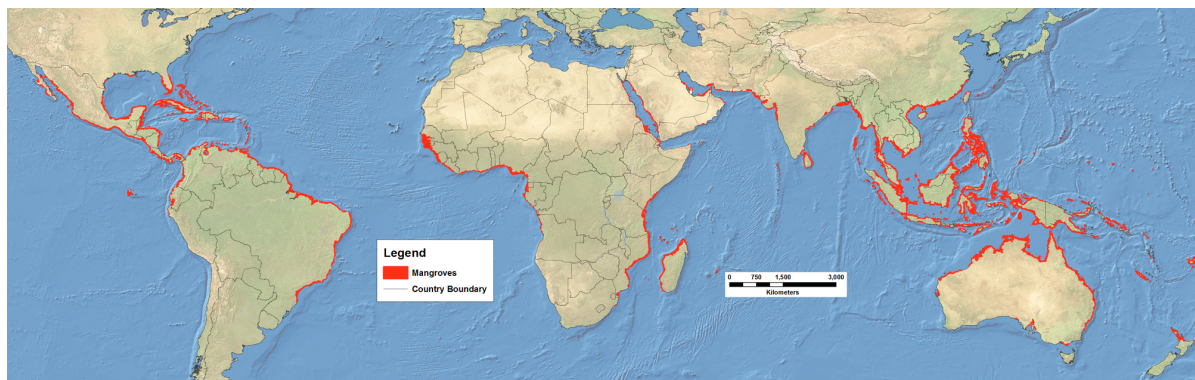


Figure 1.1: Mangrove areas around the world in the year 2000, shaded in red (Giri et al., 2011). Map redrawn by UNEP/DEWA.

Mangrove species include tropical and subtropical trees, primarily occurring at latitudes near the equator (see Figure 1.1) (NOAA, 2017). They grow in tidal areas that are alternating wet and dry, between the mean high water level and high high water spring level (see Figure 1.2a).

Mangroves require areas exposed to low wave energy, which makes convex-up profiles a suitable location for them, with waves breaking on the foreshore. The wave energy that reaches the vegetation is attenuated by the roots of the mangroves, making it possible for fine sediment to settle (NOAA, 2017).

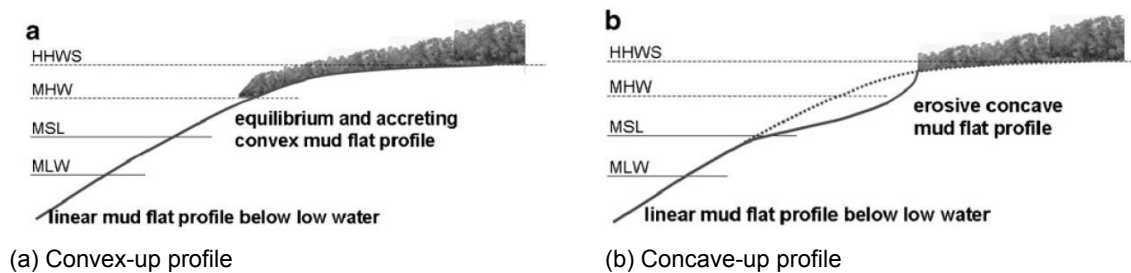


Figure 1.2: Schematic view of the (a) equilibrium convex-up profile and (b) eroding concave-up profile (Winterwerp et al., 2013).

Mangrove coastlines are often dynamic systems, with cyclic patterns of accretion and erosion. In relatively quiet conditions the systems will have an import by tidal motion and export by small surface waves stirring up the fine sediment (Figure 1.3). In storm conditions, the larger waves may stir up more sediment, resulting in more erosion. But as these waves also put sediment from the foreshore in suspension, resulting in an additional sediment source, the import and export by this wave action is balanced (Ecoshape, 2015; Winterwerp et al., 2013). However, a disturbance in this dynamic balance can cause severe damage to the system. For years now, the coastal area covered by mangroves is declining globally (FAO, 2008). Also in the region of Demak, Indonesia, mangroves have been removed (for shrimp farming), resulting in severe erosion of the coast. Over the last decades, erosion has gone up to over 1000 meters at certain locations (Ecoshape, 2015).

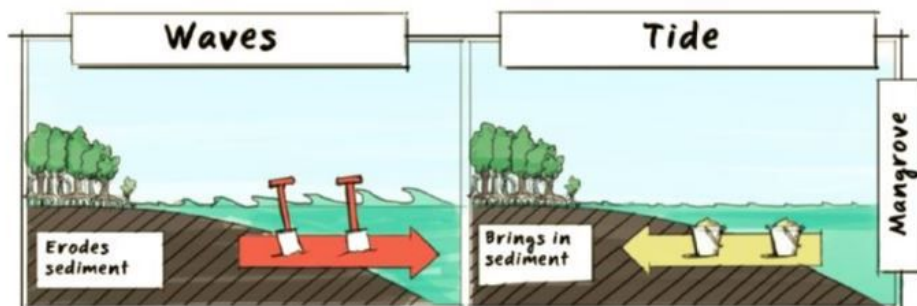


Figure 1.3: Import and export of sediment (Ecoshape, 2015)

The construction of fish ponds is considered one of the main causes that may have tipped the dynamic equilibrium. These ponds were built in the mangrove areas around the 1980s to expand the aquaculture sector (Ecoshape, 2015). Already with construction, numerous mangroves were cut down to make room for the ponds (see Figure 1.4 for an example). But secondary effects may also play a role in the morphodynamic equilibrium and the decrease of mangroves. With the construction of the dikes around the ponds, sediment transport from the rivers to the coast is blocked. Also the tidal prism is reduced, resulting in a decrease of water flow and sediment transport to the coast. The erosion caused by the waves is no longer fully compensated and the coast will retreat (Winterwerp et al., 2013), developing a concave-up profile (Figure 1.2b).

As waves can penetrate further with this increase of water depth in front of the mangroves, the wave attack on the mangrove area will also increase resulting in an even more (net) erosion. The feedback loop that develops as a result is shown in Figure 1.5.



Figure 1.4: Fish ponds replacing mangrove areas in the Philippines (Gil S. Jacinto, 2005)

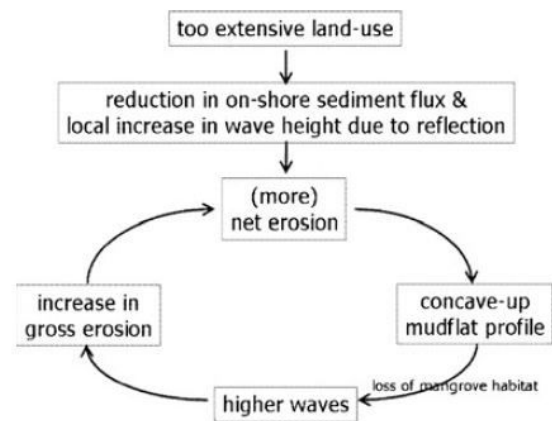


Figure 1.5: Feedback loop once erosion starts (Winterwerp et al., 2013).

In recent years, hard engineering methods have been applied to try to stop the erosion and prevent the land from flooding. But for muddy coasts, like Demak, these structures can have the opposite effect. Due to their impermeability, incoming waves will (partially) be reflected, causing an increase in wave height in front of the structure. The increase in wave height will result in higher flow velocities at the bottom due to their larger orbital velocity, creating local scour. For short waves the length of this scour area will be 10-25m, but for the longer swell waves this can go up to a few 100 meters (Winterwerp et al., 2013). The scour will induce the concave-up profile earlier mentioned, resulting in even more erosion. A second effect of the impermeability is the blockage of sediment. As the tide can no longer import fine sediment, the offshore sediment source is reduced. The system is out of balance and erosion due to wave action will be governing. This imbalance in the fine sediment import and export is considered one of the main reasons for the retreating coastlines and failing restoration projects (Winterwerp et al., 2013).

A relatively new approach to prevent the erosion, is the application of 'Building with Nature'. This approach aims to incorporate natural processes in engineering solutions, instead of relying only on hard infrastructures like dams and dikes. Examples are the restoration of natural sediment input to restore coastlines, or restoring coastal ecosystems like mangrove forests. This approach is currently also applied in the area of Demak, by placing permeable brushwood structures (Figure 1.6). Their purpose is to restore the sediment balance to promote the natural growth of mangroves, while integrating sustainable land use practice (Ecoshape, 2015).

The application of permeable structures focuses on minimizing the reflection and maximizing the dissipation. The permeability of the structure makes it possible for suspended fine sediment to go through it, while the minimal reflection reduces the negative scour effects in front of the structure. The dissipation of wave energy through the permeable body will create a sheltered zone between the structure and the coastline, where the suspended sediment can settle. This will restore the sediment balance and on the long term transform the concave-up coastline into a convex-up coastline, which will promote the natural regrowth of the mangroves. The restoration of the coastline profile will be performed in stages. A first line of structures will be built, after which there is accretion and colonization. Then new structures will be built seawards of the first line, repeating the process until the forest has expanded to the desired width. However, the structures currently applied are built on the basis of engineering judgment and trial and error, instead of design rules.



Figure 1.6: Construction of a permeable structure consisting of brushwood (EcoShape, 2018).

This research is performed as part of the BioManCO project (bio-morphodynamic modeling of mangrove-mud coasts) and focuses on the wave-structure interaction in a permeable structure. The final goal of the larger project performed by three PhD students is to develop a model for future restorations of mangrove forests on mud coasts, based on scientific knowledge of the morphological, ecological, physical and biological processes.

## 1.2. Research goal

The permeable structures currently applied in Demak show positive results concerning the wave dissipation. Previous flume experiments by Haage (2018) measured wave attenuation by schematized permeable structures. The total measured wave dissipation was assigned to the drag force, and the drag coefficient was calibrated to fit the measurements using the method of Mendez and Losada (2004). However, this approach involves a number of assumptions, such as neglecting the inertia forces or using linear wave theory. Velocity and force measurements are necessary to evaluate such assumptions, and to determine which are the most important processes driving wave energy dissipation. The goal of this research is to get a better understanding of the hydrodynamics in the permeable structure under pure wave loading and make a distinction between the different physical processes causing the wave dissipation.

## 1.3. Research question

The main question of this research is:

**How do the *physical processes* of drag force, velocity increase and *possible non-linearity's* influence the wave dissipation inside a permeable structure?**

The following sub-questions support the main research question:

1. How does the dissipation of wave energy change for a change in structure width, orientation, configuration or wave condition?
2. What is the influence of element\* diameter on wave energy dissipation?
3. What is the relative importance of the physical processes causing the wave dissipation?
  - (a) How does the relative importance of the processes change for different wave conditions?
  - (b) How do those processes change for different configurations?

\* *The individual cylinders used in the scale model are called elements. The scale model as a whole is called the structure.*

### **Physical processes**

The processes experienced by the physical model are called the physical processes. Examples are forces acting on the structure as a result of the flow velocity experienced by the model, an increase in wave height as a result of a decrease in flow cross-section or an increase in flow velocity. Section 2.2.2 will go into the details of different physical processes.

### **Possible non-linearity's**

The most simple wave is the regular linear wave, which will be explained in Section 2.2.1. The shape of this wave can be described by a sine function. As waves become more non-linear, the shape of the wave changes and the function to describe the shape includes more terms. This shape, with shorter peaks and longer troughs, may have an effect on the wave dissipation processes in the structure.

## 1.4. Scope and approach

### Scope

This research focuses on the physical dissipation processes in a scale model, which is a simplification of the real structure. The waves conditions refer to the situation in Demak, Indonesia, and are scaled to model dimensions. As not all processes of reality can be dealt with in this research, some simplifications have been applied:

Table 1.1: Overview of the processes in reality and in the experiments.

Reality	Experiments
Waves in combination with currents	Waves only
Irregular waves/ breaking waves	Regular/ non-breaking waves
Waves approaching under an angle	Unidirectional waves
Sediment transport	Clear water
Irregularities along the structure or bottom	Regular structure on a flat bottom
Deterioration of the structure over time	No deterioration during experiments
Irregular surface of bamboo elements	Smooth aluminum elements
Possible combination of horizontal and vertical elements	Only horizontal/ only vertical elements

The result is a simplified test case, making it possible to look at physical processes that lie at the basis of wave dissipation inside the structure. Once these processes are understood, the model can be adjusted step by step to a more realistic case in further research.

### Approach

To get a better understanding of the physical processes causing the wave dissipation, they have been analyzed in a scale model in the laboratory. The conditions for these scale tests are based on a literature study on wave action around cylinders and the study of a reference case in Demak, Indonesia.

The laboratory experiments consist of two sets. In the first set, different configurations are tested with a vertical and a horizontal orientation. The results are used to determine the effect of the configuration on wave dissipation (sub-question 1) and to make a comparison with the research of Haage (2018) on the effect of scaling (sub-question 2). The second set of experiments contains more detailed measurements of the force and velocity at different locations inside the structure, to determine the relative importance of the processes causing energy dissipation. The results are used to study the development of the velocity in the structure and determine the force coefficients and amplification factor for the velocity (sub-question 3) which can be used for future modelling.

## 1.5. Reading guide

The results of the literature study are presented in Chapter 2, which gives background information on flow around a single cylinder and an array of cylinders. Also the relevant parameters used to describe the processes and results are explained.

This is followed by the details of the first set of experiments. Chapter 3 presents set-up of the experiments, with details of the wave flume, the configurations and the location of the instruments, the wave conditions that are applied and the way of processing the results. The results of the experiments are presented in Chapter 4. The first part of this chapter focuses on the effect of the different configurations, whereas the second part makes a comparison with previous research on a 2 *cm* model. The implication of these results are analyzed in Chapter 5. The same sequence is applied for the second set of experiments, with the set up of the experiments in Chapter 6, the results in Chapter 7 and the analysis of the results in Chapter 8.

The report concludes with an evaluation of the methodology and interpretation of the results of this research in Chapter 9, followed by the conclusions on the research questions and recommendations for further research in Chapter 10.



## Theoretical background

*This chapter presents a theoretical background for structures under wave action. It starts with the characteristic properties of waves, followed by the influence of waves on structures (Section 2.2). It continues with an overview of previous research on cylinders in wave and current situations in Section 2.3 and concludes with a link to reality by describing the situation in Demak, Indonesia, in Section 2.4.*

### 2.1. Application of permeable structures

Permeable structures have different applications, but are mostly used for their ability to attenuate wave energy or flow velocity, while letting through the suspended sediment. Along the Dutch and German coastline, such structures are applied perpendicular to the coast in order to attenuate the alongshore current (Brielle, 2014). Current research focuses on the structure set-up used in Demak, Indonesia, where the structures are parallel to the coast as shown in Figure 2.1, to reduce the incoming wave energy and create a sheltered zone in front of the coast where sediment can settle.

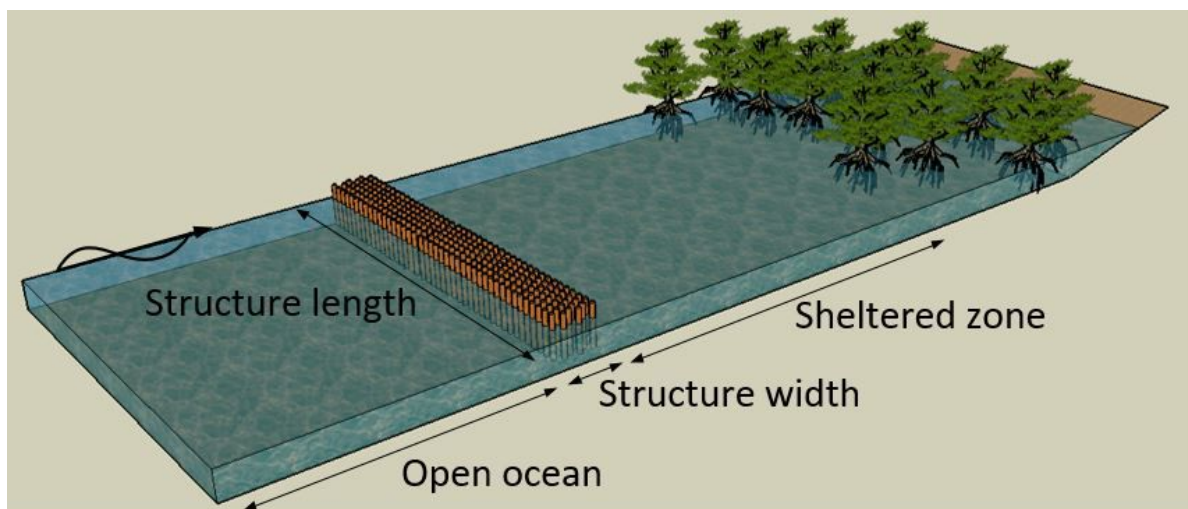


Figure 2.1: Impression of the application of the structure with some definitions. Lengths not to scale.

## 2.2. Wave action

In Demak, the permeable structures are applied in shallow to intermediate water near the coast and are subjected to wave action. Waves develop in deep, open waters from where they travel towards the coast. At the open ocean the waves are not affected by the bottom, but as the water depth decreases towards the coast, the shape of the waves changes. The waves steepen and eventually break on the shore. The distinction between shallow and deep water is based on the ratio between water depth and wave length. This section presents the important concepts of wave action and their interaction with structures.

### 2.2.1. Wave characteristics

#### Linear wave theory

For small waves in relatively deep water the linear wave theory, or first-order theory, can be applied (Schriereck, 2001). This theory states that the shape of a two-dimensional progressive gravity wave can be approximated by a simple sine function under the assumption of no friction losses (Holthuijsen, 2007):

$$\eta(x, t) = a \sin(\omega t - kx) \quad (2.1)$$

in which  $\eta$  is the surface elevation,  $\omega = 2\pi/T$  is the angular velocity,  $a$  is the wave amplitude,  $k = 2\pi/L$  is the wave number,  $t$  is the time and  $x$  the horizontal location.

If free waves are assumed (not subjected to external forces), a relationship between radian frequency and wave number can be found (Holthuijsen, 2007):

$$\omega = gk \tanh(kd) \quad \text{or} \quad L = \frac{gT^2}{2\pi} \tanh\left(\frac{2\pi d}{L}\right) \quad (2.2)$$

which is called the dispersion relationship. Based on this also the phase speed of the waves can be determined:

$$c = \frac{gT}{2\pi} \tanh(kd) \quad (2.3)$$

The energy ( $E$ ) carried by a linear wave is proportional to the wave height squared (Holthuijsen, 2007). Without losses due to dissipation, the energy of the incoming wave can be described with:

$$E = \frac{1}{8} \rho g H^2 \quad (2.4)$$

in which  $\rho$  is the mass density,  $g$  is the gravitational constant and  $H$  is the wave height.

The most important wave characteristics in shallow, intermediate and deep water are summarized in Table 2.1.

Table 2.1: Wave characteristics for different water depths (Schriereck, 2001), in which  $d$  is the water depth,  $L$  is the wave length,  $k$  is the wave number,  $c$  is the wave speed,  $g$  is the gravitational constant and  $T$  is the wave period.

Shallow water	Intermediate water	Deep water
$\frac{d}{L} < 0.05$	$0.05 < \frac{d}{L} < 0.5$	$0.5 < \frac{d}{L}$
$kd \rightarrow 0$	$kd \approx 1$	$kd \rightarrow \infty$
$c = \sqrt{gd}$	$c = \frac{gT}{2\pi} \tanh(kd)$	$c = \frac{gT}{2\pi}$
$L = T\sqrt{gd}$	$L = \frac{gT^2}{2\pi} \tanh(kd)$	$L = \frac{gT^2}{2\pi}$

The waves tested in this research have a wave height of 13cm, with a water depth of 60cm in experiment set 1 and a water depth of 55cm in experiment set 2. With a wave length that varies between 1.64-4.32m, the ratio of water depth over wavelength varies between 0.12-0.37. This means that the tests are in intermediate water conditions. More details on the wave conditions are given in Section 3.2 and 6.2.

### Flow under wave action

The water particles under a wave move in an orbital motion, as depicted in Figure 2.2. The motion transforms from circular in deep water to elliptical in shallow water, where the elliptical motion tends to a straight horizontal motion towards the bottom. The horizontal and vertical velocity component of this motion can be described with (Holthuijsen, 2007):

$$u(x, z, t) = \hat{u} \sin(\omega t - kx) \quad \text{with} \quad \hat{u} = \omega a \frac{\cosh[k(d+z)]}{\sinh(kd)} \quad (2.5)$$

$$v(x, z, t) = \hat{v} \cos(\omega t - kx) \quad \text{with} \quad \hat{v} = \omega a \frac{\sinh[k(d+z)]}{\sinh(kd)} \quad (2.6)$$

in which  $d$  is the water depth,  $z$  is the position in the water column,  $\hat{u}$  the amplitude of the horizontal particle velocity and  $\hat{v}$  the amplitude of the vertical particle velocity. The origin of the axis is the still water level, with the  $z$ -axis positive in upward direction.

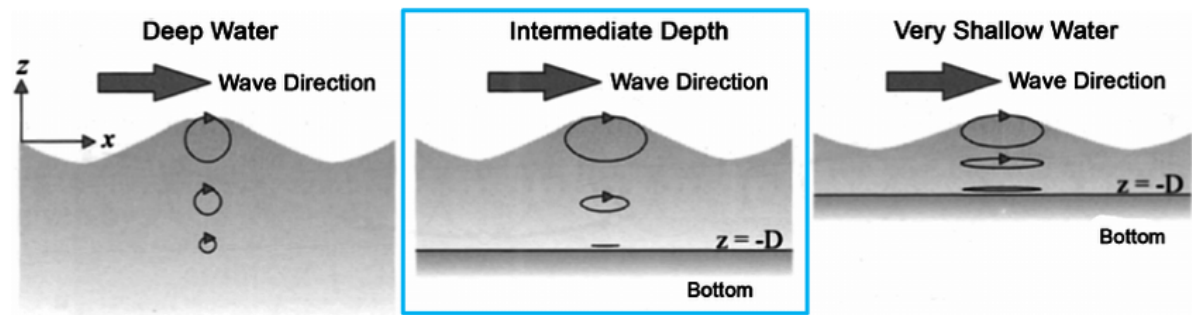


Figure 2.2: Orbital motion under a harmonic wave for different water depths (Holthuijsen, 2007). Wave conditions in this research are in intermediate depth.

### Shoaling and wave breaking

As the waves travel from deep to shallow water they transform due to the influence of decreasing water depth, while the period and wave energy remain the same. The wave celerity decreases, which causes the wave height to increase to conserve the wave energy. This process is called shoaling, which causes waves to steepen until they break. Breaking occurs when the ratio of wave height over water depth or wave length becomes too large, depending on the location of the wave. Miche described the limit of wave steepness with the breaking criterion (Schriereck, 2001):

$$H_b = 0.142L \tanh\left(\frac{2\pi}{L}h\right) \quad (2.7)$$

For shallow water, this formula leads to  $\gamma_b = H_b/h = 0.88$ . For solitary waves, this limit is slightly different:  $\gamma_b = H/h = 0.78$ . In the process of wave breaking, energy is transformed into heat by turbulence and friction.

## 2.2.2. Waves around a single cylinder

### Cylinder in uniform flow

For flow around elements, the no-slip condition applies at every surface in the flow (Nepf, 2011). This condition states that the flow velocity on the surface must match the velocity of the surface. The transition layer from the zero velocity at the surface to the undisturbed flow velocity is called the boundary layer. For low flow velocities, the boundary layer will be able to follow the surface of the object in the flow. However, as velocity increases, the layer will separate from the surface at the so-called point of separation (see Figure 2.3)(Sumer and Fredsoe, 2006). This generates a low pressure zone behind the cylinder, which is called the wake. The difference in flow velocity of the boundary layer and the wake area creates a vortex on both sides behind the cylinder (Figure 2.4).

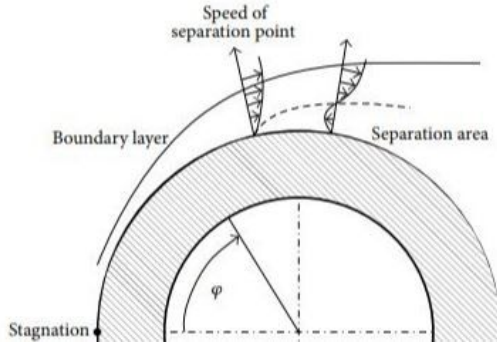


Figure 2.3: Boundary layer separation on a cylinder (Zhang and Qi, 2016).

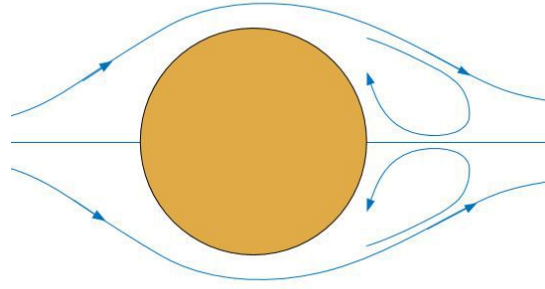


Figure 2.4: Symmetric vortex generation behind a cylinder, for  $5 < Re < 40$ .

In case of an object with sharp edges, the point of separation is predetermined by the location of the leading edge. However, for circular cylinders the point of separation can vary depending on the Reynolds number (Singha and Balachandar, 2011), which gives a description of the relative importance of viscous and inertial components:

$$Re = \frac{\text{Inertia forces}}{\text{Viscous forces}} = \frac{uD}{\nu} \quad (2.8)$$

in which  $u$  is the velocity of the fluid,  $D$  is the length scale of the object in the flume (in this research the diameter) and  $\nu$  is the kinematic viscosity.

For very small values of  $Re$ , a fixed pair of symmetric vortexes is generated, for which the length grows with increasing  $Re$ . If  $Re$  becomes larger than 40, the vortexes start shedding alternately at either side of the cylinder, creating a vortex street (Sumer and Fredsoe, 2006). For  $Re$  between 40 and 200, this vortex street is laminar, with the shedding only in the direction of the flow. By increasing  $Re$  further, the shedding gets a 3-dimensional character and the flow becomes turbulent. The exact point of transition from laminar to turbulent flow can vary depending on the geometry of the structure. For a single cylinder, this point lies at  $Re \approx 200$ , while for an array of cylinders this can be in the order of  $Re \approx 150 - 200$  (Sumer and Fredsoe, 2006).

For the wave conditions applied in this research, the amplitude of the depth average horizontal velocity varies between 0.16-0.24m/s for the undisturbed waves. With an element diameter of 4cm, this results in Reynolds numbers that vary between 6000-10.000.

The frequency of the vortex-shedding can be normalized with the flow velocity  $u$  and diameter  $D$ , which is called the Strouhal number and is defined as:

$$St = \frac{f_v D}{u} \quad (2.9)$$

in which  $f_v$  is the vortex shedding frequency. For the Reynolds numbers applicable in this research ( $Re = 10^3 - 10^4$ ), the Strouhal number has a constant value of approximately 0.2 (see Figure 2.5).

### Cylinder in oscillatory flow

To determine the importance of the drag and inertia component around an object in oscillatory flow, Keulegan and Carpenter came up with the Keulegan-Carpenter Number ( $KC$ ) (Sumer and Fredsoe, 2006):

$$KC = \frac{U_w T}{D} = \frac{2\pi a}{D} \quad (\text{for linear waves}) \quad (2.10)$$

in which  $U_w$  is the maximum orbital velocity,  $T$  is period of the oscillating motion and  $a$  is the amplitude of the oscillatory motion.  $KC$  determines the distance fluid particles can travel

in a wave period, relative to the size of the object in the flow (see Figure 2.6). For small  $KC$  the distance relative to the size is small and the situation is wave dominated, causing the drag component to be neglected (Graham, 1980). As  $KC$  tends towards infinity the situation for half a period looks like a current situation. So, for high  $KC$  the situation becomes flow dominated and the inertia component can be neglected.

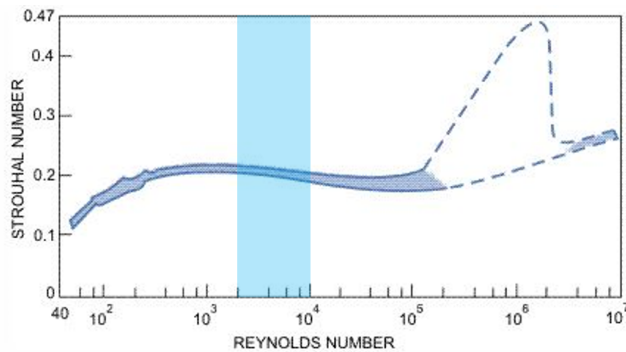


Figure 2.5: Strouhal number for a smooth cylinder as function of the Reynolds number (Blevins, 1990). The blue area marks the range for this research.

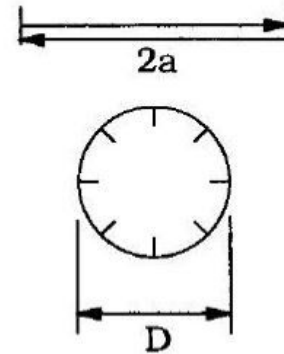


Figure 2.6: Travel distance relative to the element diameter (Sumer and Fredsoe, 2006).

Also in relation to the  $KC$ -number, the different vortex-regimes can be determined. Between  $KC = 1.1$  and  $KC = 7$ , the transition is made from the unseparated flow regime to the vortex shedding regime, as depicted in Figure 2.7.

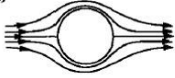
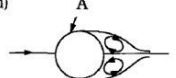
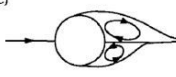
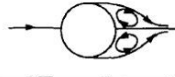
a)		No separation. Creeping (laminar) flow.	$KC < 1.1$	d)		A pair of symmetric vortices. Turbulence over the cylinder surface (A).	$2.1 < KC < 4$
b)		Separation with Honji vortices. See Figs. 3.3 and 3.4	$1.1 < KC < 1.6$	e)		A pair of asymmetric vortices	$4 < KC < 7$
c)		A pair of symmetric vortices	$1.6 < KC < 2.1$	f)		Vortex shedding	$7 < KC$ Shedding regimes

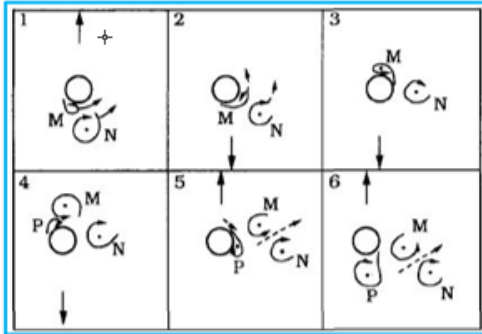
Figure 2.7: Different flow regimes around a smooth cylinder in oscillatory flow for  $Re = 10^3$  (Sumer and Fredsoe, 2006).

As the flow under waves is oscillatory, it reverses each half period. A difficult pattern of vortex shedding on both the front and the back side of the cylinder occurs. Extensive research into the different shedding regimes has been done by Williamson (1985), who gives a systematic description of the vortex trajectories. Figure 2.8 shows the development of vortices for the first 4 regimes, but these can be extended to higher  $KC$  values. The regimes are defined by the number of vortex pairs that are shed. Table 2.2 gives for the different regimes the range in  $KC$  and  $Re$  number:

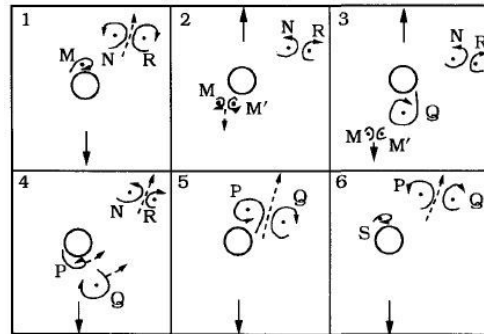
Table 2.2: Overview of the different vortex-regimes and their  $KC$  and  $Re$  range (Sumer and Fredsoe, 2006).

KC regime	KC range	Re range
Single pair	$7 < KC < 15$	$1.8 - 3.8 \times 10^3$
Double pair	$15 < KC < 24$	$3.8 - 6.1 \times 10^3$
Three pairs	$24 < KC < 32$	$6.1 - 8.2 \times 10^3$
Four pairs	$32 < KC < 40$	$8.2 - 10 \times 10^3$

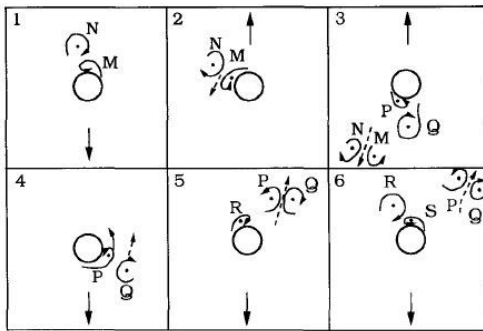
Figure 2.8a and 2.8b show the first regime, called the 'first-pair' regime. In Figure 2.8a, vortex M is developing while vortex N has just been shed. As the flow reverses in frame 2, both vortices are washed over the cylinder. In frame 4, vortex M is shed and pairs with vortex N in frame 5. The two vortices rotate in opposite direction and are convected by the velocity field of the other (Sumer and Fredsoe, 2006). The pair will then move away from one side of the cylinder in transverse direction, or at a 45° angle, depending on the  $KC$  number. For an increase in  $KC$ , also the number of vortex pairs will increase, convecting away from both sides of the cylinder as depicted in Figure 2.8c and 2.8d.



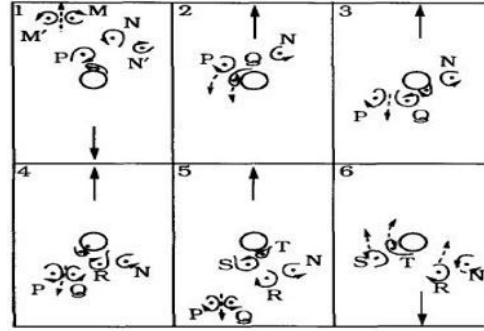
(a) Single-pair regime,  $7 < KC < 13$ . The vortices create a transverse vortex street on one side of the cylinder.



(b) Single-pair regime,  $13 < KC < 15$ . The vortices create a vortex street at a 45° angle, at one side of the cylinder.



(c) Double-pair regime,  $15 < KC < 24$ . The vortices create two vortex streets, in opposite direction and from opposite sides of the cylinder.



(d) Three-pairs regime,  $24 < KC < 32$ . Three vortices are shed each half cycle, creating a more irregular pattern.

Figure 2.8: Overview of the behaviour of different vortex-shedding regimes for  $7 < KC < 32$ . The arrows indicate the movement of the cylinder, but the reference frame also moves with the cylinder. This is analogous to the water movement under waves. (Williamson, 1985)

For the wave conditions applied in this research, the  $KC$ -values are low ( $KC = 4 - 13$ ) for the undisturbed conditions, resulting in a single pair regime (Figure 2.8a). However, as the velocity might increase inside the structure, also regimes with more pairs of vortices might be reached (Figure 2.8b - 2.8d).

### Force acting on elements in oscillatory flow

The total force per unit length acting on an element in oscillatory flow is the sum of this inertia and drag component, as expressed by the Morison equation for slender piles (Morison et al., 1950):

$$F = F_m + F_d = \frac{1}{4} C_m \rho \pi D^2 \dot{u} + \frac{1}{2} C_d \rho D u |u| \quad (2.11)$$

in which  $C_m$  is the inertia coefficient,  $\rho$  is the mass density,  $D$  is the diameter of the cylinder and  $C_d$  is the drag coefficient.

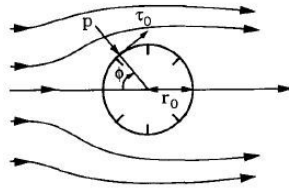


Figure 2.9: The pressure and friction component of a drag force on a submerged body (Sumer and Fredsoe, 2006).

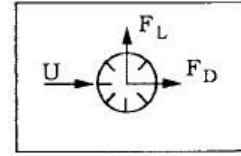


Figure 2.10: Drag and lift force acting on a submerged element (Sumer and Fredsoe, 2006).

The force exerted on an element in the direction of the flow is the resultant force of a pressure stresses normal to the surface,  $p$ , and a shear stress on the surface,  $\tau_w$  (see Figure 2.9) and can be written as:

$$F_d = F_p + F_f = \int_0^{2\pi} p \cos(\phi) r_0 d\phi + \int_0^{2\pi} \tau_0 \sin(\phi) r_0 d\phi \quad (2.12)$$

in which  $\phi$  is the angle between the flow and the line perpendicular to the surface and  $dA$  the differential area of the element. The force in cross-flow direction is called the lift force (Figure 2.10). Due to symmetry of the flow around a circular cylinder, the resultant mean lift force will be zero. However, the instantaneous lift force is asymmetrical and therefore not zero (Sumer and Fredsoe, 2006). The lift force can be described in the same way as the drag force:

$$F_L = \frac{1}{2} C_L \rho D u |u| \quad (2.13)$$

The empirical drag coefficient in Equation 2.11 varies for different shapes and Reynolds numbers, as depicted in Figure 2.11a. For a flat plate, the drag coefficient is more or less constant at a value of  $C_d = 2.0$ , following from the earlier mentioned predetermined location of the separation point. For circular elements, the drag coefficient is highly dependent on the Reynolds number, as depicted in Figure 2.11b. For the range of Reynolds numbers in this research, the value of the drag coefficient is close to 1.0 (blue area in Figure 2.11).

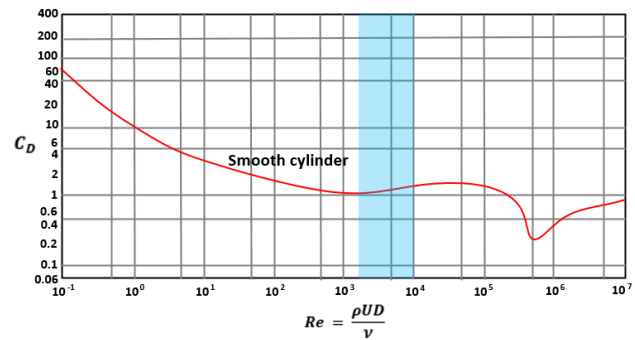
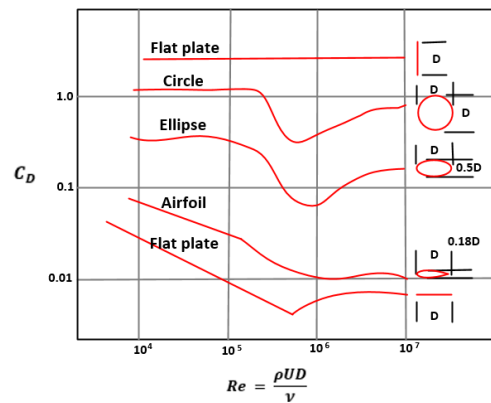


Figure 2.11: (a) Drag coefficient for different shapes dependent on Re (b) Drag coefficient for a smooth, circular cylinder dependent on Re (Adapted from Munson, 2002). Blue shaded area is the applied range of Reynolds numbers.

As mentioned earlier, the inertia component cannot be neglected for oscillatory flow and is added to the in-line drag force as described in formula 2.11. The inertia force can also be divided into two components:

$$F_m = \frac{1}{4} C_m \rho \pi D^2 \dot{u} = m' \dot{u} + \rho A \dot{u} \quad (2.14)$$

in which  $m'\dot{u}$  is the hydrodynamic-mass force and  $\rho A\dot{u}$  is the Froude-Krylov force with  $m'$  the hydrodynamic mass and  $A$  the cross sectional area of the cylinder (Sumer and Fredsoe, 2006).

The hydrodynamic-mass force accounts for the mass that is accelerated due to the object in the flow. It can be illustrated by moving an object through a fluid. If the area of the object is large, it will experience a high resistance due to the fact that the mass of the fluid around the object also has to be accelerated. This mass is also called the 'added mass'. The added mass for a circular cylinder and resulting force are given by:

$$m' = \rho\pi r^2 = \rho C_a A \quad \text{and} \quad F_a = \rho C_a A \dot{u} \quad (2.15)$$

in which  $r$  is the radius of the cylinder and  $C_a$  is the added mass coefficient.

The Froude-Krylov force represents for the pressure gradient that is present due to the acceleration of the fluid, in the undisturbed region of the flow. This pressure gradient can be described with:

$$\frac{\partial p}{\partial x} = -\rho \frac{du}{dt} \quad (2.16)$$

in which  $u$  is the velocity far from the object. With the assumption of a constant pressure gradient, the force acting on a cylinder is given by (Sumer and Fredsoe, 2006):

$$F_p = \rho A \frac{du}{dt} = \rho A \dot{u} \quad (2.17)$$

Combining equation 2.15 and 2.16 with the in-line drag force results in:

$$F = \frac{1}{2} C_d \rho D u |u| + \rho C_a A \dot{u} + \rho A \dot{u} \quad (2.18)$$

By writing  $C_m = C_a + 1$  and rewriting  $A$  in terms of diameter, this results in the Morison equation as mentioned in Equation 2.11. The drag force is dependent on velocity and the inertia force on acceleration, which results in a 90 degree phase difference for these forces. Figure 2.12 gives example of the output signals of velocity, drag force, inertia force and the total force over the same time period. From this figure, the phase difference becomes clear. In case of a drag-dominated situation, the peak of the total force coincides with the peak in the velocity. In an inertia-dominated situation, the peak coincides with the maximal gradient in the velocity.

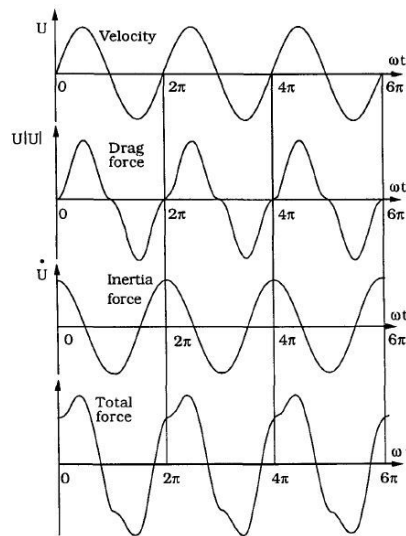


Figure 2.12: Example of the phase difference between velocity, acceleration, drag force and inertia force (Sumer and Fredsoe, 2006).

The orbital motion discussed in Section 2.2.1 describes a horizontal and vertical velocity component. As the original Morison equation was developed for vertically submerged cylinders, only the horizontal velocity component is taken into account. However, for this research also horizontal cylinders are applied, which requires it to take also the vertical velocity into account. To capture this, the Morison equation is adapted for horizontal and vertical force (Chaplin, 1988; Li and Lin, 2010):

$$F_x = \frac{1}{4}C_{mx}\rho\pi D^2\dot{u} + \frac{1}{2}C_{dx}\rho D u\sqrt{u^2 + v^2} \quad (2.19)$$

$$F_z = \frac{1}{4}C_{mz}\rho\pi D^2\dot{v} + \frac{1}{2}C_{dz}\rho D v\sqrt{u^2 + v^2} \quad (2.20)$$

### Surface irregularities

Increasing the roughness of the surface can have impact on the force coefficient discussed before. Various aspect of the flow will be affected by the roughness, such as the angle of separation of vortices, the turbulence or vortex strength (Sumer and Fredsoe, 2006). Research by Justesen (1989) show that for an increase in roughness, the drag coefficient will increase and the inertia coefficient will decrease (Figure 2.13a and 2.13b). Although for the inertia coefficient it seems that the effect of increasing the roughness is limited. However, this research was performed for  $Re$ -numbers in the range of  $10^5$ , highly turbulent flow. The roughness was defined as  $k/D$ , in which  $k$  is the Nikuradse equivalent sand roughness.

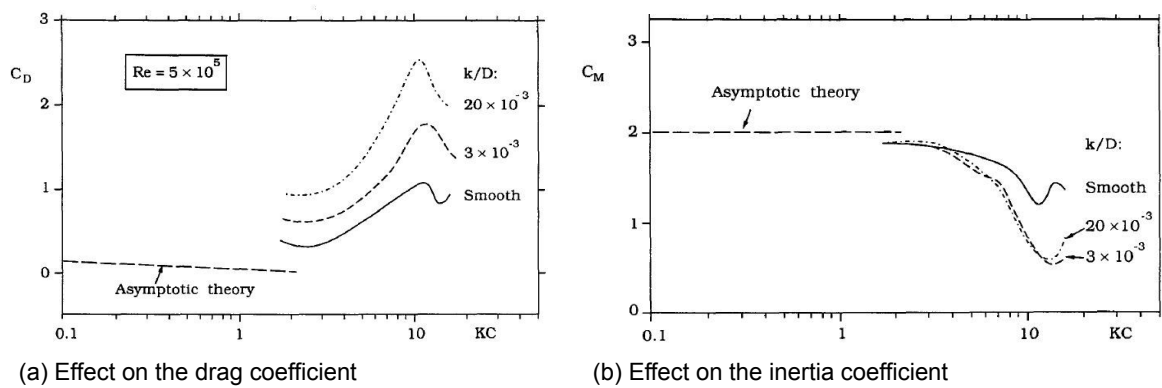


Figure 2.13: Effect of surface roughness on the in-line force coefficients (Sumer and Fredsoe, 2006)

### 2.2.3. Waves through an array of cylinders

#### Sheltering

In the previous section, the forces and coefficients were considered for the case of a single cylinder. However, as multiple cylinders are applied in the structure, they may influence each other by sheltering and induced turbulence by vortex shedding as discussed in Section 2.2.2. Bokaian and Geoola (1984) studied how the drag and lift coefficient of a trailing cylinder were influenced by the interaction between the cylinders. Based on their results, Nepf (1999) calculated the contours of the drag coefficient in relation to their relative distance. Her results are shown in Figure 2.14. This shows that the drag coefficient for the trailing cylinder decreases for a decreasing relative distance. This behaviour is also shown in his results with random arrays of cylinders. Figure 2.15 shows the bulk drag coefficient for different array densities, in which the dimensionless density is defined as:

$$ad = \frac{d^2}{\Delta S^2} \quad (2.21)$$

with  $d$  the cylinder diameter and  $\Delta S$  the mean spacing between the cylinders. The reduction of the drag coefficient follows from two properties of the wake (Nepf, 1999): First, as the downstream cylinder is (partly) in the wake of the leading cylinder, the impact velocity is

lower as a result of the velocity reduction in the wake. Second, the turbulence generated by the wake of the leading cylinder moves the point of separation on the trailing cylinder. This results in a lower pressure differential around the cylinder and thus a lower drag.

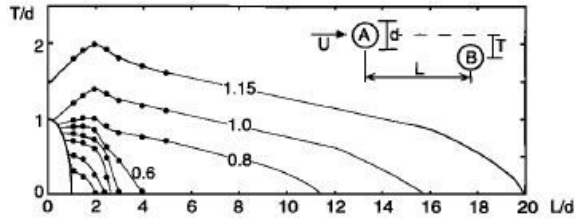


Figure 2.14: Contours of the drag coefficient for the trailing cylinder, depending on their relative distance (Nepf, 1999).

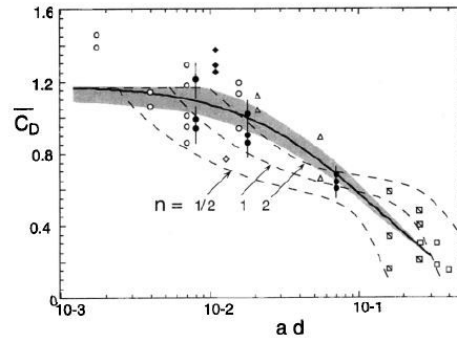


Figure 2.15: Bulk drag coefficient as a function of the dimensionless density  $ad$  (Nepf, 1999).

### Wave dissipation

When a wave hits the array of cylinders, different processes take place. As the structure blocks part of the cross section, a percentage of the incoming energy is reflected. Another percentage is dissipated by the work done on the structure and the energy that is left will transmit through the structure and penetrate into the sheltered zone behind the structure. This balance is visualized in Figure 2.16 and can be summarized as:

$$E_i = E_r + E_{diss} + E_t \tag{2.22}$$

in which  $E_i$  is described by Formula 2.4,  $E_r$  is the reflected energy,  $E_{diss}$  is the dissipated energy and  $E_t$  is the transmitted energy.

Dividing all the terms in Equation 2.22 by  $(1/8)\rho g H_{in}^2$  gives:

$$1 = \left(\frac{H_r}{H_i}\right)^2 + \left(\frac{H_{diss}}{H_i}\right)^2 + \left(\frac{H_t}{H_i}\right)^2 = C_r^2 + C_{diss}^2 + C_t^2 \tag{2.23}$$

in which  $C_r$  is the reflection coefficient,  $C_{diss}$  is the dissipation coefficient and  $C_t$  is the transmission coefficient. If the wave heights are known from experiments, the dissipation by the structure can be calculated.

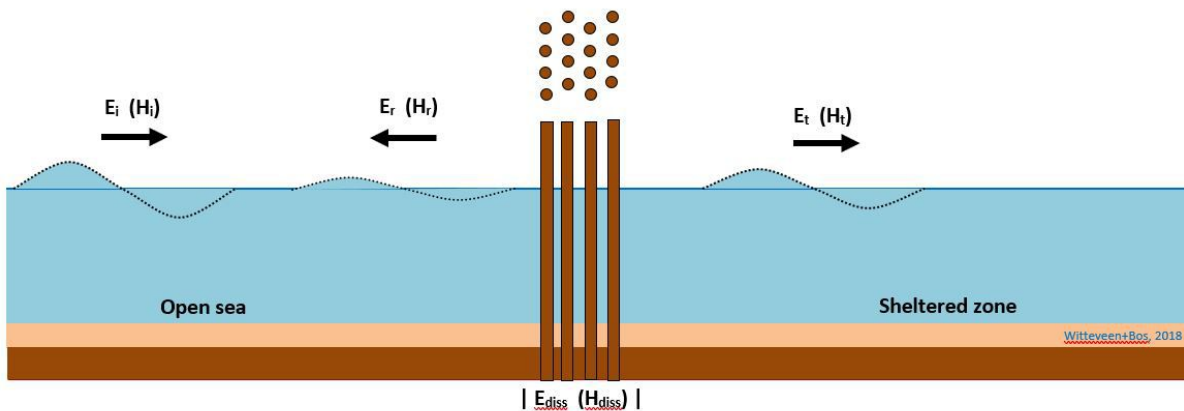


Figure 2.16: Simplified energy balance for an incoming wave interacting with a permeable structure (Adapted from Witteveen+Bos, 2018).

The energy is dissipated by the work done on the structure and can be calculated based on the conservation of energy, assuming linear wave theory and normal incident waves on a straight coastline (Mendez and Losada, 2004):

$$\frac{\partial E_i c_g}{\partial x} = -\epsilon_v \quad (2.24)$$

in which  $c_g$  is the wave celerity and  $\epsilon_v$  the energy dissipation per unit horizontal area. The depth-integrated  $\epsilon_v$  can be calculated with:

$$\epsilon_v = W = \int_0^{h_v} F u dz \quad (2.25)$$

in which  $h_v$  is the submerged cylinder height. Assuming that the velocity can be determined from linear wave theory, Dalrymple et al. (1984) expressed this as:

$$\epsilon_v = \frac{2}{3\pi} \rho C_d D N \left( \frac{kg}{2\omega} \right)^3 \frac{\sinh(kh_v)^3 + 3\sinh(kh_v)}{3k \cosh(kh_v)^3} H_i^3 \quad (2.26)$$

He then rewrote Equation 2.24 for a horizontal bottom, which after solving the differential equation gives an expression for the transmitted wave height in relation to the incoming wave height:

$$K_v = \frac{H_t}{H_i} = \frac{1}{1 + \beta x} \quad (2.27)$$

With:

$$\beta = \frac{4}{9\pi} C_d D N H_i k \frac{\sinh(kh_v)^3 + 3\sinh(kh_v)}{(\sinh(2kh) + 2kh)\sinh(kh)} \quad (2.28)$$

Under the assumption that the velocity can be determined from linear wave theory, Equation 2.27 and 2.28 can be used to determine the drag coefficient  $C_d$  based on the incoming and transmitted wave heights from experiments.

Dalrymple et al. (1984) developed his equation to describe the wave dissipation in vegetation, which has a relatively high porosity. He therefore neglected the reflection, as this would have only a small contribution to the total energy reduction. (If 20% of the wave height is reflected, this leads to a reflected energy of only 4% since energy is related to the wave height squared (Mendez and Losada, 2004)). Porosity's in this research are lower, which means reflection cannot be neglected in advance and the energy balance of Equation 2.22 is applied. The porosity is defined as:

$$n = 1 - \frac{Area_{piles}}{Area_{total}} \quad (2.29)$$

As mentioned earlier, the expression is also based on the assumption of undisturbed velocities inside the structure, as the vegetation has an open structure. To include the effect of a reduced cross section of the flow in case of lower porosity's, a constricted velocity based on the element diameter and spacing is suggested (Ozeren et al., 2014; Stone and Shen, 2002):

$$u_c = \frac{u}{1 - \frac{D_v}{\lambda_s}} \quad (2.30)$$

in which  $\lambda_s$  is the spacing between the elements. The model of Dalrymple et al. (1984) only includes horizontal velocities, for the work done in vertical direction is assumed to be negligible for vertical elements such as vegetation.

## 2.3. Previous experiments on wave dissipation

Vegetation such as salt marshes and mangroves form a natural coastal protection (Hu et al., 2014). To understand the principles, many studies have been done to determine the effect of vegetation on wave dissipation. The studies use different schematized models as rigid cylinders, plastic strips and live vegetation in the experiments. The model with rigid wooden cylinders corresponds best with the permeable structure with vertical elements. The difference with the current research is the effect of configuration. Live vegetation is positioned randomly, which is in most studies represented by a staggered configuration. As current research focuses on a permeable structure, different configuration designs are possible and tested. Table 2.3 gives an overview of relevant studies and some specifications.

Table 2.3: Overview of relevant research.

Research	Model	Waves/ Current	Findings
Hu et al. (2014)	Rigid cylinders	Waves + Current	$C_d = 0.08 + \left(\frac{2200}{Re}\right)^{2.4}$ $2200 < Re < 18000$
Ozeren et al. (2014)	Rigid cylinders	Waves	$C_d = 1.5 + \left(\frac{6.785}{KC}\right)^{2.22}$ $R^2 = 0.21$
Mendez and Losada (2004)	Flexible real vegetation	Waves	$C_d = 0.47 \exp(-0.052 * KC)$ $3 \leq KC \leq 59$
Bradley and Houser (2009)	Flexible real vegetation	Waves	$C_d = 253.9 * KC^{-3.0}$ $0 < KC < 6$
Chen et al. (2018)	Data from Hu et al. & Losada et al.	Waves + current	<i>For waves only:</i> $C_d = 6.94 * KC^{-0.72} + 0.87$ <i>For waves + current:</i> $C_d = 12.89 * KC^{-1.25} + 1.17$ <i>For waves only:</i>
Losada et al. (2016)	Flexible real vegetation	Waves + current	$C_d = 0.08 + \left(\frac{50.000}{Re}\right)^{2.2}$ <i>For waves + current:</i> $C_d = 0.25 + \left(\frac{75.000}{Re}\right)^9$
Jadhav et al. (2013)	Flexible real vegetation	Waves	$C_d = 70 * KC^{-0.86}$ $25 < KC < 135$

Part of the experiments in Table 2.3 use the calibration method as described in Section 2.2.3. Another method to calculate the drag and inertia coefficient is the direct measurement method, as used by Hu et al. (2014).

To apply this method, the force on a cylinder and the impact velocity have to be measured at the same location inside the structure. With the signals in phase, Hu et al. (2014) calculated the  $C_d$  directly from the work done on the structure:

$$C_d = \frac{2 \int_{-\pi/\omega}^{\pi/\omega} F_d u dt}{\int_{-\pi/\omega}^{\pi/\omega} \rho h_v D u^2 |u| dt} \quad (2.31)$$

The inertia is neglected in this calculation, under the assumption that the work done by the inertia force is zero over a full wave period.

## 2.4. Reference situation in the Demak region, Indonesia

### 2.4.1. Hydrodynamic conditions

#### Prediction Witteveen + Bos

For the design of a permeable structure, Witteveen + Bos made a prediction of the design wave conditions. The application area of the permeable structures is at the inter tidal area,

which means a changing water level with the tide. For the Demak region, the prediction of the average water depth varies with the tide between 0.2 and 1.2 meter. The significant wave height varies between 0.2 and 0.5 meter for daily conditions and between 1.0 and 1.5 meter for storm conditions, with a mean period between 3 and 5 seconds. An overview of these wave conditions is shown in Figure 2.17. Due to the shallow foreshore with slopes of 1:1000 that can stretch for 1 kilometer, refraction in the coastal zone is negligible and waves approach the coast approximately perpendicular.

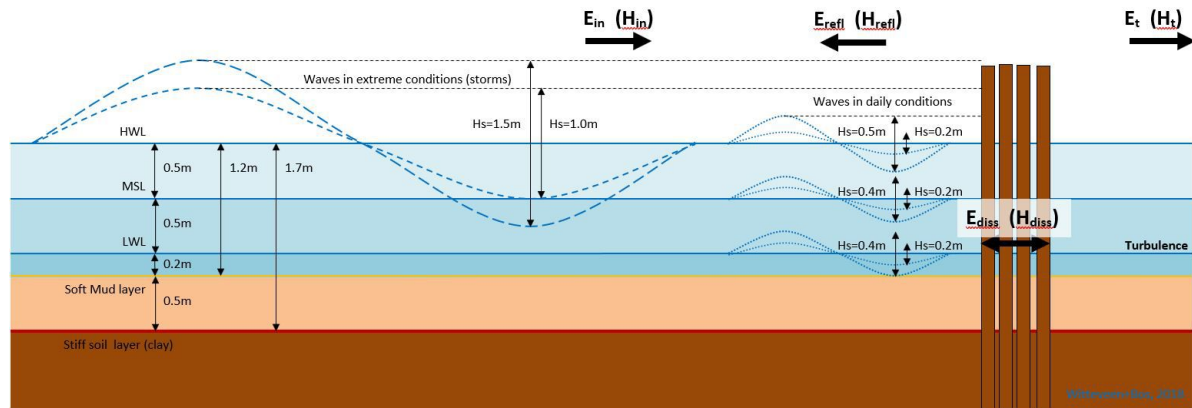


Figure 2.17: Averaged wave heights for daily and storm conditions (Adapted from Witteveen+Bos, 2018).

### Field measurements BioManCo

In the winter period of 2018, field measurements were performed by the BioManCo project. During this period, they measured the daily conditions around the structure, as no storm occurred. The measured wave period and water depth reasonably agree with the prediction made by Witteveen + Bos. However, the significant wave height during daily conditions is significantly lower, with values between 0.05 and 0.2 m.

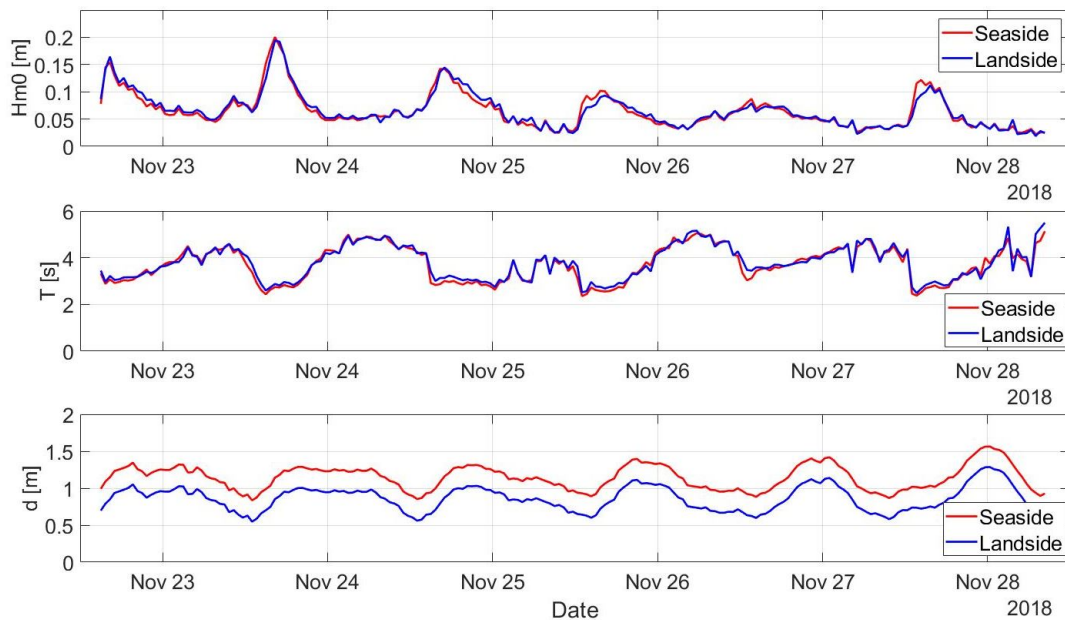


Figure 2.18: Field conditions as measured by the BioManCo project, at the land- and seaside of a structure with vertical poles, see Figure 2.19a (BioManCo, 2018).

From the figure it is observed that the wave characteristics do not significantly vary between the land- and seaside of the structure. For the depth, a reduction of about 0.3m is observed.

### 2.4.2. Applied structures

The structures currently applied/ studied, are built up from bamboo poles in different configurations, sometimes in combination with brushwood filling material. Figure 2.19 gives some examples of the study by BioManCo (2018). As there is not so much research done on these structures, they are build on engineering judgment.

#### Vertical poles

Figure 2.19a shows a structure of vertical poles, which have a diameter of 12-15 centimeter and are place in a staggered configuration. The width of the dam is 1.4 meter, with an average of 10 poles /m<sup>2</sup>. As bamboo is a natural material and located at the water surface, it is subject to deterioration. Without protection, the poles last for only 3 years, which is why they are packed in fiber.

#### Vertical and horizontal poles

Figure 2.19b shows a combination of vertical and horizontal poles. As wave cause a motion in both horizontal and vertical direction, these structures are expected to dissipate more energy. The horizontal poles are applied in the upper part of the water column and have a diameter of 9 centimeter. The structure has a width of 1 meter. The construction of these structures is however quite labor intensive, as it is difficult to fixate the horizontal elements at the right location.

#### Brushwood

Figure 2.19c shows an example of the combination of vertical poles with brushwood filling. As the brushwood has a diameter of 2 centimeter and is densely packed, the porosity of these types of structures is significantly lower. The width of these structures is 50 - 75 centimeter. Also for these structures, the construction and maintenance is labor intensive. On the one side, the brushwood filling wants to float, which has to be restrained by ropes. On the other side, part of the brushwood filling is lost due to subsidence into the soft mud, which requires constant restoration of the filling.



(a) Vertical poles, packed in fiber as protection against ship worm.



(b) Combination of vertical and horizontal poles.



(c) Vertical poles with brushwood filling. (Horizontal poles for stability)

Figure 2.19: Different types of permeable structures studied in Demak, Indonesia (BioManCo, 2018).

Based on the hydrodynamic conditions and the structure dimensions, the characteristic values for each structure are determined. The results are presented in Table 2.4, which gives the extreme values for the measured quantities. This gives an indication of the field conditions.

Table 2.4: Characteristic values for the reference wave conditions, with the extreme values for the measured quantities.

d [m]	H [m]	T [s]	Vertical <sup>1</sup>		Horizontal		Brushwood	
			Re	KC	Re	KC	Re	KC
0.5	0.05	3.00	14520	3.0	10890	4.0	2420	18.2
		5.00	17400	6.0	13050	8.1	2900	36.3
	0.20	3.00	62760	13.1	47070	17.4	10460	78.5
		5.00	-	-	-	-	-	-
1.5	0.05	3.00	6840	1.4	5130	1.9	1140	8.6
		5.00	7680	2.7	5760	3.6	1280	16.0
	0.20	3.00	27720	5.8	20790	7.7	4620	34.7
		5.00	33120	11.5	24840	15.3	5520	69.0
	0.50	5.00	89820	31.0	66960	41.3	14880	186.0

<sup>1</sup>Calculated for a diameter for 12 cm.



# 3

## Methodology: First set of experiments

The first set of experiments focuses on the wave attenuation and reflection of different configurations. Section 3.1 gives a description of the set-up of the physical model in the wave flume with the location of the instruments, followed by the configurations of the model itself. Section 3.2 presents the wave conditions to which the model is subjected in the experiments, with a connection to the situation in Demak. Section 3.3 explains the way the data is gathered by the instruments, followed by the way of processing the data in Section 3.4.

### 3.1. Set-up physical model

#### 3.1.1. Set-up wave flume

The experiments are performed in the wave flume of Delft University of Technology, which has a length of 40m, a width of 0.80m and a maximum water depth of 1.0m. The flume is designed for the purpose of wave experiments, but also combinations with currents are possible. In this research, only pure wave cases are considered with a constant water depth of 0.60m. The wave generator is located at the beginning of the flume and is equipped with an Automatic Reflection Compensation (ARC). It is capable of producing regular and irregular waves, with specifications to be defined by the user. The model is located at a distance of 18.20m from the wave generator, approximately at the middle of the flume. At the end of the flume, a mild slope of approximately 1:3 is created to absorb the transmitted wave and reduce reflection towards the model. Figure 3.1 shows a schematic overview of the set-up.

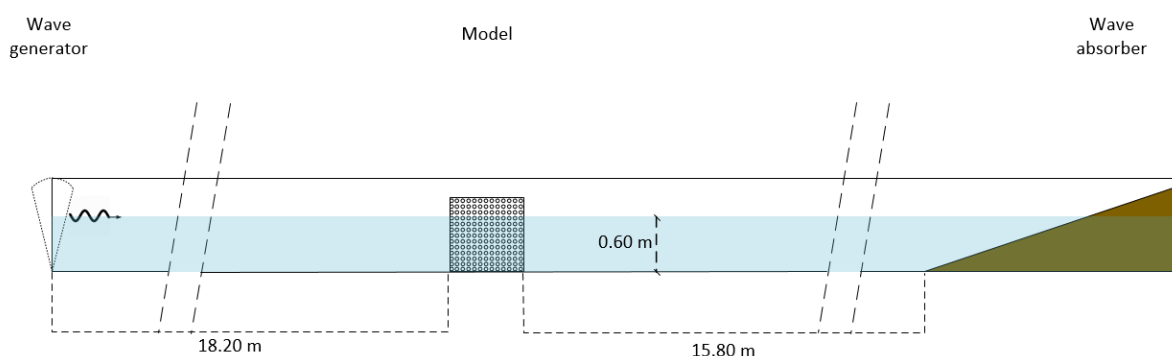


Figure 3.1: Schematic overview of the model in the wave flume. Not to scale.

#### 3.1.2. Model dimensions

The model is designed based on the prototype dimensions and environmental conditions that apply in the study area of Demak, Indonesia, in combination with the constrictions imposed by the wave flume.

After taking into account a margin in order to be able to place the model in the flume, the structure has a 'length' of 78cm (transverse direction in the flume). As both in vertical and horizontal set-up the same configurations are tested, it is advantageous to make the model rotatable. For this purpose, the model has a square frontal area with a height of 78cm, equal to the width.

To determine the diameter of the model, a scaling ratio of 1:4 is used. The diameter of the prototype in Indonesia is 12-15cm, which corresponds to a model diameter of 3-4cm following from the scaling rules:

$$\lambda = \frac{\text{Length scale prototype}}{\text{Length scale model}} = \frac{L_p}{L_m} \quad (3.1)$$

$$D_{\text{prototype}} = \lambda D_{\text{model}}$$

in which  $\lambda$  is the scaling factor. To maximize the possible effect of the increase in diameter, elements of 4cm are used. Using the scaling factor from Equation 3.1 on the width, gives a model width of 0.35-0.38m. Based on the properties of the grid and the configurations (see Section 3.1.3), a width of 0.40 m is chosen. In the whole research, calculated quantities are on model scale.

The water depth is determined by the wave properties. Minimizing the non-linear effects in waves gives a minimum water depth of 0.60m (based on the results of Haage (2018)). An overview of the prototype and model dimensions is given in Table 3.1.

Table 3.1: Comparison of real and model dimensions

	Reference case	Scale model
Diameter [m]	0.12 - 0.15	0.04
Width [m]	1.4-1.5	0.40 / 0.76
Length [m]	Not relevant	0.78 (flume width)
Height [m]	Not relevant (Emerged)	0.78
Water depth [m]	0.2 - 1.2	0.60

Figure 3.2 shows the actual aluminum model with an example of a vertical configuration in Figure 3.2a and a horizontal configuration in Figure 3.2b. The elements are fixed on the top and bottom side by a grid, which is shown in Figure 3.2c.



Figure 3.2: View of the complete model with different orientations. The black elements are for recording purposes.

The total grid of the structure can be filled with  $13 \times 13 = 169$  elements. By leaving out part of the elements, different configurations can be made, with different porosity's. With an element spacing of 2cm, the minimum porosity that can be tested is  $n = 0.64$ , with  $n$  defined as in Equation 2.29.

### 3.1.3. Model configurations

Four different configurations are designed, based on their porosity and the relative distance of the elements. As the configurations are tested for half the width ( $0.40m$ ) and the full width ( $0.76m$ ), it gives a total of 8 configurations. The design contains two uniform configurations ( $n = 0.64$  &  $n = 0.89$ ), the see the effect of porosity. To see the effect of arrangement, the staggered and longitudinal configuration are included. The relative distance of the element in the direction of the wave propagation is the same in both configurations, but the placement of the elements differs. A top view of all eight configurations is shown in Figure 3.3.

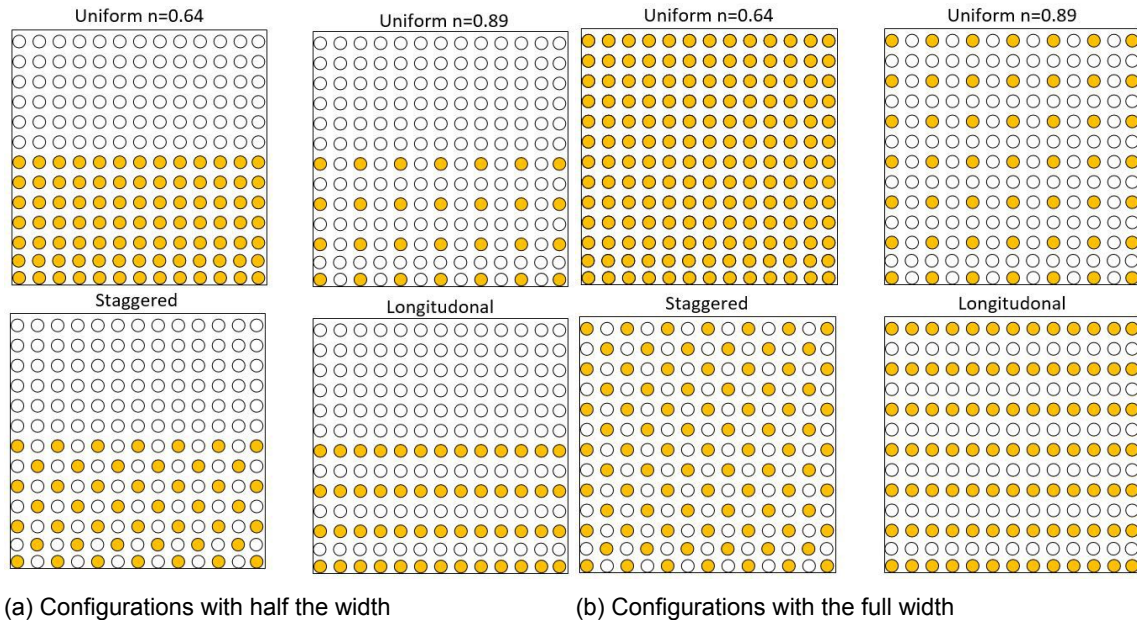


Figure 3.3: Overview of the tested configurations: Uniform with  $n=0.64$ , uniform with  $n=0.89$ , staggered and longitudinal. This is a top view for the vertical setup, with the waves coming in from the bottom of the figure.

All the configurations are tested in vertical and horizontal setup, which gives a total of 16 different configurations. These are presented in Table 3.2, with their characteristic values.

Table 3.2: Tested configurations with their characteristics

Name	Orientation	Width [m]	Porosity	Number of elements
V040U064	Vertical	0.40	0.64	91
V040U089	Vertical	0.40	0.89	28
V040L	Vertical	0.40	0.79	52
V040S	Vertical	0.40	0.82	46
V076U064	Vertical	0.76	0.64	169
V076U089	Vertical	0.76	0.89	49
V076L	Vertical	0.76	0.79	91
V076S	Vertical	0.76	0.82	85
H0405U064	Horizontal	0.40	0.64	91
H040U089	Horizontal	0.40	0.89	28
H040L	Horizontal	0.40	0.79	52
H040S	Horizontal	0.40	0.82	46
H076U064	Horizontal	0.76	0.64	169
H076U089	Horizontal	0.76	0.89	49
H076L	Horizontal	0.76	0.79	91
H076S	Horizontal	0.76	0.82	85

### 3.2. Wave conditions

In reality, an irregular wave field is present with varying wave heights and periods (see Section 2.4). However, as a first step to understand the basic physical processes, regular waves are studied to understand the effect of different wave conditions.

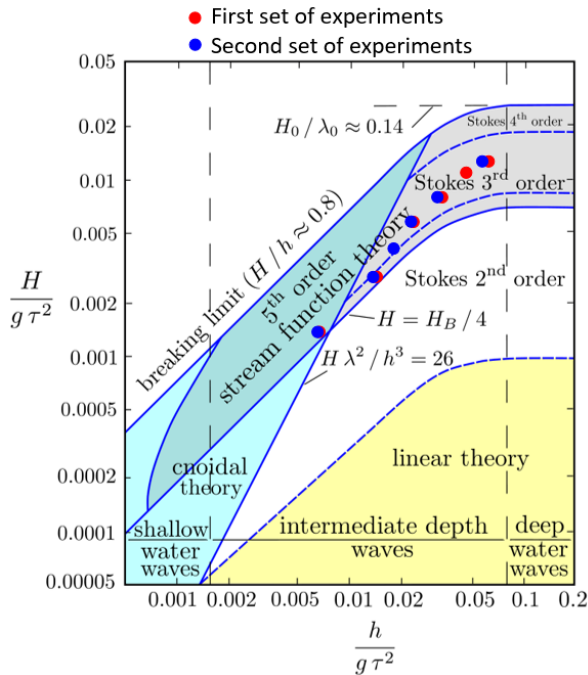


Figure 3.4: Validity regions of different wave theories (Le Mehauté, 1976). The plot shows the wave conditions used in the first and second set of experiments.

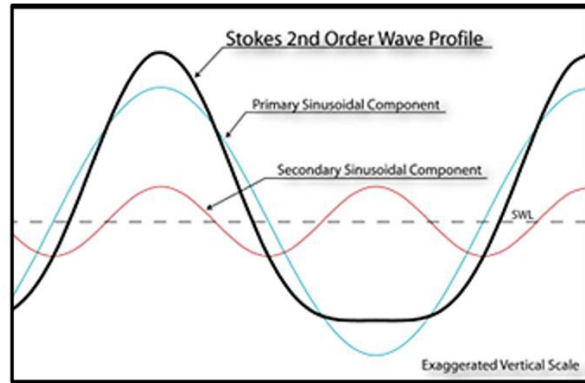


Figure 3.5: From a linear wave to a 2nd order Stokes wave. The vertical scale is exaggerated. The blue line is a linear wave. Interaction with a second component (red) changes the shape to a non-linear wave (black).

This study focused on linear waves as discussed in Section 2.2.1, or waves close to that. Figure 3.4 shows the region in which this theory is valid. However, in reality the wave field is not linear but consists of more components; the higher order Stokes waves and cnoidal waves. Figure 3.5 gives an example of the change in shape if the primary sinusoidal component (blue) interacts with a secondary sinusoidal component (red). The resulting 2nd order Stokes wave (black) has a sharp peak and a long, flat trough.

Based on the scaling factor  $\lambda$  from Froude scaling, the scaling rules for the wave height, wave period and force can be determined:

$$\begin{aligned} H_{prototype} &= \lambda H_{model} \\ T_{prototype} &= \sqrt{\lambda} T_{model} \\ F_{prototype} &= \lambda^3 F_{model} \end{aligned}$$

Applying these rules makes sure that the Froude number (ratio of inertia forces to gravitational forces) is the same for the prototype and the scale model. Table 3.3 presents the wave parameters used in this study, based on the scaling rules and previous experiments of Haage (2018).

Table 3.3: Overview of the environmental conditions for the reference case and the model case.

	Reference case	Model case
Wave height H [m]	0.2 - 1.5	0.13
Wave period [s]	1.0 - 5.0	1.0 - 2.0

The 1-2 seconds interval is divided into 5 wave conditions. Table 3.4 presents the conditions and some of their characteristic values based on the wave height and velocity.

Table 3.4: Tested wave cases with their characteristic values.

Name	H [m]	T [s]	d [m]	Re	KC	H/d	H/L
T100	0.13	1.00	0.60	6665	4.2	0.22	0.08
T113	0.13	1.13	0.60	7351	5.2	0.22	0.07
T125	0.13	1.25	0.60	7868	6.1	0.22	0.06
T150	0.13	1.50	0.60	8638	8.1	0.22	0.04
T200	0.13	2.00	0.60	9451	11.8	0.22	0.03

The different configurations together with the wave conditions form a large set of unique experiments. To structure the data, each experiment is assigned a unique name with the parameters of the experiment in it:

$$\underbrace{H}_{1} \underbrace{040}_{2} \underbrace{U064}_{3} \underbrace{T100}_{4} - \underbrace{1}_{5}$$

In which:

- 1 - Horizontal (H) / Vertical (V) configuration
- 2 - Width of the structure (0.40 m/ 0.76 m)
- 3 - Type of configuration (U064/ U089/ L/ S)
- 4 - Wave period
- 5 - Take 1 / Take 2

### 3.3. Data gathering

To distinguish between an incoming wave and a reflected wave, the method of Goda and Suzuki is applied (See Appendix A). To apply this method, two wave gauges in front of the model (1 & 2) are used to measure the height of the incoming wave and the reflected wave from the model. Two wave gauges at the back of the model (3 & 4) are used to measure the transmitted wave and the reflected wave from the absorber. To calculate the height of the incoming and reflected wave, the distance between the wave gauges and the model must be at least 20% of the wave length. The distance between the two wave gauges themselves must be 25% of the wave length, which means that the wave gauges are relocated for every wave case. See Figure 3.6 for an overview of the location of the measurement equipment.

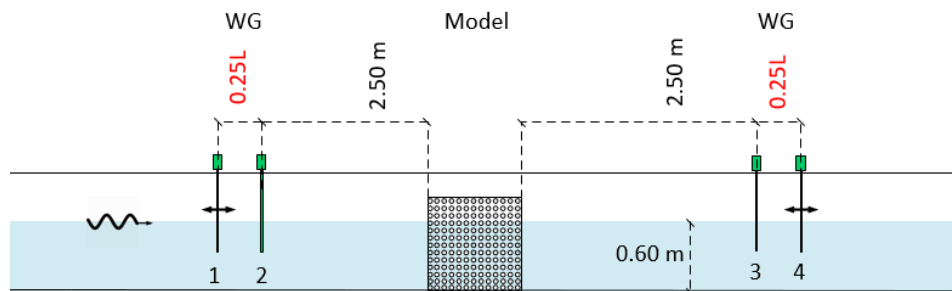


Figure 3.6: Schematic overview of the location of the wave gauges. The distance between the wave gauges marked in red varies for every wave condition. Not to scale.

The wave gauges measure the water level based on the conductivity of water, with a frequency of 1000Hz. The computer connected to the wave gauges generates an output record with values varying between -10V and +10V. As the relationship between water level and voltage is linear, calibration can be done by varying the water level.

### 3.4. Data processing

The data generated by the four wave gauges, is combined into one ASC-file by the software DasyLab. This data file containing the signals in Volt is then processed in a Matlab script, using the method of Goda and Suzuki to determine the incoming and reflected wave amplitude and the reflection coefficient. The flow diagram in figure 3.7 shows the different steps.



Figure 3.7: Flow diagram of processing the results in Matlab.

As the script takes the signal of 2 wave gauges as input, the calculation has to be done twice for every wave condition. The first time for wave gauges 1 and 2, the second time for wave gauges 3 and 4. The resulting parameters are:

- $A_{in}$  - Incoming wave amplitude
- $A_{r1}$  - Reflected wave amplitude from the model
- $C_{r1}$  - Reflection coefficient from the model
- $A_t$  - Transmitted amplitude
- $A_{r2}$  - Reflected amplitude from the wave absorber
- $C_{r2}$  - Reflection coefficient from the wave absorber

In the processing of the results and in the analysis of this research, the actual measured values are used. All quantities are on the scale of the model in the flume.

#### 3.4.1. Dissipation

With the wave amplitudes and reflection coefficients known, the energy dissipated by the structure is determined based on the conservation of energy, as described in Section 2.2.3:

$$E_{diss} = E_i - E_r - E_t \quad (3.2)$$

$$\left(\frac{H_{diss}}{H_i}\right)^2 = \left(\frac{H_i}{H_i}\right)^2 - \left(\frac{H_r}{H_i}\right)^2 - \left(\frac{H_t}{H_i}\right)^2 \quad (3.3)$$

$$C_{diss}^2 = 1 - \left(\frac{H_r}{H_i}\right)^2 - \left(\frac{H_t}{H_i}\right)^2 \quad (3.4)$$

#### 3.4.2. Computation interval

To determine the right interval for calculating the terms of the energy balance, the dissipation for successive intervals is determined for the configurations V035U064, V035L and H068L. The results for the different wave conditions applied on V035U064 are shown in Figure 3.8. The trend in the results for the configurations V035L and H068L is similar, but less extreme (See Appendix C.1 and C.2). From the figure, it can be seen that the situation requires some time to develop, as the first points are slightly lower. For the longer wave periods ( $T = 1.25s$ ,  $T = 1.50s$ ,  $T = 2.00s$ ), the situation then becomes stable with a constant level of dissipation.

However, for the wave periods of  $T = 1.00s$  &  $T = 1.13s$ , the dissipation changes drastically around 60-70 seconds. Looking at Figure 3.8a, the dissipation seems to increase with almost 15%. Around the same period, a drop in dissipation followed by a strong increase can be observed in Figure 3.8b. From physical observations during the experiments, these phenomena can be attributed to a transverse wave that develops in the flume over time. This observation is also supported by velocity measurements with an ADV under the same conditions in a later experiment (see Appendix B.3). As the transverse wave also influences the level of the water surface, the determination of the wave dissipation becomes more difficult.

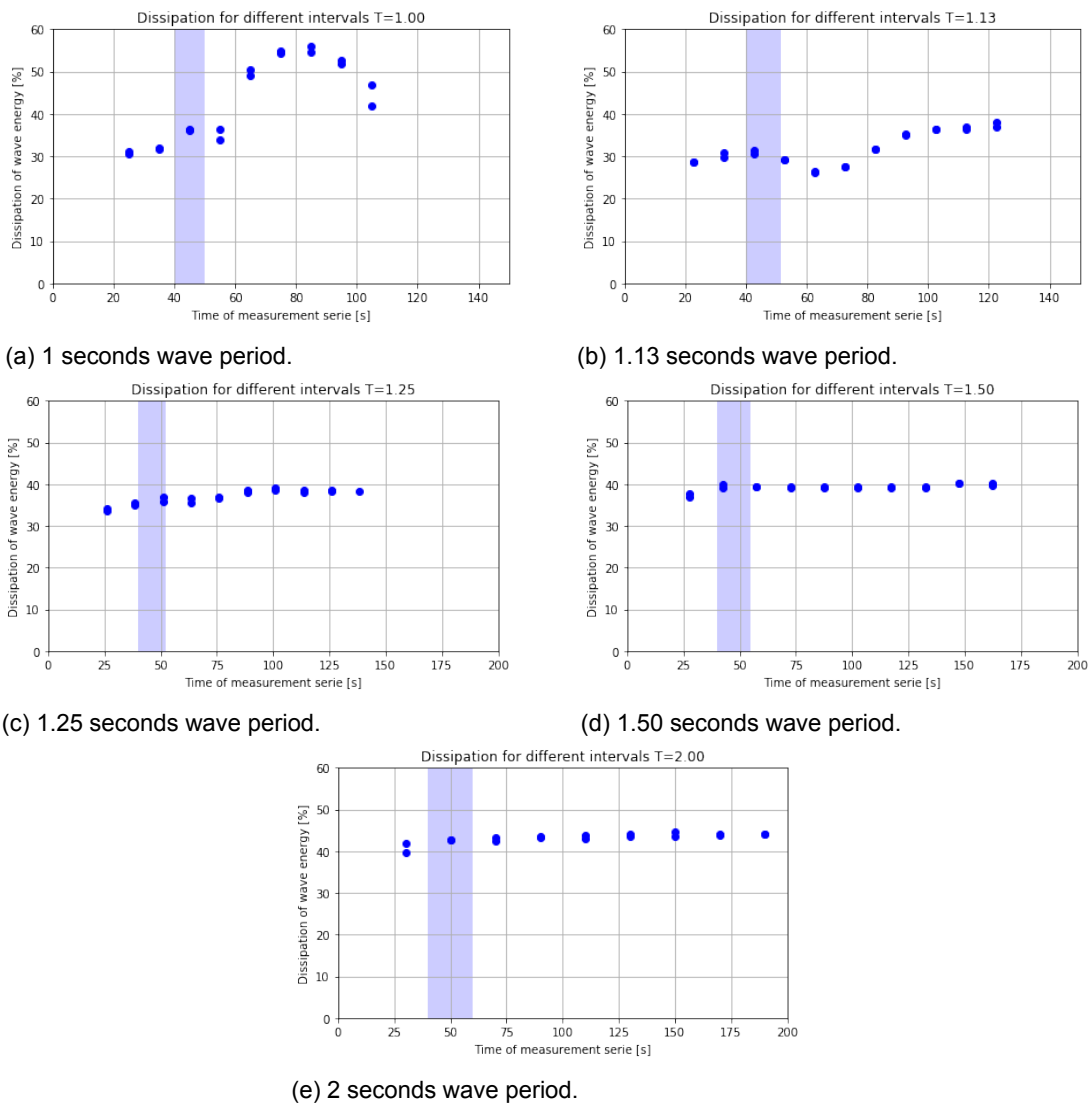


Figure 3.8: Dissipation as a percentage of the incoming energy, calculated for successive intervals in different wave conditions. The first movement of the water surface observed by the wave gauges is at  $t = 0$ . The interval marked in blue is the interval used for further calculations.

As the transverse waves causes 3D effects and complicates the calculations, the interval for further calculations is chosen such that these effects are excluded. Also taking into account the time required for development of the situation, it is decided to start the interval at 40 seconds after the first movement of the water surface is registered by the wave gauges. The required length of the interval is 10 wave periods, which means that the total time is different for every wave condition. Figure 3.9 gives a clarification of this method.

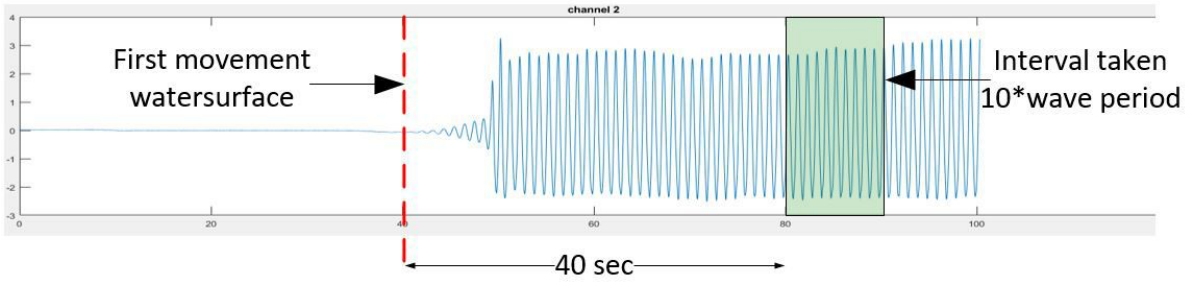


Figure 3.9: Example of the interval taken for calculation, starting 40 seconds after the first movement of the water surface.

### 3.4.3. Drag coefficient calibration from wave energy dissipation

#### Vertical elements

The drag coefficient for the vertical elements is calculated based on the calibration method with the theory of Dalrymple, as described in Section 2.2.3. In this calculation, the inertia component is assumed to be negligible, as is the vertical force component. With the velocity from linear wave theory, first the theoretical wave transmission is calculated for every value of  $C_D$  between 0 and 10 according to:

$$Ct = \frac{H}{H_i} = \frac{1}{1 + \beta x} \quad (3.5)$$

$$\beta = \frac{4}{9\pi} C_d b_v N H_i k \frac{\sinh(kh_v)^3 + 3\sinh(kh_v)}{(\sinh(2kh) + 2kh)\sinh(kh)} \quad (3.6)$$

To determine the drag coefficient for the measured dissipation, the measured transmission is compared with the theoretical values of transmission (See Figure 3.10). Based on the minimum absolute error, the drag coefficient is determined. As reflection might play a role for the low porosity configurations, the incoming wave height  $H_i$  in Equation 3.5 and 3.6 is corrected for this by subtracting the reflected energy, resulting in a slightly lower incoming wave height. The result of the calibration is a bulk drag coefficient averaged per element,  $\overline{C_D}$ .

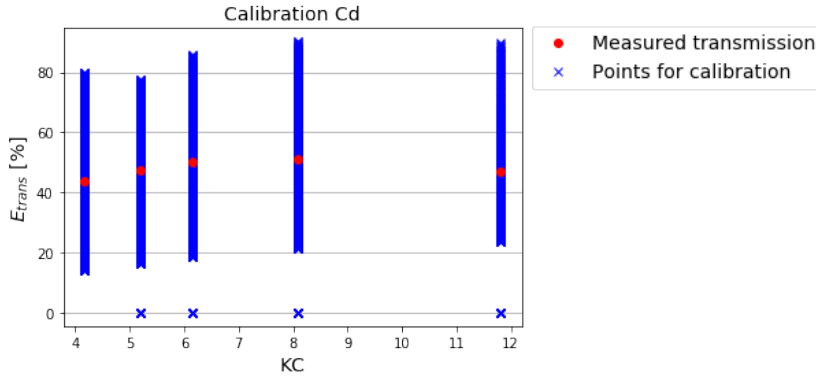


Figure 3.10: Calibration of  $C_d$  by comparison of the theoretical and measured transmission.

#### Horizontal elements

For the horizontal elements, the force in both the horizontal and vertical direction has to be taken into account. Suzuki et al. (2019) introduced the effect of the vertical force component by adapting the expression for beta:

$$\beta = \frac{4}{9\pi} C_d b_v N H_i k \frac{\sinh(kh_v)^3 + 3\sinh(kh_v) + \cosh(kh_v)^3 - 3\cosh(kh_v) + 2}{(\sinh(2kh) + 2kh)\sinh(kh)} \quad (3.7)$$

This expression is still a simplification, but results in a lower and more realistic value for  $C_d$ .

## Results: First set of experiments

This chapter presents the results of the scale model tests. In Section 4.1, the total energy balance for the different configurations and wave conditions is presented. In Sections 4.2 and 4.3, this balance is taken apart and the focus is more on the dissipation. Several parameters are discussed, also to make the comparison with the results for the 2cm model of Haage (2018).

### 4.1. Energy balance

Based on the energy balance described in Section 3.4.1, the incoming wave energy is decomposed into reflected energy, transmitted energy and dissipated energy. The range of the components is shown in Figure 4.1, divided into the vertical and horizontal configurations and plotted against the wave period. The reflection component is generally in the range of 0-10% of the incoming energy, with some outliers around 20% for the most dense configuration. This corresponds to a wave height reduction of around 4% for  $n > 60\%$ . For these porosity's, this won't affect the energy balance so much. The transmission component is between 30-85% for the vertical and between 10-85% for the horizontal configurations. This results in a dissipation component between 10-65% for the vertical configurations and between 15-90% for the horizontal configurations. The energy balances for every configuration separate are presented in Appendix E.1, with their exact values in the tables.

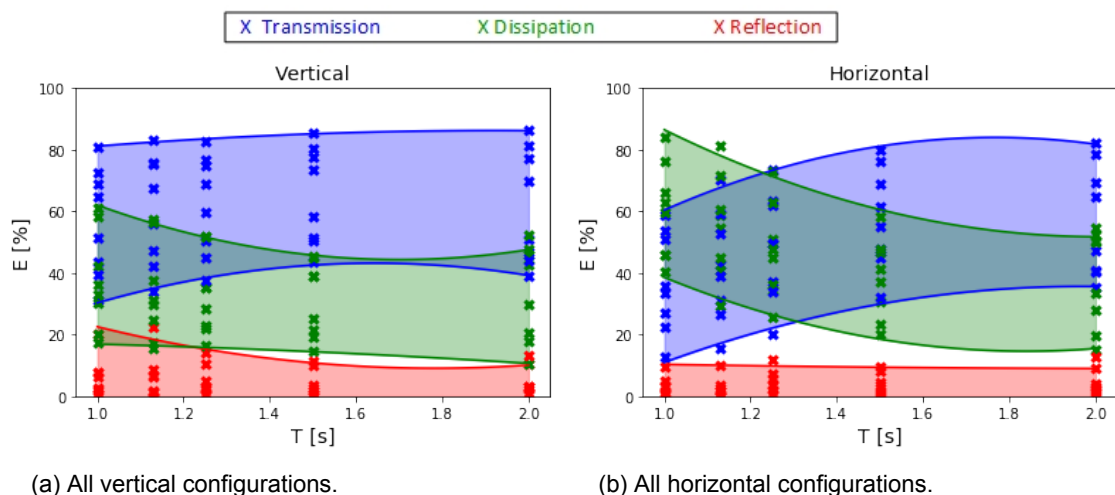


Figure 4.1: Energy balance for all the different configurations, plotted against the wave period. The lines are fitted through the most extreme points, to show the range of the components.

It can be concluded from the figure that the range of dissipation is the same in the vertical and horizontal configurations for wave periods around  $T = 2.0s$ . For wave periods around  $T = 1.0s$  however, the horizontal configurations dissipate 10-20% more energy than the vertical ones.

## 4.2. Relationship between configuration and dissipation

By focusing on the dissipation component of the energy balance, the influence of different structure parameters is investigated. These results will be used to answer the first sub-question of Section 1.3:

1. How does the dissipation of wave energy change for different configurations and wave conditions?

### 4.2.1. Total dissipation

Following from the literature study, the dissipation in terms of energy is plotted against the  $KC$ -number, as this parameter includes information about the oscillatory motion relative to the diameter. The  $KC$ -number is determined based on the undisturbed velocity from linear wave theory and the element diameter. It also allows for a comparison with previous research. The results of the different configurations are split into four sections, depending on their configuration and orientation. First, the vertical configurations with half the width and the full width are presented (Figure 4.3), followed by the horizontal configurations with half the width and the full width (Figure 4.4). The results are compared based on four different characteristics of the structure. A recap of the configurations, with their respective colour in the graphs is given in Figure 4.2.

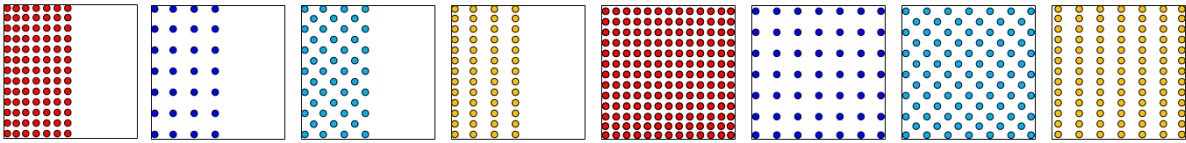


Figure 4.2: Recap of the configurations, with colour indication. The right side of the figure is always the front side of the model. For the horizontal configurations this is a side view, for the vertical configurations a top view.

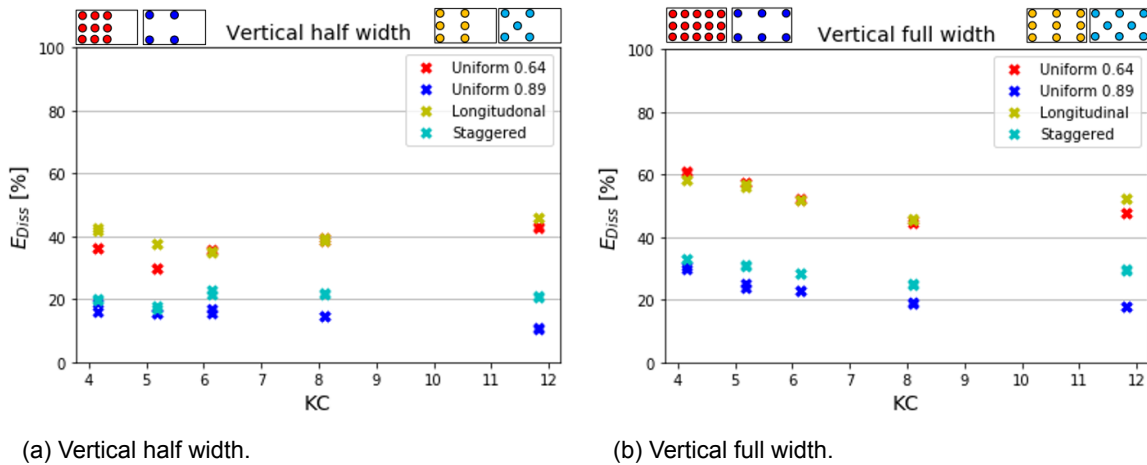


Figure 4.3: Total dissipation for the vertical configurations. Each configuration and wave condition is tested twice, which gives only a slight difference for some wave conditions. Larger  $KC$  represents longer waves.

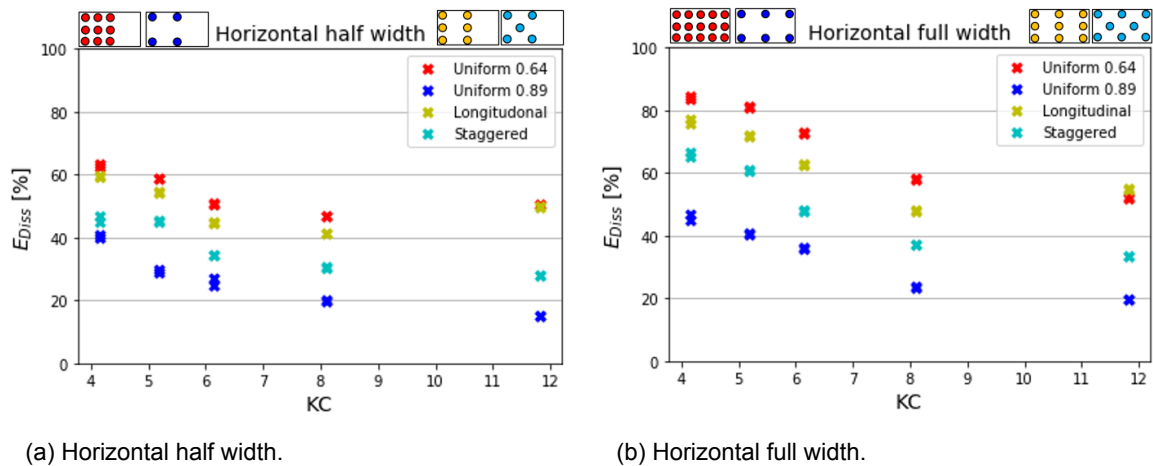


Figure 4.4: Total dissipation for the horizontal configurations. Each configuration and wave condition is tested twice, which gives only a slight difference for some wave conditions. Larger  $KC$  represents longer waves.

### Effect of wave condition

For the vertical half width configurations (Figure 4.3a), the dissipation is fairly constant over the wave conditions, with values between 20-40%. The spread becomes larger for the longer excursion<sup>1</sup>, but no clear increase or decrease is distinguished. For the full width configuration (Figure 4.3b), a slight decrease ( $\pm 10\%$ ) in dissipation is observed for increasing wave period.

For the horizontal configurations (Figure 4.4a & 4.4b), the dissipation is high for  $KC \approx 4.0$  ( $T = 1.0s$ ) and it decreases with 20-30% for increasing wave period, for both the half width and full width configurations. The difference in dissipation between the configurations is quite constant over the wave conditions.

### Effect of configuration

The different configurations are distinguished by colour in Figure 4.3 and 4.4. For the vertical orientation, the uniform dense configuration and the longitudinal configuration cause the most and almost the same dissipation. For some wave conditions, the longitudinal dissipates even more than the uniform one. The staggered and uniform open configurations dissipate in the order of 20-30% less energy.

For the horizontal orientation, the order in the amount of dissipation is more clear. The uniform dense configuration dissipates most, followed by the longitudinal, the staggered and last the uniform open configuration. The spread in dissipation over the configurations is up to almost 40%.

### Effect of width

Increasing the width of the structure from 0.40m to 0.76m causes an increase in dissipation. This increase is strongest for  $KC \approx 4.0$  ( $T = 1.0s$ ) in both the vertical and horizontal orientation, with a factor varying between 1.1 and 1.5 depending on the configuration. For  $KC \approx 12$  ( $T = 2.0s$ ), the factor is approximately 1.1. The factors are the same for the vertical and horizontal orientation.

### Effect of orientation

The effect of orientation is negligible for the larger  $KC$ -numbers, as dissipation for both orientations is the same (compare the right hand side of the four figures). For the  $KC$ -numbers however, a strong increase in dissipation is observed (in the order of 20%) if the orientation is changed from vertical to horizontal. This effect is visible for all configurations, with for both the half width and the full width an increase in the order of 20%.<sup>2</sup>

<sup>1</sup>For the longer waves, the reflected energy from the wave absorber is larger (order 3-8% of imposed incoming energy). The reflected wave might interact with the incoming wave, influencing the wave height measurements and thus the dissipation.

<sup>2</sup>During the experiments, the wave gauge on position 1 broke down. The instrument was replaced and calibrated, but this might have had an effect on the configurations H076U064, H076U089, H076L and H076S, which were executed with the replaced

### 4.2.2. Dissipation per element

The configurations all contain a different number of elements. To compare the effectiveness of the configurations and see whether sheltering plays a role, the average dissipation per element is calculated by dividing the total dissipation by the number of elements used in the configuration. The results are plotted in Figure 4.5 and 4.6.

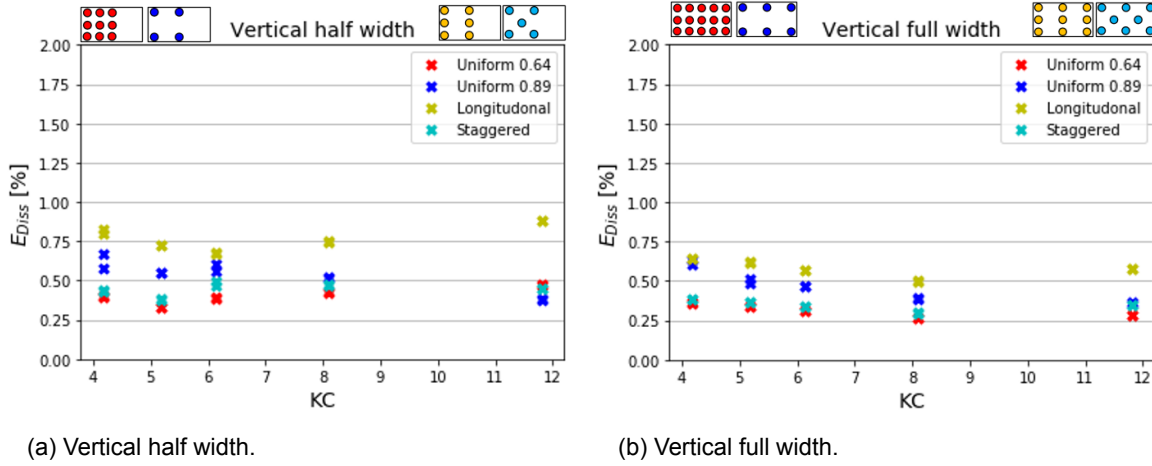


Figure 4.5: Dissipation per element for the vertical configurations. Each configuration and wave condition is tested twice, which gives only a slight difference for some wave conditions. Larger  $KC$  represents longer waves.

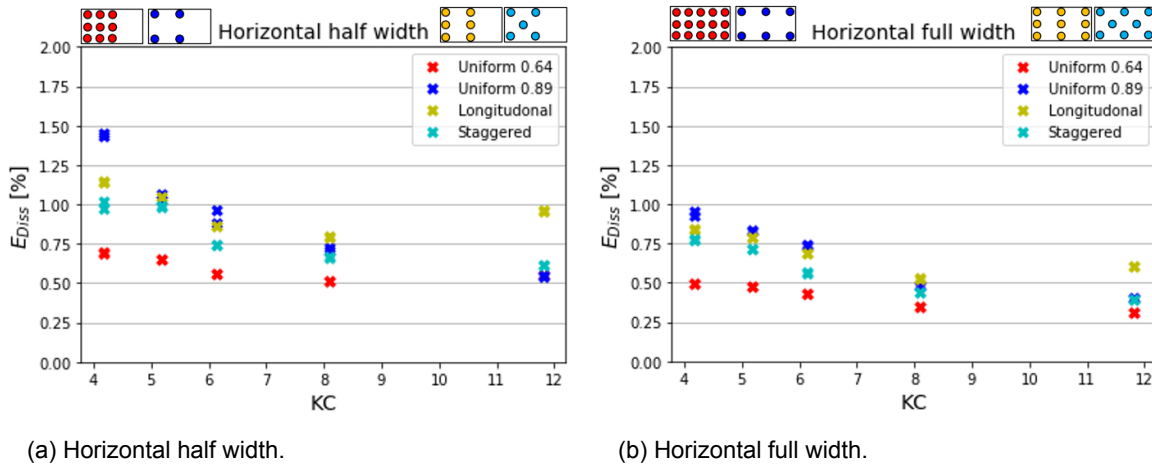


Figure 4.6: Dissipation per element for the horizontal configurations. Each configuration and wave condition is tested twice, which gives only a slight difference for some wave conditions. Larger  $KC$  represents longer waves.

As can be seen in graphs, the order of the configurations changes completely for the dissipation per element. The uniform dense configuration, which has the highest total dissipation, appears to have the lowest dissipation per element for both the vertical and horizontal orientation. The uniform open configuration, which has a low total dissipation, appears to have relatively high dissipation per element. The longitudinal configurations performs well in both the total dissipation and the dissipation per element. Interesting to see is that for the vertical orientation, the staggered configurations performs the same as the uniform dense one. However, for the horizontal orientation the staggered one performs much better than the uniform dense configuration (factor of 1.3).

Another aspect observed in the graphs is that the average dissipation per element is larger for the half width configurations, especially for the horizontal orientation (factor of 1.5).

instrument. The measured incoming wave height was larger than in previous tests, which might result in a larger dissipation.

### 4.2.3. Drag coefficient by Dalrymple

To compare the obtained results with previous research, the bulk drag coefficient is determined using the theory of Dalrymple and Suzuki as described in Section 3.4.3. The results are shown in Figure 4.7 and 4.8.

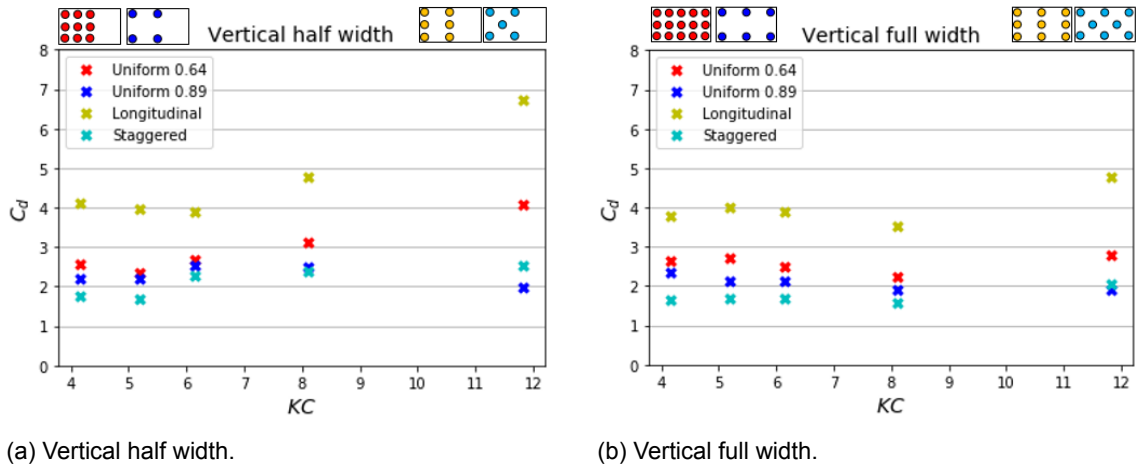


Figure 4.7: Drag coefficient according to the theory of Dalrymple for the vertical configurations. Larger  $KC$  represents longer waves.

For the vertical configurations, the drag coefficient varies between 1.5 and 3, except for the 2-seconds wave and the longitudinal configuration, for which  $C_d$  varies between 3.5 and 7. A strong increase in drag coefficient is observed for an increase in wave length in the uniform dense and longitudinal configuration. By increasing the width of the structure, the bulk drag coefficient becomes slightly lower.

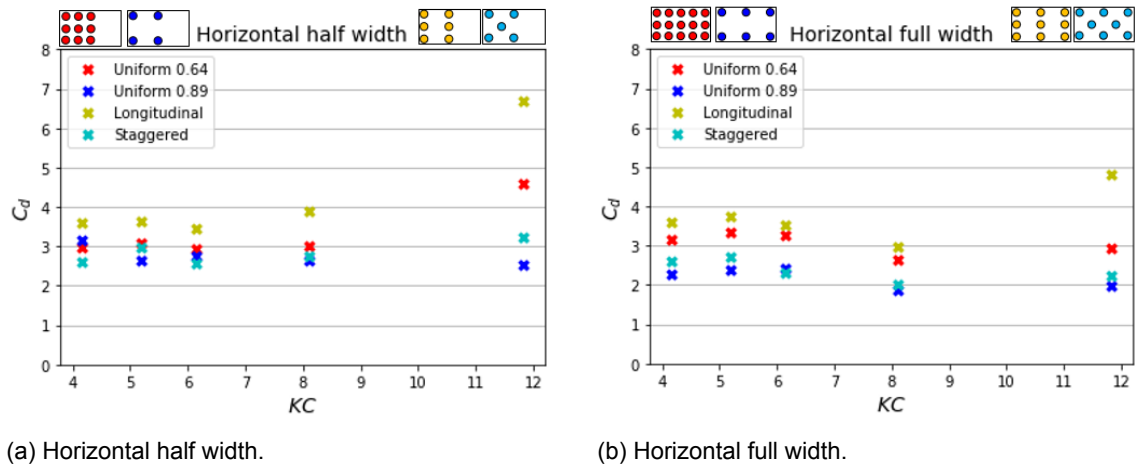


Figure 4.8: Drag coefficient according to the theory of Dalrymple for the horizontal configurations. Larger  $KC$  represents longer waves.

The observed trend for the horizontal orientation is the same as for the vertical orientation, with a slight increase overall. For all the configurations, except the longitudinal, the drag coefficient goes up to a value around 3. For the longitudinal configuration, the drag coefficient goes down for the short waves, while it stays the same for the 2-seconds wave.

### 4.3. Influence of element diameter

By combining the data of the 4cm model with the results of previous research on a 2cm model from Haage (2018), the effect of changing the diameter is studied. The results will be used to answer the second sub-question of Section 1.3:

2. What is the influence of element diameter on wave energy dissipation?

#### 4.3.1. Total dissipation vs. KC number (element diameter)

The first step in the comparison, is plotting the dissipation rates against their respective  $KC$  numbers. In both studies, the same wave conditions and water depths are used. Figure 4.9 shows the results for all the vertical configurations combined and all the horizontal configurations combined. The grey area shows the global trend of the data. As the diameter differs a factor 2, also the  $KC$  numbers for the wave conditions differ a factor 2.

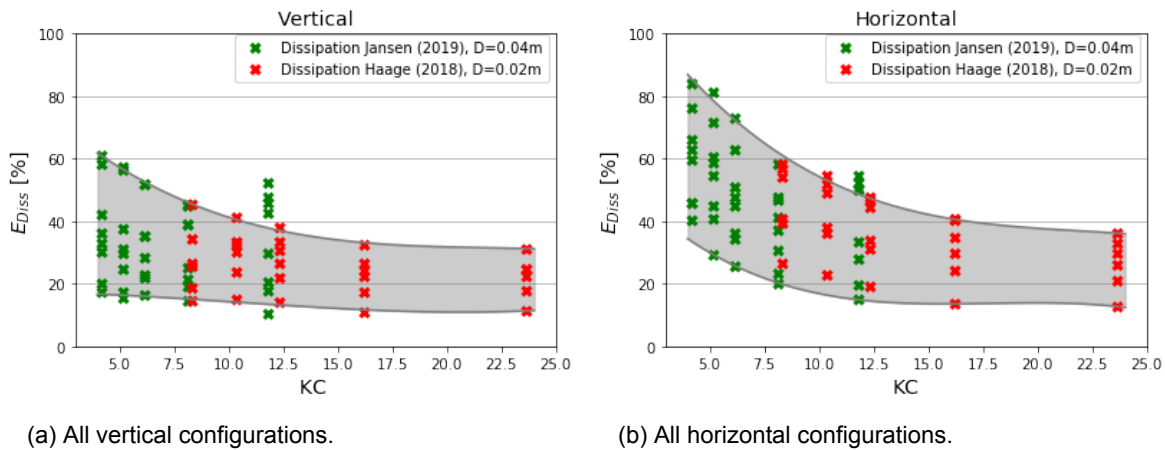


Figure 4.9: Total dissipation for all the configurations, compared with the data of Haage (2018) with a  $D = 2.0$  cm model.

From figure 4.9, a general trend of decreasing dissipation for increasing  $KC$  is observed. However, around  $KC = 12.5$ , a discontinuity is observed between the two data-sets. This suggests that  $Dissipation - KC$  may not be the right parameter set to compare the effect of the diameter.

Also, the dissipation is related to  $u^3$ . As velocity is then expected to be related to the porosity of the structure, it is important to take this into account. The element density is different for each configuration and model, which makes it impossible to compare them quantitatively based on the total dissipation. Dimensionless parameters including variables such as the element density should be defined for a better comparison of the physical processes.

#### 4.3.2. Drag coefficient vs. KC number (element diameter)

To compare the data sets based on a parameter that is independent of element density, an average drag coefficient per element is determined. This coefficient follows from the energy dissipation per unit area and the number of elements in each configuration, according to:

$$C_d = \frac{\epsilon_v}{\frac{1}{2}\rho D h N U^3} \quad (4.1)$$

in which  $\epsilon_v$  is the energy dissipation per unit area as described in Formula 2.24. As formula 4.1 includes both  $D$  and  $N$  in the denominator, it takes into account the porosity. The result is a dimensionless drag coefficient, which is plotted in Figure 4.10. The difference between this approach and the calibration approach by Dalrymple in Section 4.2.3, is that Dalrymple assumes a decay of the wave height through the structure. In the current approach, the

dissipation is assumed to be constant throughout the structure, resulting in lower values for the drag coefficient.

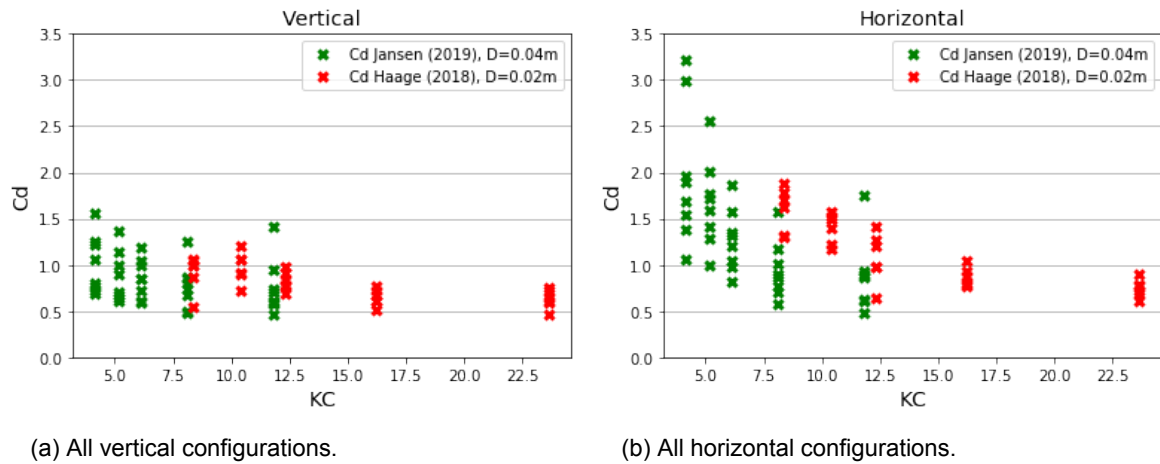


Figure 4.10: Comparison of the simplified drag coefficient, plotted against the KC number based on the element diameter.

From this figure it is observed that both data sets have a  $C_d$  in the same order of magnitude. Also, both sets also show a decrease in  $C_d$  for an increase in  $KC$ . However, the  $KC$  numbers are still a factor 2 apart, which causes again a discontinuity in the data set. This suggests that  $KC$  based on the element diameter on the x-axis might not be the right parameter to compare the results. As the excursion relative to the diameter is quite large, other processes may play a role in an array of elements.

### 4.3.3. Drag coefficient vs. KC number (element spacing)

The  $KC$ -number from Figure 4.10 (which gives information about the water motion relative to diameter) ranges from 4 till 24, while the elements have a spacing of 1-2 diameters. This means that the water particles in motion will encounter more than 1 element on their path, causing a change in the trajectory of the particle. The  $KC$ -number cannot include elements that are in the proximity or the change in flow that they cause, suggesting that it is not the right parameter for an array of elements with small spacing. To capture this physical process better, it is proposed to replace  $KC$  with  $KC^*$ , which is based on the heart-to-heart distance instead of the diameter, according to:

$$KC^* = \frac{UT}{\lambda_s} \quad (4.2)$$

in which  $\lambda_s$  is the heart-to-heart distance between the elements in the direction of wave propagation.  $KC^*$  represents the number of elements that the water particles will encounter on their path. The distances for the different configurations and models is presented in Table 4.1.

Table 4.1: Heart-to-heart distance of the elements in the direction of motion for the different configurations and models.

$\lambda_s$	2cm model (Haage 2018)	4cm model (Jansen 2019)
Uniform dense	4.1 cm	6.0 cm
Uniform open	8.2 cm	12.0 cm
Longitudinal	8.2 cm	12.0 cm
Staggered	8.2 cm	12.0 cm

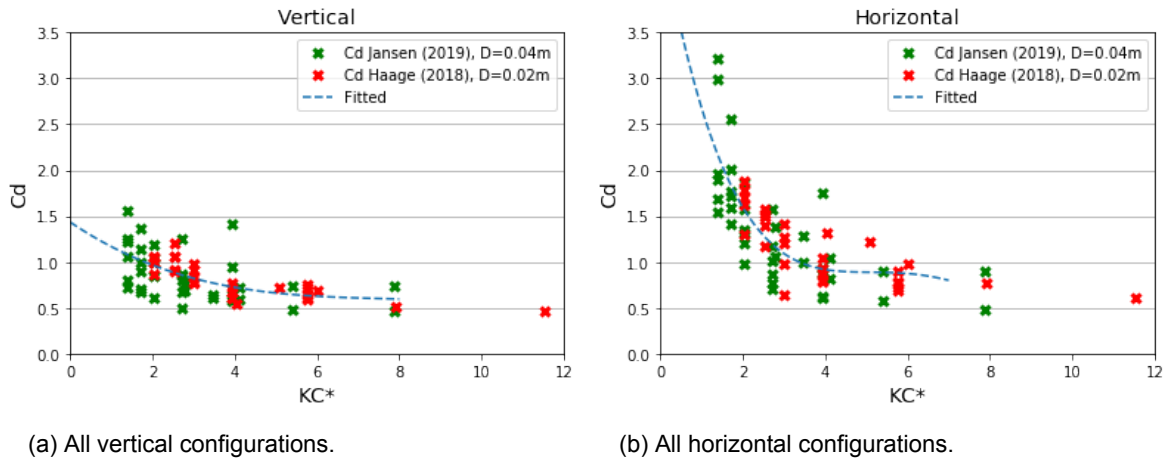


Figure 4.11: Comparison of the simplified drag coefficient plotted against the  $KC^*$  number, which is based on the heart-to-heart spacing of the element in the direction of wave motion.  $KC^*$  indicates how many elements the water particle encounters on its path.

In Figure 4.11, the drag coefficient is plotted against the new  $KC^*$  number. It shows a decrease in drag coefficient for an increase in  $KC^*$ , which suggests that the average drag coefficient per element decreases if the flow encounters more elements in its motion. For the overlapping parts of the plots, the drag coefficient for the 2cm model seems to be slightly larger than for the 4cm model. The values of  $C_d$  range from 0.5 till 1.5 for the vertical orientation, while they reach from 0.5 till 3.5 for the horizontal configuration.

### 4.3.4. Drag coefficient per configuration

The total data set of Figure 4.11 is split into the configurations, in order to see the effect of the diameter for each configuration. As the effect is in the same order for every configuration, only the results for the uniform open configurations are plotted in Figure 4.12. The results of the uniform dense, longitudinal and staggered configurations are presented in Appendix E.2.

The figure shows two trend lines. The dashed line is based on the total data set, containing both the data of the half width and full width configurations. The solid line is based on only the data of the half width configurations. From Figure 4.12 and the data in the appendix, no clear effect of the diameter is observed. The drag coefficients follow the trend line for both data sets, without a significant difference for the diameters. The trend of decreasing  $C_d$  for increasing  $KC$  observed for the total data is also observed for every configuration separately.

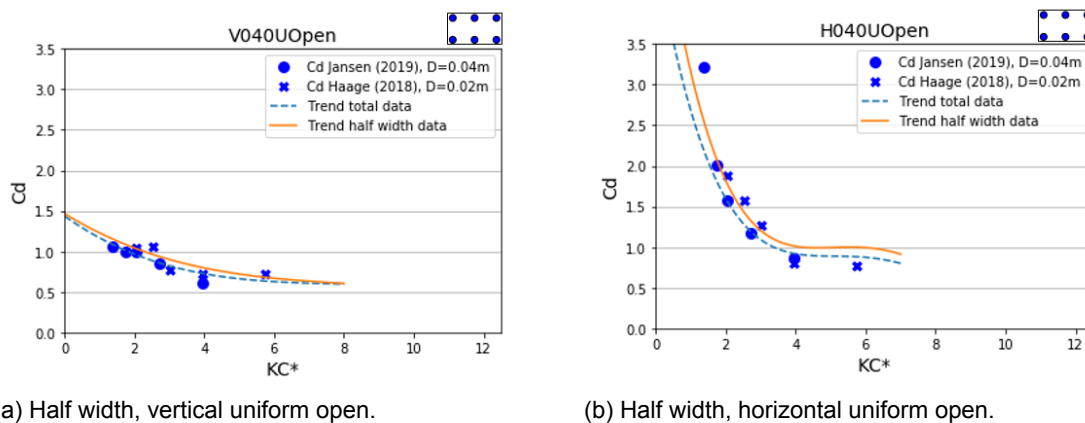


Figure 4.12: Comparison of the dimensionless drag coefficient for uniform open configuration with half the width. The dashed line is based on the data of both the half and full width configurations. The solid line is based on the data of the half width configurations only.

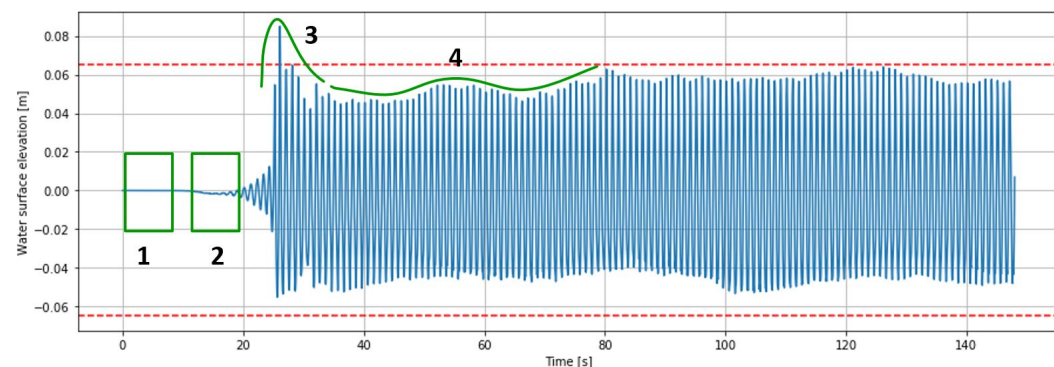
# 5

## Analysis of the results: First set

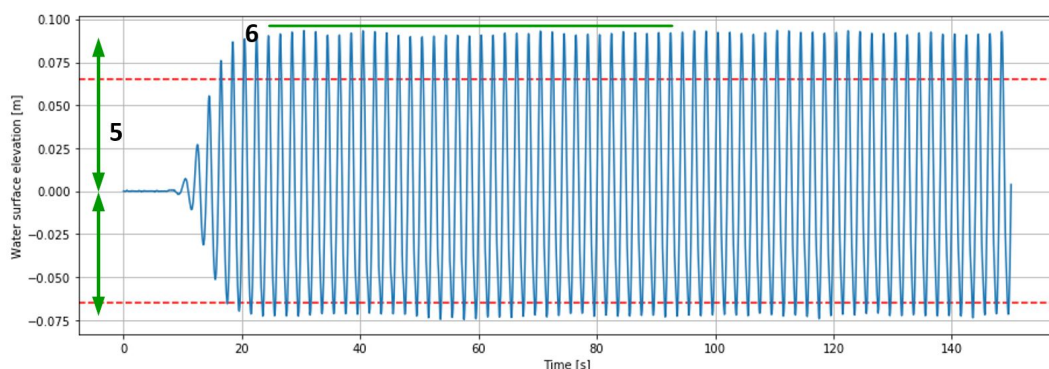
In this chapter, the results from Chapter 4 are analyzed. First, the measured wave signal for a  $T = 1.0\text{s}$  wave and a  $T = 2.0\text{s}$  wave is discussed in Section 5.1. It continues with the effect of the configurations on the dissipation in Section 5.2 by calculation of the amplification factors, followed by the effect of the diameter in Section 5.3. The results and observations are summarized in Section 5.4.

### 5.1. Analysis of wave signal

To understand the behaviour of the structure, the output signals of the wave gauges are briefly discussed in this section. Figure 5.1 shows the output for a short wave 1-second wave and a 2-second wave, followed by a description of some characteristic features.



(a) Water surface elevation for uniform configuration with  $n = 0.64$  and  $T = 1.00\text{s}$ .



(b) Water surface elevation for uniform configuration with  $n = 0.64$  and  $T = 2.00\text{s}$ .

Figure 5.1: Signal of the water surface elevation for 1-second and a 2-second wave, with some interesting features highlighted. The red lines indicate the theoretical amplitude for a perfect sinusoidal wave with a wave height of  $H = 0.13\text{m}$ .

1. For all tests, the first part of the signal represents still water, with a surface elevation that is equal to zero. The signal is already corrected for an offset in the instrument values.
2. For the 1-second waves, sometimes a small decrease in water level can be observed just before the arrival of the waves. This is caused by the activation of the wave board. If the wave board moves to the front (away from the structure), the length of the water volume becomes longer. With a constant volume of water in the wave flume, this induces a slight decrease in water level.
3. For the 1-second waves, sometimes a bump in the signal is observed at the arrival of the first waves. As the wave gauge is at approximately one wave length distance from the model for the short waves, the first reflected waves might reinforce the incoming wave, an effect that fades out after a few waves.
4. For the 1-second waves, the incoming waves strongly interact with the reflected waves from the model. This causes the output signal to have some variation in surface elevation amplitude over time. Due to the interaction, the total surface elevation amplitude is lower than the imposed amplitude.
5. For the 2-seconds waves, a difference is observed between the positive and negative amplitude of the surface elevation. This indicates that for this wave, the wave profile tends towards a cnoidal profile, with sharp peaks and flat troughs.
6. For the 2-seconds waves, the amplitude of the wave is constant over time. The measured surface elevation is larger than the imposed wave amplitude, which can be due to interaction with the reflected wave from the model/ back of the flume. For configurations with lower reflection, the measured amplitude tends towards the imposed amplitude.

## 5.2. Effect of configuration on the dissipation

From studying the results, it is observed that the increase in width and the change of orientation have an effect on the total dissipation, but not so much on the differences in dissipation of the configurations between themselves. Therefore, first the effects of width and orientation are analyzed, before analyzing the effect of the position of the elements.

### 5.2.1. Increasing the structure width

By using the full structure instead of half the structure, the width of the structure increases with a factor of 1.9. However, looking at the results, the increase in dissipation is much smaller. The amplification factors are calculated for all the configurations, orientations and wave conditions. The results are presented in Table 5.1 and 5.2. The average amplification factor for the vertical orientations is around 1.5, slightly bigger than for the horizontal orientations which have a factor of around 1.3. According to the calculated range of amplification factors, the first half of the structure dissipates 65-90% of the energy, suggesting a non-linear correlation between the width and dissipation.

Table 5.1: The total dissipation for all the wave conditions for half the width and the full width, with the amplification factor when changing from half to full width - Vertical orientation.

T[s]	Uniform 0.64			Uniform 0.89			Longitudinal			Staggered		
	Half [%]	Full [%]	F [-]	Half [%]	Full [%]	F [-]	Half [%]	Full [%]	F [-]	Half [%]	Full [%]	F [-]
1.00	36.1	61.0	1.7	17.4	30.3	1.7	42.3	58.2	1.4	20.0	32.9	1.6
1.13	29.9	57.4	1.9	15.4	24.5	1.6	37.8	56.5	1.5	17.4	31.0	1.8
1.25	35.5	52.1	1.5	16.3	22.8	1.4	35.1	52.0	1.5	22.2	28.5	1.3
1.50	39.0	44.9	1.2	14.6	19.0	1.3	38.9	45.5	1.2	21.7	25.1	1.2
2.00	42.9	47.8	1.1	10.6	17.8	1.7	46.0	52.4	1.1	20.7	29.6	1.4
AVG.			1.5			1.5			1.3			1.5

As a result of the dissipation of energy, the wave height reduces throughout the structure, which then leads to a decrease in particle velocity. With the energy dissipation related to the velocity according to:

$$E_{diss} \propto C_d \cdot u^3 \quad (5.1)$$

the wave height reduction results in an exponential decay in dissipation. This explains why doubling the width does not result in double the amount of dissipation.

The effect of wave height reduction is even stronger for the horizontal elements, as for these configurations, the wave energy is also dissipated in the vertical direction. As more energy is dissipated per unit area, the wave height reduction is stronger through the structure. This causes more of the dissipation to take place in the first half of the structure and explains why the amplification factor is slightly lower for the horizontal orientations.

Table 5.2: The total dissipation for all the wave conditions for half the width and the full width, with the amplification factor when changing from half to full width - Horizontal orientation.

T[s]	Uniform 0.64			Uniform 0.89			Longitudinal			Staggered		
	Half [%]	Full [%]	F [-]	Half [%]	Full [%]	F [-]	Half [%]	Full [%]	F [-]	Half [%]	Full [%]	F [-]
1.00	63.1	84.1	1.3	40.4	46.0	1.1	59.6	76.4	1.3	45.8	65.9	1.4
1.13	58.9	81.1	1.4	29.3	40.7	1.4	54.4	71.8	1.3	45.2	60.7	1.3
1.25	50.8	72.8	1.4	25.8	36.0	1.4	44.8	62.7	1.4	34.4	47.9	1.4
1.50	46.8	58.2	1.2	20.1	23.6	1.2	41.4	47.8	1.2	30.6	37.2	1.2
2.00	50.5	52.2	1.0	15.2	19.8	1.3	49.8	54.8	1.1	28.2	33.6	1.2
AVG.			1.3			1.3			1.3			1.3

The effect of increasing the width is largest for the vertical elements and especially for wave periods around  $T = 1.0s$ . For the longer waves, the effect is only marginal. But as the longer waves are more representatives of the reference situation ( $T = 3 - 5s$  in the field), it suggests that increasing the width is not the best option to increase the dissipation.

### 5.2.2. Changing the orientation of the elements

The horizontal elements dissipate energy in both the horizontal and vertical plane, as already shortly mentioned in Section 5.2.1. This behaviour is also observed in the results, with an increase in dissipation when the structure is rotated 90 degrees. For all the configurations, the amplification factor is calculated and presented in Table 5.3.

Table 5.3: Amplification factors of the dissipation for changing the orientation from vertical to horizontal. Calculated with the dissipation values from Table 5.1 and 5.2. ( $F_h$  - Factor half width,  $F_f$  - Factor full width,  $F_a$  - Average factor.)

T[s]	Uniform 0.64			Uniform 0.89			Longitudinal			Staggered		
	$F_h$ [-]	$F_f$ [-]	$F_a$ [-]	$F_h$ [-]	$F_f$ [-]	$F_a$ [-]	$F_h$ [-]	$F_f$ [-]	$F_a$ [-]	$F_h$ [-]	$F_f$ [-]	$F_a$ [-]
1.00	1.7	1.4	1.55	2.3	1.5	1.9	1.4	1.3	1.35	2.3	2.0	2.15
1.13	2.0	1.4	1.7	1.9	1.7	1.8	1.4	1.3	1.35	2.6	2.0	2.3
1.25	1.4	1.4	1.4	1.6	1.6	1.6	1.3	1.2	1.25	1.6	1.7	1.65
1.50	1.2	1.3	1.25	1.4	1.2	1.3	1.1	1.1	1.1	1.4	1.5	1.45
2.00	1.2	1.1	1.15	1.4	1.1	1.25	1.1	1.0	1.05	1.4	1.1	1.25
AVG.	1.5	1.3	1.4	1.7	1.4	1.6	1.3	1.2	1.2	1.9	1.7	1.8

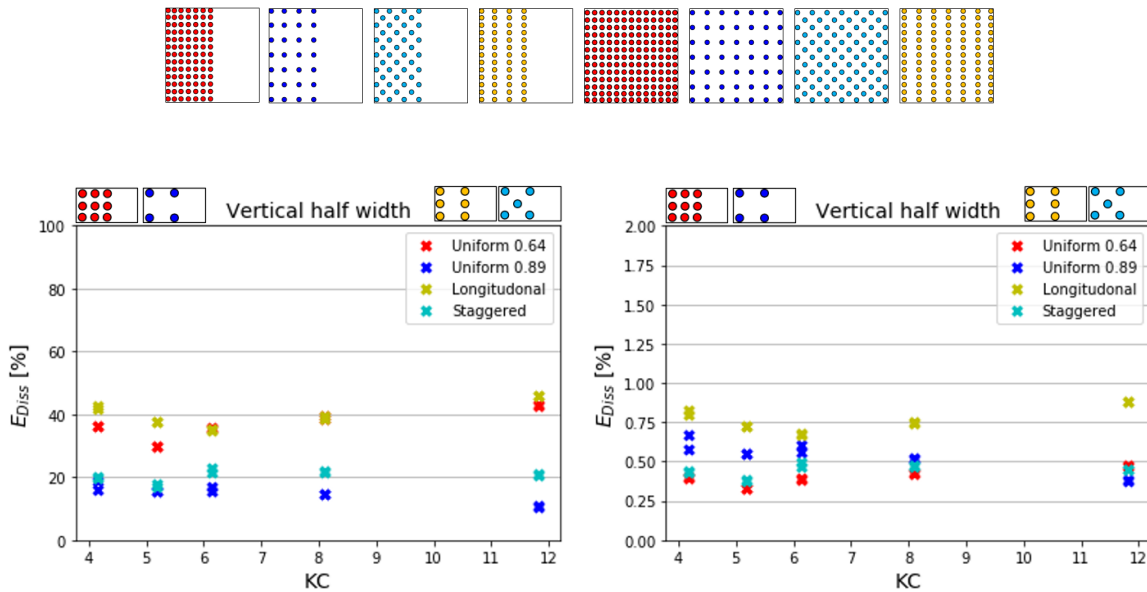
From Table 5.3, it is observed that the effect is strongest for the half width configurations, which can be explained with the mechanism of the previous section. Looking at the difference between the wave conditions, it is again observed that the effect is strongest for wave periods around  $T = 1.0s$ , which is expected based on the vertical velocities of the different conditions. For short waves, the vertical velocities are higher, resulting in more dissipation.

Interesting however are the differences between the configurations. The uniform dense and the longitudinal configurations dissipate the most energy, but rotating them is less effective than rotating the uniform open and staggered configurations. This suggests that in the order of magnitude of the vertical velocities, the vertical distance between the elements might play an important role. For the uniform dense and longitudinal configuration, the heart-to-heart distance is only  $6\text{cm}$ , while for uniform open and staggered ones the distance is increased to  $12\text{cm}$ . With a depth averaged velocity of  $0.09\text{--}0.14\text{m/s}$ , the excursion reaches past the next element for the uniform dense and longitudinal configuration, but not for the uniform open and staggered ones. This suggests that sheltering might play a role in the dissipation. The same trend is observed for the drag coefficient in Section 4.3.3, with a decrease in  $C_d$  for an increase in  $KC^*$ , the number of elements encountered.

### 5.2.3. Changing the positions of the elements

For the analysis, the uniform open configuration is taken as the reference case. Based on this configuration, the effect of adding elements at different positions is investigated. Important factors in the amount of dissipation might be the number of elements and the frontal area per row. As the trend is the same for the half and full width, in this section only the figures of half the width are presented.

For all configurations, adding elements causes an increase in the total amount of dissipation (see Figure 5.2a). However, the location of the added elements seems to be very important for the amount of increase. The longitudinal and staggered configuration have almost the same number of elements (respectively 52 and 46), but the longitudinal configuration dissipates roughly twice the amount of energy. By looking at figure 5.2b, which presents the effectiveness of the elements, it is observed that the effectiveness is only increased for the longitudinal configuration, while for the others the effectiveness decreases. Adding extra rows to the longitudinal configuration to get the uniform dense configuration, does not change much in the total amount of dissipation, but causes a significant drop in effectiveness.



(a) Total dissipation for the vertical half width.

(b) Dissipation per element for the vertical half width.

Figure 5.2: Total dissipation for the vertical configurations. Each configuration and wave condition is tested twice, which gives only a slight difference for some wave conditions. Larger  $KC$  represents longer waves.

A reason for the fact that the increase in dissipation is only small for the staggered configuration, may be found in the vortex shedding. As discussed in section 2.2.2, the tests are in the single or double vortex shedding regime. For the double vortex shedding regime, the vortices move away from the cylinder under an angle of 45 degrees. In case of the staggered configuration, this is exactly the location of the added element. The turbulence induced by the vortex changes the pressure difference over the trailing element, as the point of separation is delayed. This results in a reduced drag coefficient and therefore a lower dissipation. A sketch of the mechanism is depicted in Figure 5.3.

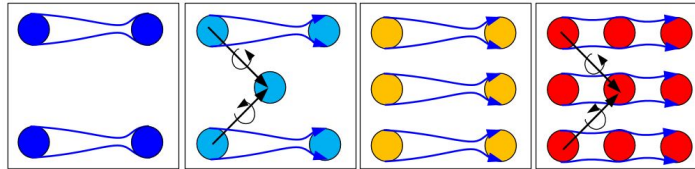
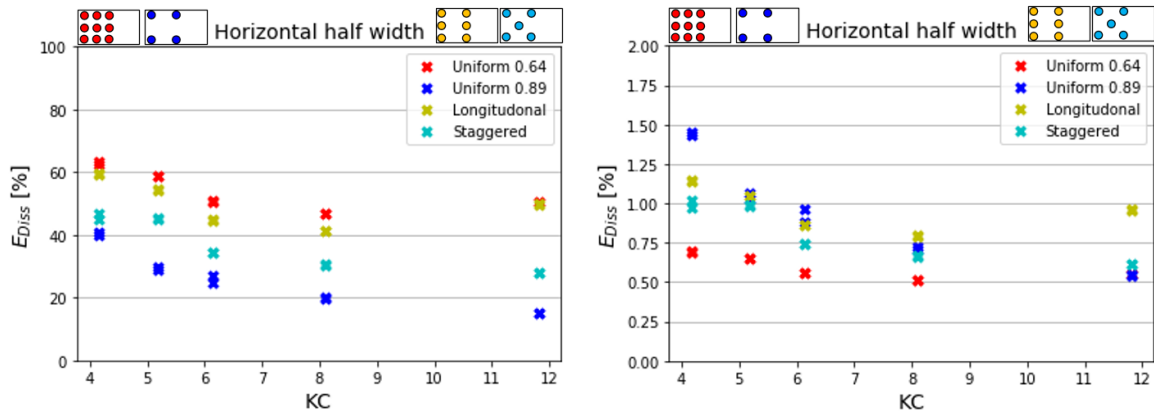


Figure 5.3: A sketch of the mechanisms of vortex shedding and sheltering for the different configurations.

A reason for the fact that the dissipation does not (significantly) increase for the change from the longitudinal to the uniform dense configuration, might be found in the concept of sheltering. The added elements are located in the wake area of the longitudinal rows, which causes them to experience a lower velocity. The next row is then again in the wake area of the added elements, which causes also these elements to experience a lower velocity. Also the vortex shedding mentioned for the staggered configuration might play a role. A sketch of the mechanisms is depicted in Figure 5.3.



(a) Total dissipation for the horizontal half width.

(b) Dissipation per element for the horizontal half width.

Figure 5.4: Total dissipation for the vertical configurations. Each configuration and wave condition is tested twice, which gives only a slight difference for some wave conditions. Larger KC represents longer waves.

For the horizontal orientation, the same trends are observed, except for the effectiveness of the uniform open configuration. In this case, both the spacing in horizontal and vertical direction are important. As the uniform open configuration has the largest spacing in both directions, this one is per element the most effective. The effects are largest for wave periods around  $T = 1.0s$ . Differences with the longitudinal configuration are however small.

### 5.3. Effect of diameter

By plotting the simplified dimensionless drag coefficient based on formula 4.1 against the  $KC^*$  number based on element spacing ( $KC^*$ ), a comparison is made with previous research of Haage (2018) on a 2cm model. The drag coefficient is the average value per element, by assuming a linear decay in wave height trough the structure.

#### Primary effect

The values of  $KC^*$  for the two diameters partly overlap, which makes it possible to make a direct comparison between the drag coefficients for both diameters. By analyzing the total data set, it is observed that the drag coefficient follows the same trend: an increase for  $KC^*$  values below 4. The trend is much stronger for the horizontal orientation compared to the vertical orientation. This is expected, as the calculation of the drag coefficient does not account for the vertical velocity component in case of the horizontal elements, which is strongest for the low  $KC^*$  numbers.

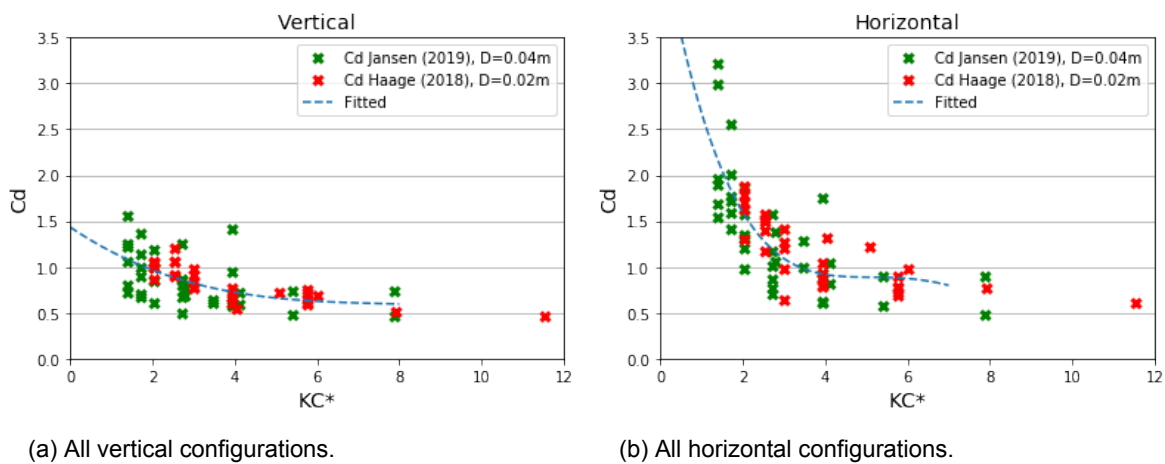


Figure 5.5: Comparison of the simplified drag coefficient plotted against the  $KC^*$  number, which is based on the heart-to-heart spacing of the element in the direction of wave motion.  $KC^*$  indicates how many elements the water particle encounters on its path.

The  $KC^*$  value is calculated based on the depth-averaged value of the maximum velocity amplitude, which means that for most of the wave period the value is actually lower. This suggests that the drag coefficient strongly increases if the excursion reaches only 1 or 2 elements. For the larger  $KC^*$  values, which means larger velocities, the flow between the elements might become more streamlined, resulting in a sheltering effect and a decrease in drag coefficient, as sketched in Figure 5.6. Based on the expected wave conditions in the field, an ideal heart-to-heart distance can be designed, resulting in an optimization of the drag coefficients.

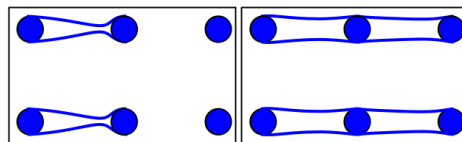


Figure 5.6: A sketch of the sheltering effect that might play a role for a larger excursion.

However, the described trend is valid for both diameters and no distinction can be made based on a direct comparison of the obtained drag coefficients per configuration, concluding that the diameter has no significant direct influence on  $C_d$ .

### Secondary effect

However, despite the fact that the diameter does not have a direct effect on the drag coefficient, there might be a secondary effect. For both diameters, the tested wave conditions and with that the excursions are the same. As in this research the diameter is larger, the water particles will encounter less elements for the same excursion. This results in a lower  $KC^*$  value, but a larger drag coefficient following from the observed trend. The increase in drag coefficient is only observed for low  $KC^*$  values, which makes increasing the diameter only interesting if the values are already close to this regime.

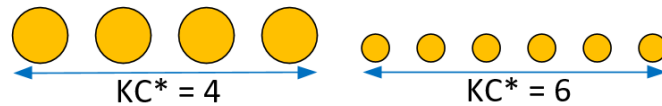


Figure 5.7: A sketch of the influence of the diameter on  $KC^*$ . For the same excursion, the  $KC^*$  value is lower for a larger diameter.

For the current studies, this effect is only marginal as the configurations had the same spacing of  $2\text{cm}$ . If the spacing was also scaled (which would then be  $4\text{cm}$ ), the differences would be more significant.

## 5.4. Executive summary

This section summarizes the most important points and observations of the analysis of the first set of experiments.

- An increase in structure width causes an increase in dissipation, but the relation is non-linear.
- The horizontal structures dissipate more energy than the vertical structures. The effect is strongest for wave periods around  $T = 1.0\text{s}$  and decreases with increasing wave period.
- Adding more elements to the structure causes an increase in dissipation, but considering the dissipation per element it is only effective for the longitudinal configuration.
- With respect to the wave period, an increase in wave period causes in general a decrease in wave energy dissipation.
- By comparing the drag coefficient for the 2 centimeter and 4 centimeter model, no direct effect of the increase in diameter is observed.

### Remark

With the results and conclusions presented in this chapter, it is possible to make a prediction of the energy dissipation for these specific configurations. However, the structure itself is still treated as a black box and the processes that cause the (difference in) energy dissipation are not fully understood. To gain more insight into what happens inside the structure, more detailed measurements are performed, which will be explained in Chapter 6.



# 6

## Methodology: Second set of experiments

The second set of experiments focuses on what happens inside the structure. Section 6.1 gives a description of the setup and location of the measurement instruments in the different configurations. This is followed in Section 6.2 by the wave conditions to which the model is subjected. Section 6.3 explains how the gathered data is processed and how the force coefficients are obtained. To study what happens inside the model, two methods are adopted, which are explained in Section 6.4.

### 6.1. Set-up

#### 6.1.1. Data gathering

To make a comparison with the first set of experiments on dissipation, the four wave gauges as described in Section 3.3 are also installed in the second set. In addition, an Electromagnetic Flow meter (EMF) is located in front of the model (at a distance of 6.10m), to measure the undisturbed velocity and make a comparison with the velocity of linear wave theory.

To determine the drag and inertia coefficients by means of direct force measurements, a force transducer (FT) and an Acoustic Doppler Velocimetry sensor (ADV) are applied inside the model. Details on their framework and the accuracy of the instruments are presented in Appendix B. Their exact locations in the horizontal plane are discussed in Section 6.1.2. As the velocity under waves changes over depth (as discussed in Section 2.2), velocity measurements are performed at three different heights ( $z = 0.15, 0.25$  and  $0.40m$ ), which is depicted in Figure 6.1. Based on these three measurement points, a velocity profile is reconstructed, which will be discussed in Section 6.3.2. For every test, the EMF in front of the model is located at the same height as the ADV.

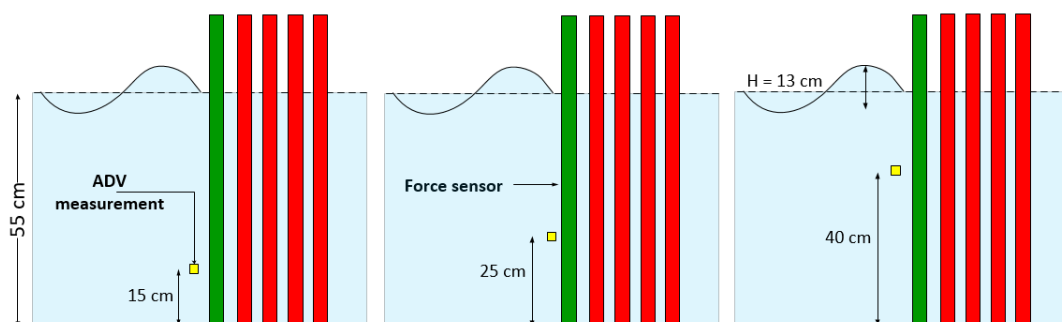


Figure 6.1: Schematic side view of the distribution of the ADV measurements over height. Each wave condition is repeated three times, changing the height of the ADV for every test to estimate a velocity profile over depth.

### 6.1.2. Model configurations

From the analysis of the first results, it becomes clear that the velocity is an important factor in the determination of the force coefficients. In the second set, the velocity is measured at different locations inside the model. To capture the change from undisturbed flow (empty flume) to the flow inside an array of elements, the number of elements in the model is gradually increased from a single element to a full array of elements (see Figure 6.2). To see the development of the force and velocity through the structure, the measurements are also performed on the first and the last row of the structure.

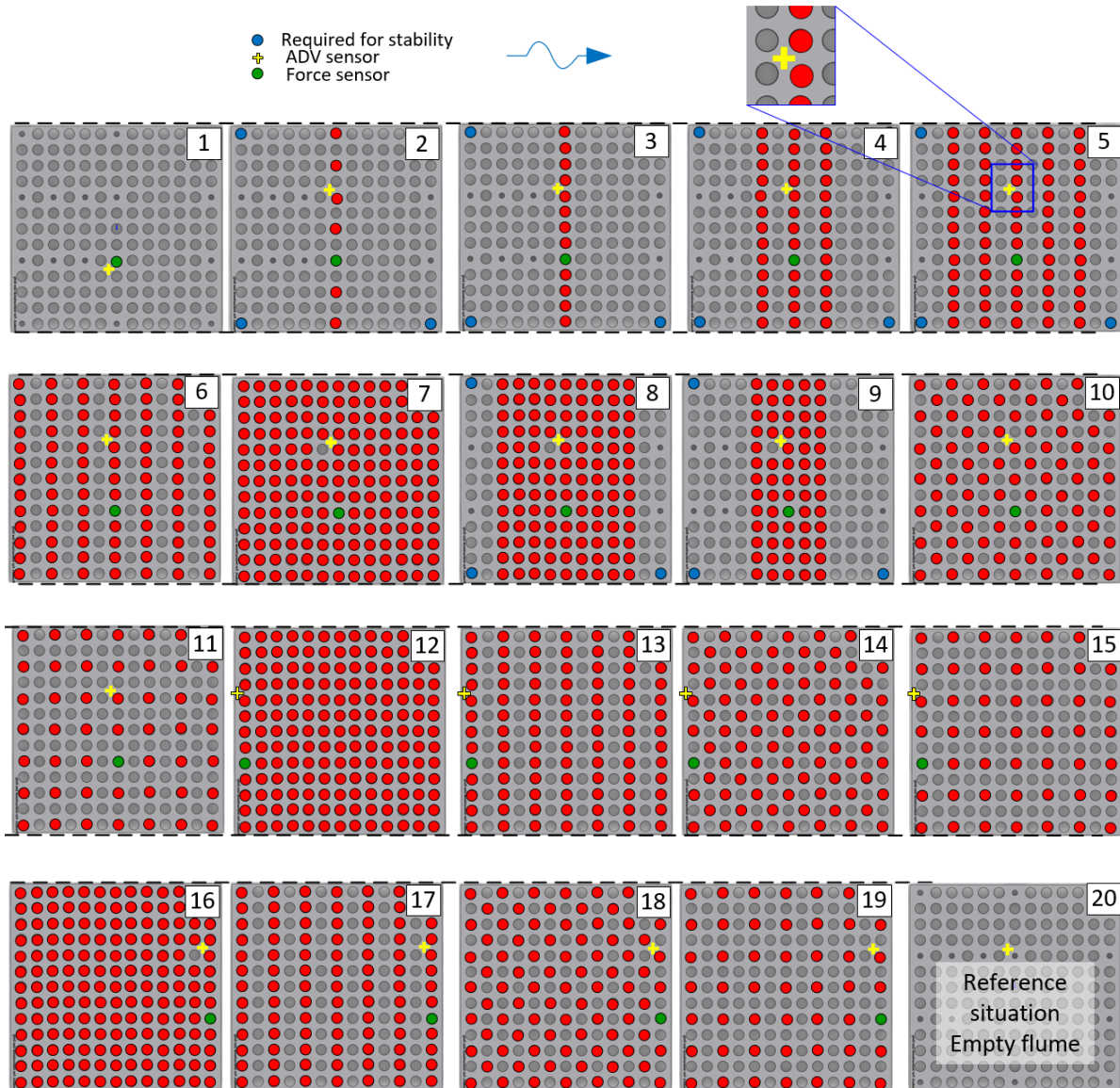


Figure 6.2: Top view of the vertical test configurations with the location of the force sensor and ADV. Waves are incoming from the left. For the uniform dense configuration, an element is missing to make space for the frame of the ADV.

Due to time limitations, the row-by-row testing is done for only 2 configurations: the longitudinal and uniform dense configurations as these are the most interesting from dissipation perspective as discussed in Section 5.2. For the staggered and uniform open configuration, only the complete structures are tested on the front, middle and last row.

## 6.2. Wave conditions

In the first set of experiments, the focus was on short waves to remain within the assumptions of linear wave theory and make a comparison with previous research. In the second set, these waves are tested again, as for these cases the behaviour of the force coefficients is easiest to understand. To make also a connection with the real wave conditions of Indonesia (see Section 2.4) in the data set, it was expanded with longer wave periods ( $T = 3.00s$ ,  $T = 4.00s$  and  $T = 5.00s$ ). However, for these wave conditions the reflection from the back of the flume was too large which complicated the interpretation of the results, due to interaction of the incoming and reflected wave. The total set of tested wave conditions with some characteristics is presented in Table 6.1. Figure 6.3 presents the change in the shape of the waves from a 1 to 3 seconds wave period. The water level is lowered to 55cm to prevent the waves from hitting the frame of the force transducer.

Table 6.1: Tested wave conditions with their characteristic values.

Name	H [m]	T [s]	d [m]	Re	KC	KC*	H/L
T100	0.13	1.00	0.55	6665	4.2	1.39 / 2.78	0.08
T125	0.13	1.25	0.55	7868	6.1	2.05 / 4.10	0.06
T150	0.13	1.50	0.55	8638	8.1	2.70 / 5.40	0.04
T175 <sup>1</sup>	0.13	1.75	0.55	9128	10.0	3.33 / 6.66	0.04
T200	0.13	2.00	0.55	9451	11.8	3.94 / 7.88	0.03
T300 <sup>2</sup>	0.13	3.00	0.55	11880	22.28	7.43 / 14.85	0.02

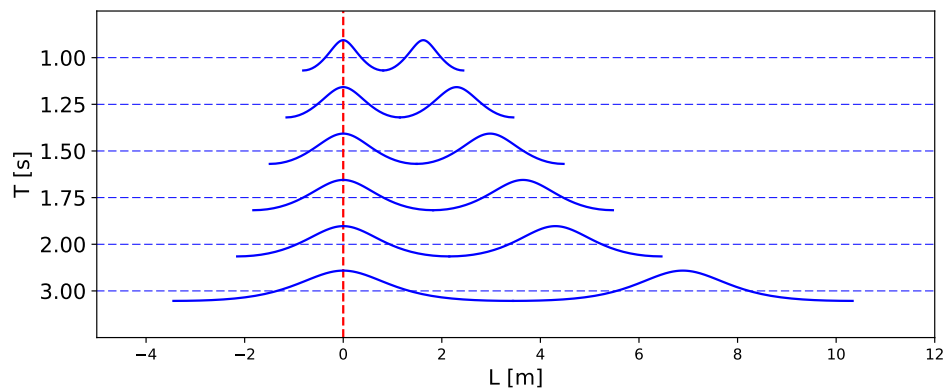


Figure 6.3: Change in wave shape for increasing period. The short waves remain within the assumption of linear waves, while the 3 second wave represent a cnoidal wave.

## 6.3. Data processing

The goal of this research is to understand what happens inside the structure. Part of this is the understanding of the different components in the formulae for the force signal:

$$\frac{1}{2}\rho C_d b u |u| + \frac{1}{4}\rho \pi C_m b^2 \dot{u} = F_m \quad (6.1)$$

The first step in the analyses is to obtain the relevant velocity and acceleration signals. Based on these signals, the coefficients can be determined using the Least square method. This section gives a description on how the input values and coefficients are obtained.

<sup>1</sup>The  $T = 1.75s$  wave had a strange behaviour in the flume. For the empty flume, there was a large difference in velocity measured by the EMF and ADV, where they were expected to be the same. The wave case also showed a exceptional large reflection from the model in comparison with the other wave cases.

<sup>2</sup>For this wave, the wave absorber at the end of the flume was not able to dissipate all the energy, resulting in a large reflection component from the back of the flume which interferes with the incoming wave. Therefore it is decided to leave this wave out of the analyses.

### 6.3.1. Filtering of the measured signals

#### Velocity

The measured velocity signal shows small fluctuations, caused by the local turbulence around the element. However, the forces are considered depth-averaged (the total force on an element), ignoring the small fluctuations over depth. Also, the depth-average velocity signal used for the fitting of the force coefficients is derived from velocity measurements in separate experiments. It is therefore decided to filter out the very high-frequency fluctuations in the velocity signal in two steps with a moving-average over 20 points (with a measurement frequency of 100Hz), in order to make correlations and calculations easier. An example of a filtered velocity signal is shown in Figure 6.5a. The filter removes the local peaks, which might result in a slight underestimation of the local peak velocities.

#### Force

If the frequencies of the loading force are in the same order of the natural frequency of the system, it might start vibrating in this frequency. To exclude these effects in the measured force signal, first the natural frequency of the system is determined. This is done by placing the model in the flume filled with water and giving a force pulse. The frequency in which the force damps out is the natural frequency, which is determined using Continuous Wavelet Transform (CWT). The results are shown in Figure 6.4, resulting in a natural frequency between 6-7Hz.

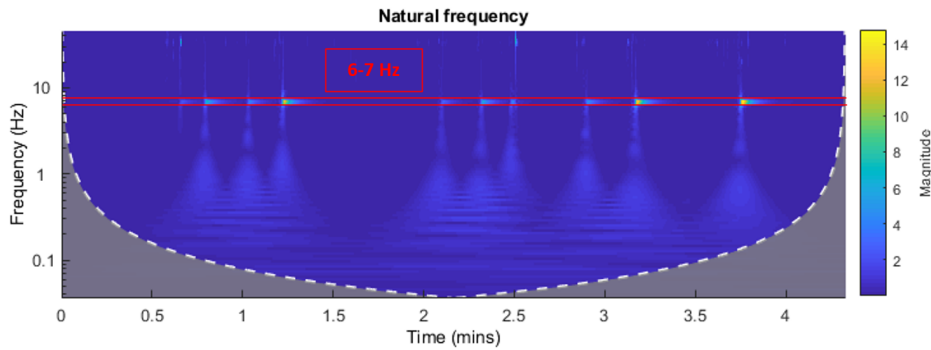
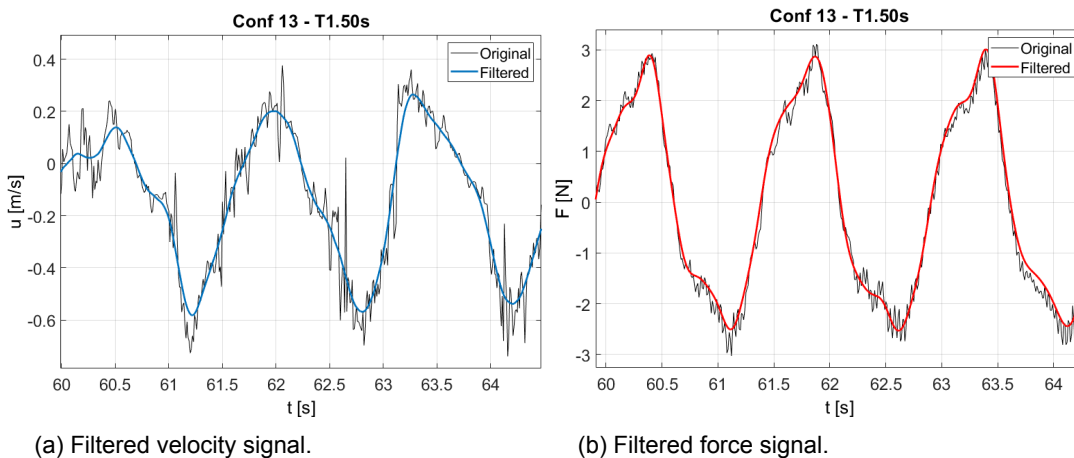


Figure 6.4: CWT diagram to determine the natural frequency of the system when it is placed in water.

The measured force signal is then filtered for a specified frequency band which is lower than the natural frequency (0-5Hz.). This preserves the frequencies of higher wave harmonics, but removes the high natural frequency. An example of the filtered force signal is shown in Figure 6.5b.



(a) Filtered velocity signal.

(b) Filtered force signal.

Figure 6.5: Example of the filtered signals for configuration 13 with a  $T = 1.5s$  wave.

### 6.3.2. Computation of the velocity profile over depth

The velocity measurements over height are done in three different experiments, which causes a time shift in the signals (see Figure 6.6a). To construct a velocity profile over depth, the results of the 3 experiments are combined. In order to make sure that the measured velocity in each experiment corresponds to the same phase of the wave, the correlation between the surface elevation at wave gauge 1 of each test is calculated, according to:

$$R(\eta_f(t), \eta_i(t + \Delta t_s)) = \frac{\eta_f(t) * \eta_i(t + \Delta t_s)}{\sqrt{\eta_f(t)^2 * \eta_i(t + \Delta t_s)^2}} \quad (6.2)$$

in which  $\eta_f$  is the water surface elevation of the experiment from which the measured force signal is used.  $\eta_i$  represents the surface elevation of an experiment with the same wave condition, but a different ADV height. The required time shift,  $\Delta t_s$ , is calculated by maximizing the correlation coefficient. Figure 6.6a shows the unprocessed velocity signal. After applying the time shift, the resulting velocity signal is similar to Figure 6.6b.

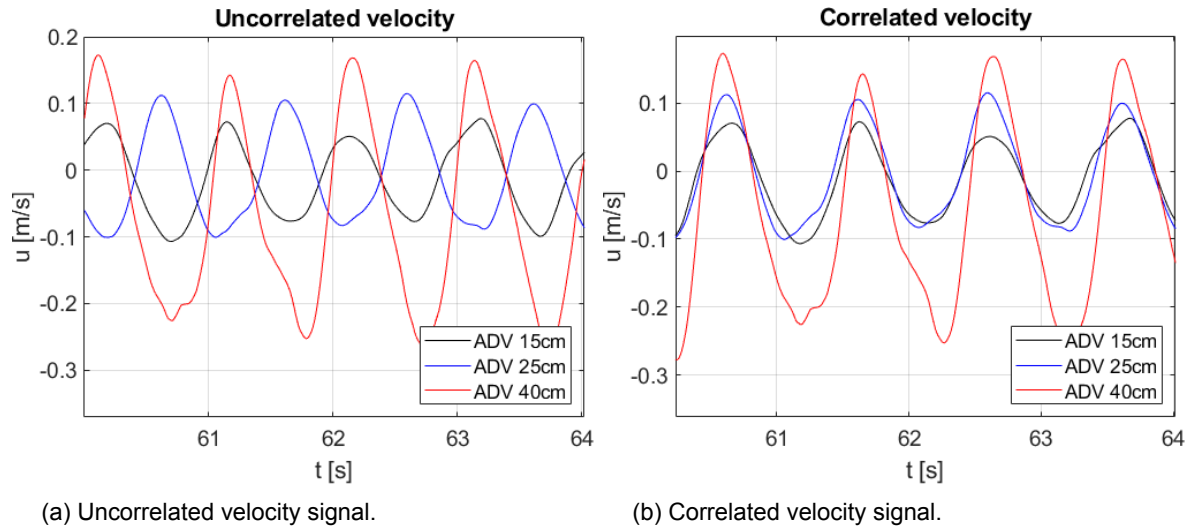


Figure 6.6: Example of the time shift in the velocity signals for  $T = 1.00s$ .

The measured velocities result in a velocity profile of only three points. To construct a velocity profile over the full depth, the velocity profile under linear wave theory is fitted to the measurements. The correction factor that is used is defined as:

$$factor = \frac{\sum(\frac{u_m}{u_l})}{N_m} \quad (6.3)$$

in which  $u_m$  is the measured velocity,  $u_l$  the velocity under linear wave theory at the same water depth and  $N_m$  the number of measurement points over depth (3 in this research). Based on this corrected velocity profile, the depth averaged velocity is computed by integrating the velocity profile at each moment in time. The resulting velocity is similar to Figure 6.7b. The depth-averaged velocity is then used to calculate the acceleration and the force coefficients.

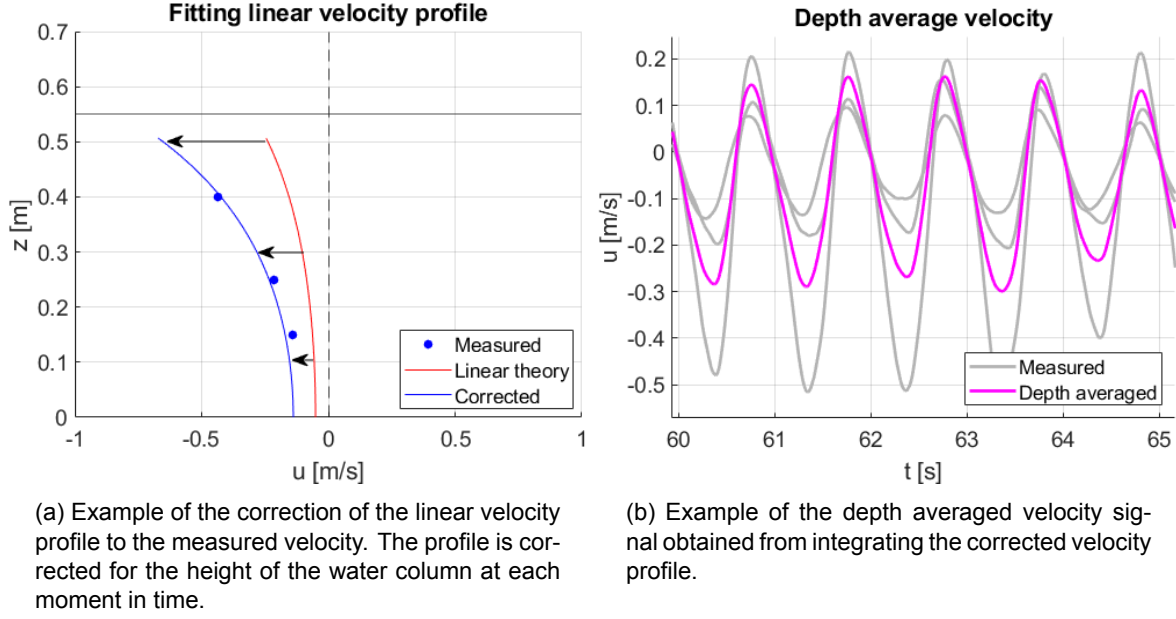


Figure 6.7: Computation of the depth averaged velocity, used for the reconstruction of the force signal. The linear profile is fitted through the measured data in (a), for which then the depth-average velocity is calculated (b).

### 6.3.3. Computation of the force coefficients

To calculate the force coefficients, the least square method described by Hudspeth et al. (1988) is used. Later, Isaacson et al. (1991) compared this method to different approaches based on their relative accuracy, and concluded that this was the most simple and accurate method of the approaches he examined. The method is based on the estimation of one constant pair of force coefficients for a time series, by minimizing the squared error between the predicted and measured force (Borgman, 1972). The sum of the squared error over a time series is given by:

$$\varepsilon^2 = \sum [F_p(t) - F_m(t)]^2 \quad (6.4)$$

In this equation, the predicted force can be described and simplified as:

$$F_p = \frac{1}{2} \rho C_d b u |u| + \frac{1}{4} \rho \pi b^2 \dot{u} \rightarrow K_d u |u| + K_i \dot{u} \quad (6.5)$$

With:

$$K_d = \frac{1}{2} \rho C_d b \text{ and } K_i = \frac{1}{4} \rho \pi b^2$$

Assuming that the derivative of the error squared to each of the force coefficients is equal to zero, results in two equations:

$$\frac{\delta \varepsilon^2}{\delta K_d} = 0 \rightarrow K_d \sum (u^2 |u|^2) + K_i \sum (u |u| \dot{u}) = F_m \sum (u |u|) \quad (6.6)$$

$$\frac{\delta \varepsilon^2}{\delta K_i} = 0 \rightarrow K_d \sum (u |u| \dot{u}) + K_i \sum (\dot{u}^2) = F_m \sum (\dot{u}) \quad (6.7)$$

Solving these equations, using the earlier obtained velocity and acceleration signals, results in a combination of  $K_d$  and  $K_i$  for which the predicted force approaches the measured force best. The drag and inertia coefficient are obtained by dividing the force coefficients by their constants of equation 6.5.

### 6.3.4. Asymmetry in velocity signal

Due to the size of the ADV, it is not possible to position it between the elements of a row. Instead, the ADV is positioned in front of the rows, as shown in Figure 6.2. However, as a consequence of this location, the measured velocity signal shows asymmetry. The measured negative velocities are larger than the positive velocities, especially when the elements of a row are close together. For the positive part of the wave cycle, measured velocities are more or less undisturbed. For the negative part of the cycle, the ADV measures the jet generated by the flow between the elements. The process is visualized in Figure 6.8. Due to this asymmetry, it is decided to focus on the negative quantities, as it is assumed that the jet is also present in positive direction but not measured.

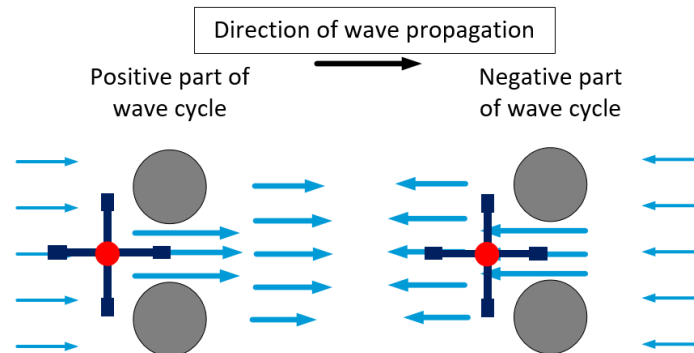


Figure 6.8: Location of the ADV. On the left, it shows the positive part of the wave cycle when the ADV measures the undisturbed velocities, before acceleration between the elements. The right side shows the negative part of the cycle, when the ADV measures the jet generated by the flow between the elements. The red circle marks the location of the velocity measurement.

## 6.4. Approach with 2 methods

Due to the asymmetry in the measured velocity signal, calculating the force coefficients based on this signal will result in unrealistic values. Therefore, two methods based on the theory of linear velocity are adopted. Method 1 takes the measured energy dissipation (calculated with the wave gauge signals) as a starting point and assumes a constant pair of force coefficients. An amplification factor for the velocity ( $UF$ ) is then calibrated to match the measured dissipation. Method 2 takes the measured force signal as a starting point and assumes that linear wave theory is valid within the model. The force coefficients are then calibrated to match the measured force. For both methods, the linear velocity inside the model is corrected for the decrease in wave height due to energy dissipation, as explained in more detail in Appendix F.

To check the reliability of both methods, the calibrated parameters of each method are then used to perform a cross-check on the energy dissipation and force. The workflow for the two methods is shown in Figure 6.9. A more elaborate explanation of the steps is given in Appendix F.

The approach is adapted from Chen et al. (2018), who made a similar comparison between the calibration method and the direct force measurement method.

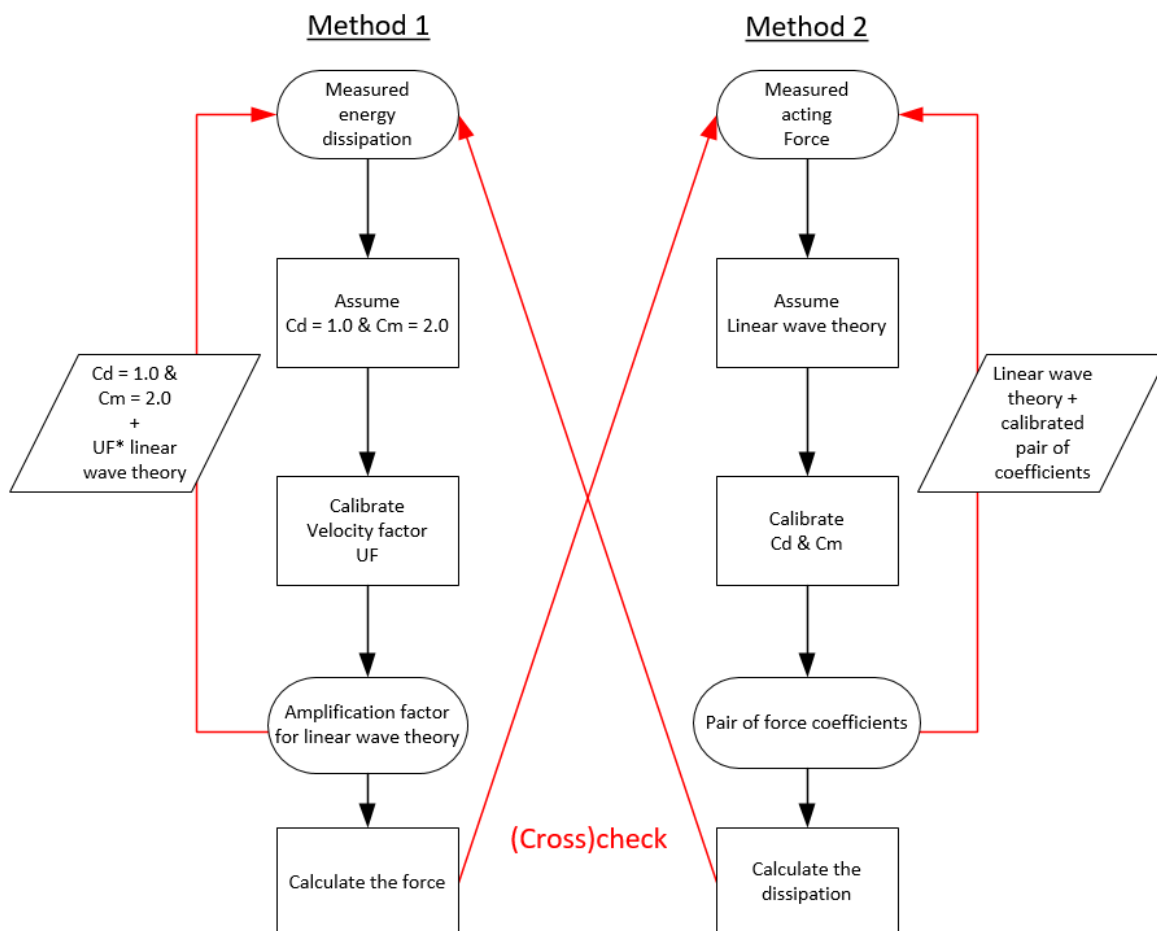


Figure 6.9: Workflow for the two-method approach. The calibrated parameters are checked with their direct-linked measured quantities and cross-checked with the indirect-linked measured quantity. Figure adapted from Chen et al. (2018).

## Results: Second set of experiments

*This chapter presents the results of the second set of experiments. Due to time limitations, only the longitudinal and uniform dense configuration are considered, as these are the most interesting from the dissipation perspective. It starts in Section 7.2 with the results for the dissipation, velocity and force when increasing the width of the structure. Thereafter, the effect of the location in the model is considered for the force and velocity in Section 7.3. The Chapter concludes in Sections 7.4 & 7.5 with presenting the results of the two methods explained in previous chapter. Due to the asymmetric velocity signal mentioned in Section 6.3.4, only the relevant negative quantities are shown in the results.*

### 7.1. Presentation of the results

For the presentation and comparison of the velocities, the mean amplitude of the depth-average velocity is used. The depth-average velocity is calculated as described in Section 6.3.2. For the interval of 40-70 seconds in the measurement series, the maximum amplitudes are then determined. The presented values are the averages over this interval. Figure 7.1 gives an example of the measured velocities, the depth average velocity and the location of the maximum amplitude.

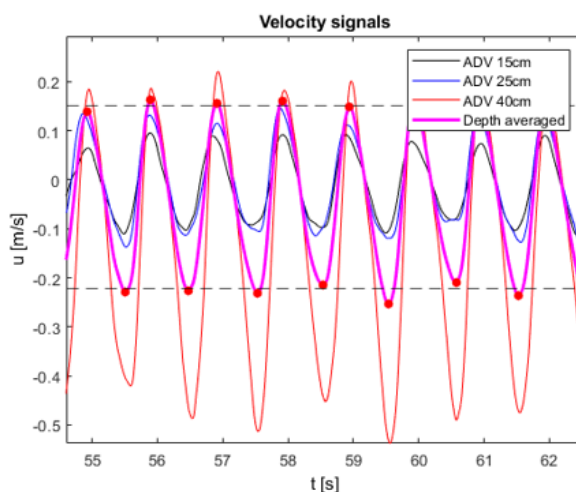


Figure 7.1: Example for the calculation of the average value of the maximum amplitude.

The same method is applied on the force signal, by determining the maximum amplitude of the measured force signal for the same interval. The presented values are the averages of this interval.

## 7.2. Effects of increasing the number of rows

To understand the behaviour of the complete model, it is important to understand how the processes and quantities change from an empty flume to the full structure. Therefore, this section focuses on the build up of the longitudinal and uniform dense configuration in 4 steps, as shown in Figure 7.2. The structure width in the intermediate steps is the same for both configurations, but the number of rows and elements is different.

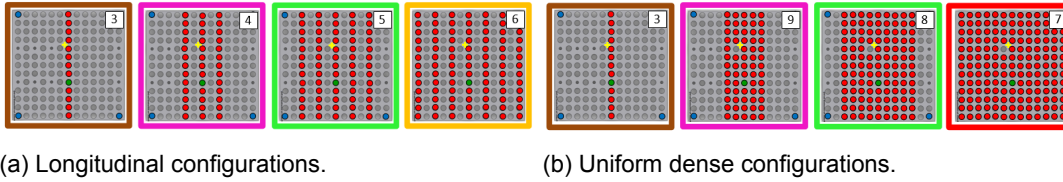


Figure 7.2: Increasing the structure width for the longitudinal and uniform dense configuration. Both configurations have the same width, but a different number of rows/ elements. Colours are used for comparisons in Section 7.2.2 and 7.2.3

### 7.2.1. Dissipation

For each width, the energy dissipation is calculated from the energy balance as described in Section 3.4.1. The results are shown in Figure 7.3, presented as a percentage in the incoming wave energy. As expected, the amount of energy dissipation increases with increasing width. For the first half of the structure (0-0.4m), a strong increase is observed, which flattens when the width increases further. This behaviour was also observed in Section 5.2.1 and in the research of (Haage, 2018), with most of the energy dissipation taking place in the first half of the structure. Although the uniform dense configuration has more rows/ elements for the same width, the observed trend and amount of dissipation is of the same order for both configurations. Also over the different wave cases the trend is the same, with only a difference in the amount of dissipation.

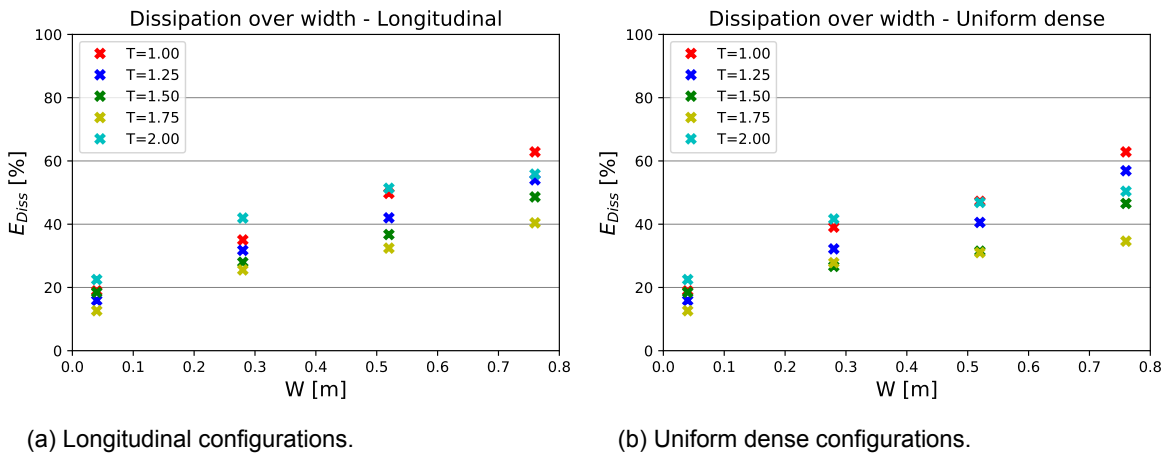


Figure 7.3: The amount of energy dissipation for an increasing structure width for the longitudinal and uniform dense configuration.

### 7.2.2. Velocity

As energy dissipation is driven by the velocity, it is important to understand how this behaves and relates to the undisturbed velocity/ linear wave theory. Figure 7.4 shows the negative velocity for increasing width, with also the results of the undisturbed velocity (no model in the flume) and linear wave theory. The left side shows the longitudinal configuration, the right side the uniform dense. A strong increase in velocity is observed when changing from an empty flume to a single row, with velocities going from 0.3m/s up to 0.8m/s. The difference

is small for the shortest wave ( $KC = 4.5$ ) and increases with increasing  $KC$  number. For both configurations, a dip in the velocity is observed for  $KC = 10.5$  ( $T = 1.75s$ ).

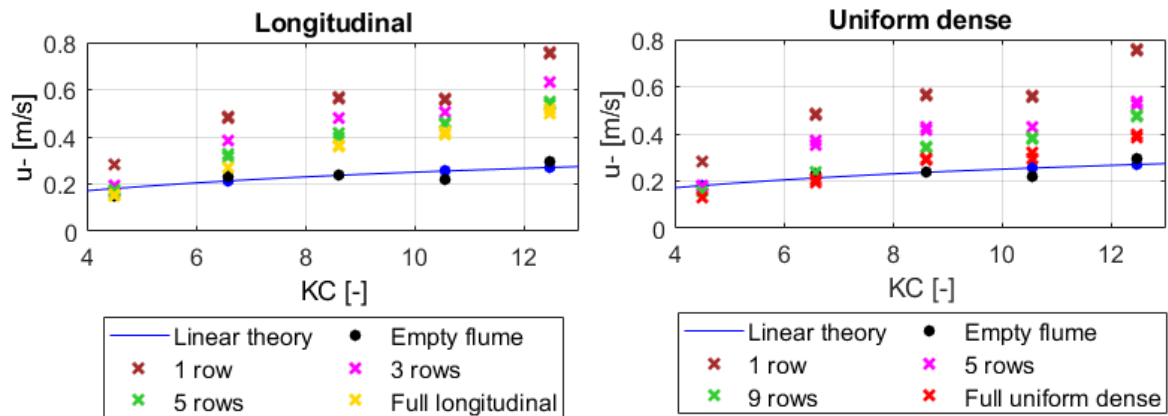


Figure 7.4: Results of the amplitude of the negative depth-averaged velocity for increasing structure width.

When increasing the structure width from 4 (x) to 28cm (x), the velocity decreases. This decrease is larger for the uniform dense configuration, although the amount of dissipation is the same (Figure 7.3). With a further increase of the structure width, the velocity gradually decreases further. However, for the full structure width, the velocity in the middle of the structure is still equal to or larger than the undisturbed velocity and linear wave theory, despite the wave height reduction in front of the measurement location.

### 7.2.3. Force

Also for the force, the strong increase is observed when changing from a single element to a full row, with forces ranging from 1.0 to 4.0N (see Figure 7.5). The force then gradually decreases when more rows are added in front of the measurement location. Again, the decrease is stronger for the uniform dense configuration. Although the velocity increases with increasing  $KC$ , the force has a more constant value, except for  $KC = 12.5$  where a strong increase is observed.

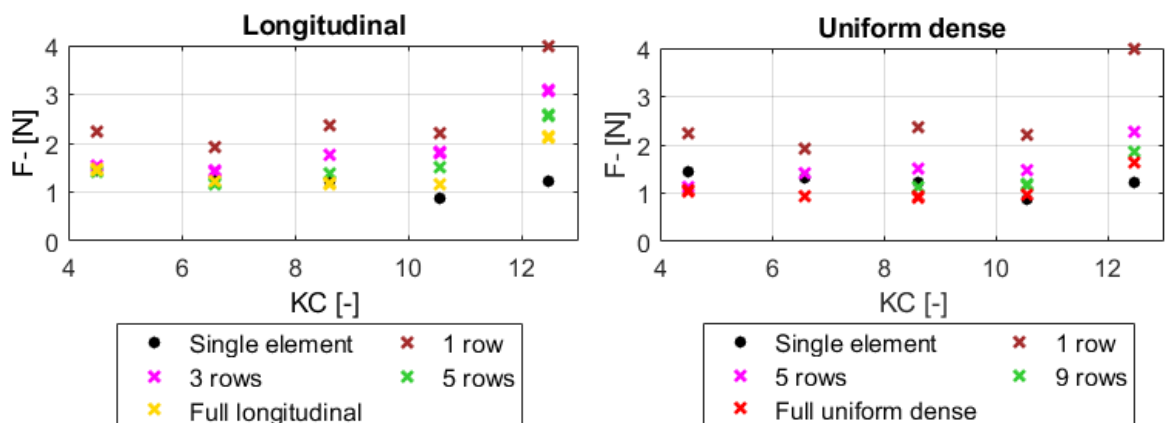


Figure 7.5: Results of the amplitude of the negative force for increasing structure width.

As the decrease is stronger for uniform dense configuration, the forces for the full configuration are slightly smaller than for the longitudinal one. For  $KC = 4.5$ , forces even drop below the values for a single element.

### 7.3. Effect of location in the model

The second part in understanding the behaviour of the complete structure, is looking at the effect of the location in the model on the measured quantities. For the two configurations, the results of 3 locations are presented; the front, middle and back row, as shown in Figure 7.6.

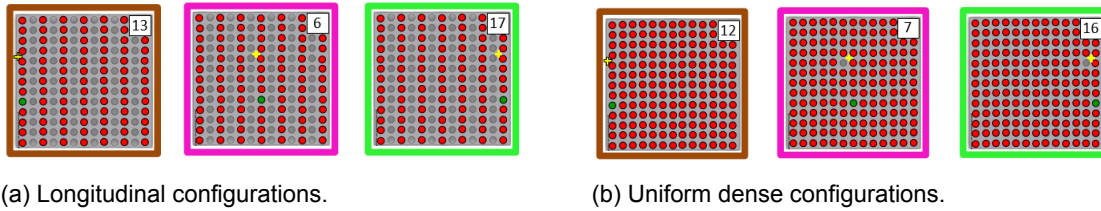


Figure 7.6: Different measurement locations in the model; front, middle and back row. Waves are incoming from the left. The colours are used in the comparison.

#### 7.3.1. Velocity

Figure 7.7 presents the results of the velocity at the different locations. The left side shows the longitudinal configuration, the right side the uniform dense configuration. For the longitudinal configuration, the velocities show a large variation over  $KC$ . The velocities are the largest at the front row, with values up to  $0.6m/s$ . However, for the middle and back row, values vary between the undisturbed velocity and the velocity at the front row, without a clear trend. For  $KC < 10$  the velocities of both rows are approximately the same, for  $KC = 10.5$  the velocity at the last row is larger and for  $KC = 12.5$  the velocity at the middle row is larger.

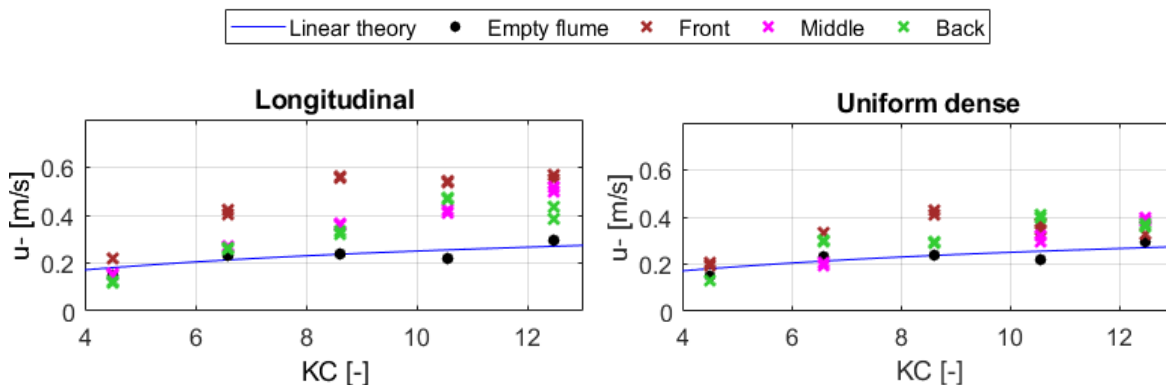


Figure 7.7: Negative velocities for different locations in the model.

For the uniform dense configuration, the spread in velocities is smaller, with values between  $0.2$  and  $0.4m/s$ . For low  $KC$ -numbers, the velocity at the front row is largest, where for the larger  $KC$ -numbers the distinction is less clear. For all wave cases and locations, the measured velocities are approximately equal to or larger than the undisturbed velocities.

#### 7.3.2. Force

For the forces, more or less the same trend is observed (see Figure 7.8). Largest forces are measured at the front row ( $2.0-2.5N$ ) and the forces at the middle and back row vary between the values of the single element and the front row ( $1.0-2.5N$ ). Also, the values for the middle and back row are approximately the same for  $KC < 10$  (with only a small difference for  $KC = 6.5$ ), for  $KC = 10.5$  the force on the back row is larger and for  $KC = 12.5$  the force on the middle row is larger. However, the forces per row are more constant over  $KC$  than the velocities.

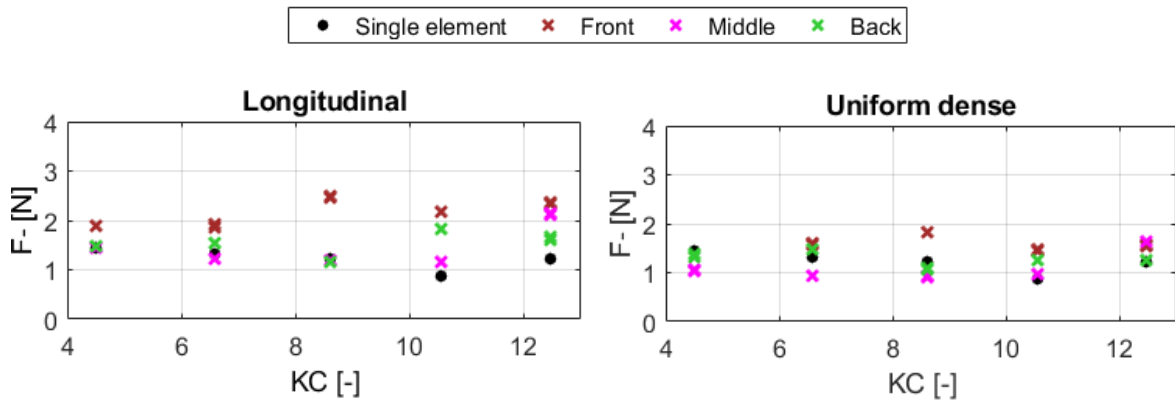


Figure 7.8: Negative forces for different locations in the model.

For the uniform configuration, the order in the forces is more clear. The largest forces are measure at the front row, with values between 1.5 and 2.0N. These are followed by the forces of the last row, with values between 1.0 and 1.5N. The lowest forces are measured in the middle of the structure, with a more or less constant value of 1.0N. Only exception is  $KC = 12.5$ , where forces of the middle row are equal to the forces of the front row (1.7N). The low values for the middle row might suggest sheltering of the elements, which reduces the forces.

## 7.4. Results method 1 - Calibration from dissipation

Figure 7.9 shows the results of the calibrated amplification factor to be applied on the velocity of linear theory to predict the dissipated energy. The figure shows that the trend is the same for both configurations, with a more or less constant value for  $KC < 11$  and an increase for  $KC = 12.5$  (the  $T = 2.0s$  wave). The amplification factor for the longitudinal configuration is larger than the factor for the uniform configuration, with values of respectively 1.4-1.7 and 1.1-1.4.

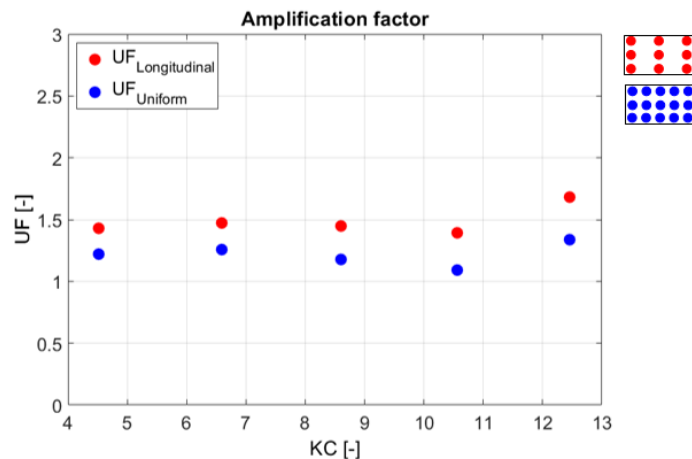


Figure 7.9: Amplification factor ( $UF$ ) for the linear velocity, calibrated for the energy dissipation.

## 7.5. Results method 2 - Calibration from forces

In method 2, the force coefficients  $C_d$  and  $C_m$  are determined based on a semi direct-force calculation, with a measured force signal and a velocity profile of linear theory. The velocity profile for the middle and back row is adapted for the wave height inside the structure using the transmitted wave height from the experiments with increasing width (see Section 7.2). For more details on the calculation, see Appendix F. The results are presented in Figure 7.10 (Longitudinal) and 7.11 (Uniform).

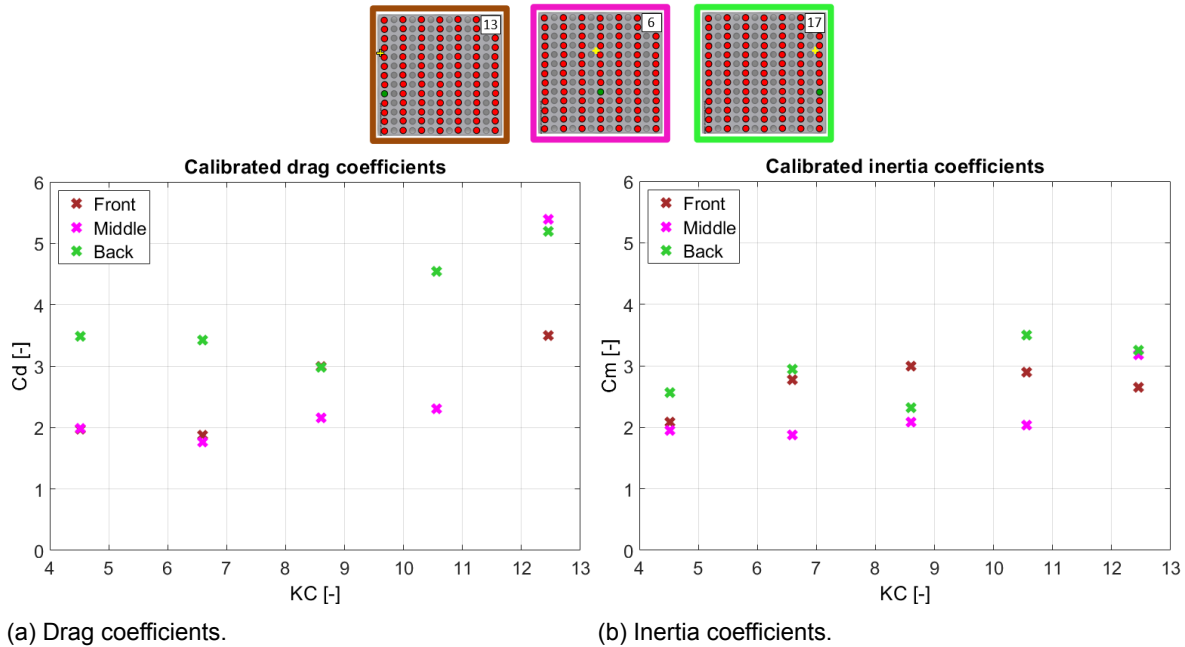


Figure 7.10: Force coefficients determined for 3 locations in the longitudinal configuration; front (13), middle (6) and back (17).

The calibrated drag coefficients for the longitudinal configuration show a large spread, with values ranging from 1.9 to 5.5. The front and middle row have values around 2.0 for the low  $KC$ -numbers (with a deviation at  $KC = 8.5$ , where the front row has a value of 3.0) and show an increase for  $KC = 12.5$ . For the back row, the coefficients are significantly larger in general, with values between 3.0 and 5.5.

For the inertia coefficients the spread is smaller, with values between 2.0 and 3.5. Still, the largest values are for back row (2.3-2.5), followed by the front (2.0-3.0) row and the middle row (1.9-3.2). The inertia coefficients are more constant over  $KC$  in comparison with drag coefficients.

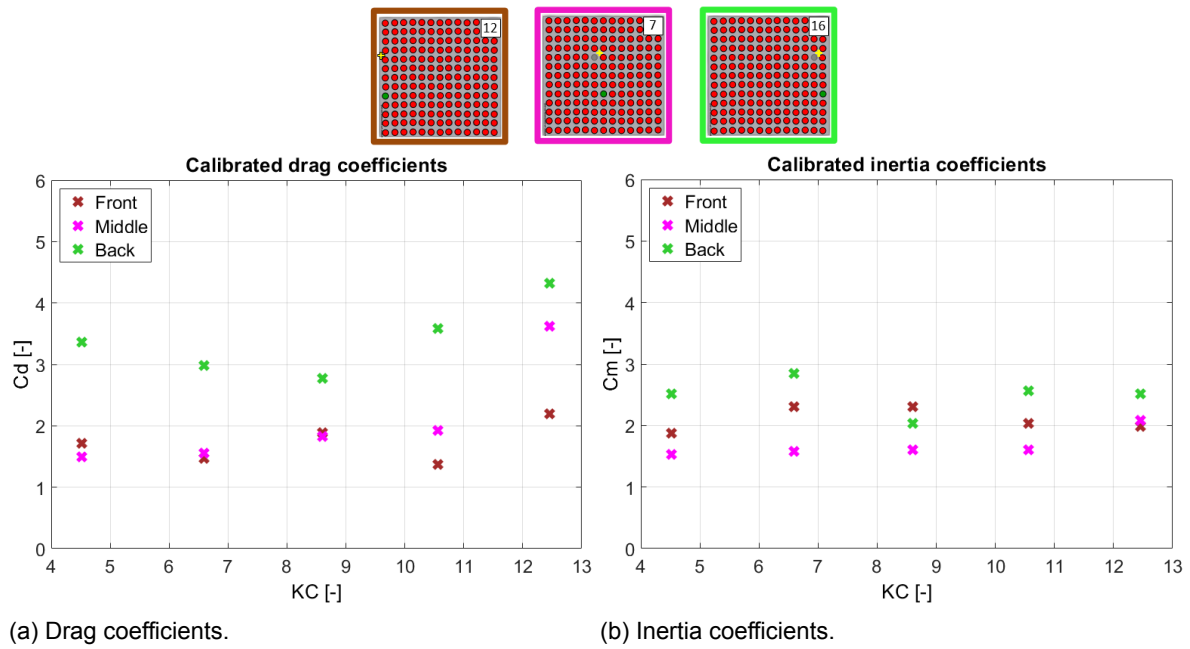
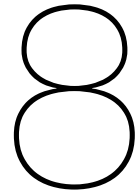


Figure 7.11: Force coefficients determined for 3 locations in the uniform configuration; front (12), middle (7) and back (16).

For the uniform dense configuration, drag coefficients vary between 1.5 and 2.0 for the front and middle row, except for  $KC = 12.5$  where an increase is observed. For the back row, drag coefficients are significantly larger, with values between 2.5 and 4.5. Here, also an increase is observed for increasing  $KC$ . The calibrated inertia coefficients show a more constant trend over  $KC$ , with values between 1.5 and 3 for all three locations. The largest values are for the back row (2.0-3.0), follow by the front row (1.9-2.5) and the middle row (1.5-2.1).

The implications and reliability of these results are further analyzed in Chapter 8.





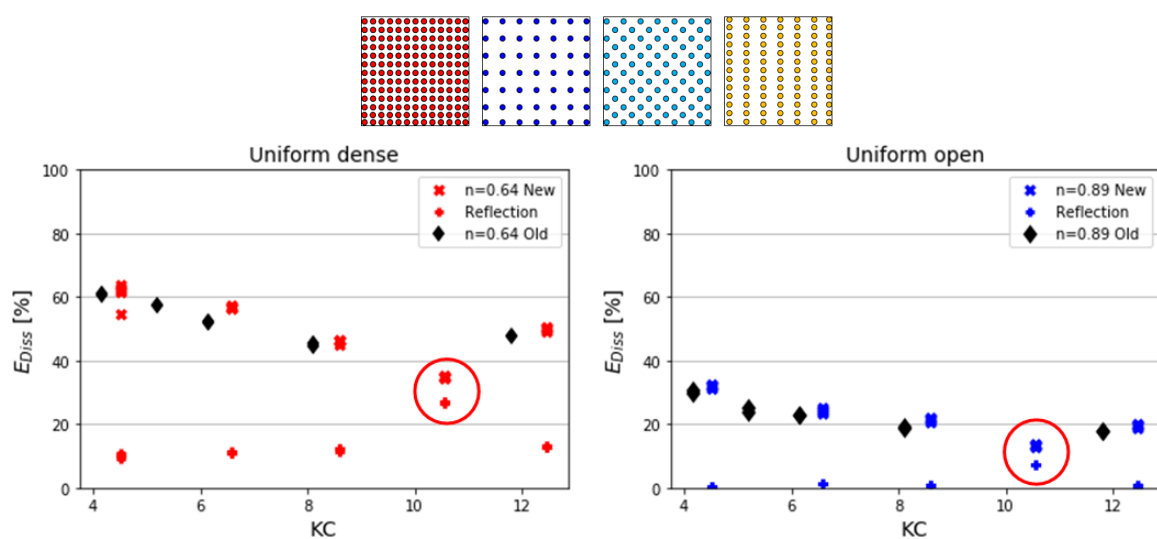
## Analysis of the results: Second set

In this chapter, the results of the second set of experiments are analyzed. First, the energy dissipation and transmission is analyzed for the complete structures in Section 8.1, including a comparison with the first set of experiments and the theory of Dalrymple. In Section 8.2, the forces and velocities are analyzed by calculation of the amplification factors, which are compared with factors for constricted velocity. The two methods of Section 6.4 are then analyzed in Section 8.4 and 8.5, followed by their comparison in Section 8.6. Section 8.7 elaborates a bit more on method 1. The chapter concludes in Section 8.8 with a short summary of the most important points and observations.

### 8.1. Dissipation and transmission

Figure 8.1 shows the results of the energy dissipation for the full configurations, comparing the results of the previous set of experiments (Section 4.2.1) and the current set. The results for experiment set 2 are of the same order and show the same trend as the results from experiments set 1, for each configuration and wave case. From this can be concluded that the experiments are reproducible. The small shift in  $KC$ -number is due to a 5cm water level decrease for set 2, which causes a small increase in the depth-average velocity and  $KC$ .

For  $KC = 10.5$  ( $T=1.75s$ ), the measurements deviate from the general reflection trends for the reflection from the model. For this wave case, the reflection almost triples. As the reflection is one of the constituents of the energy balance, it also affects the calculated energy dissipation, resulting in a lower value.



(a) Uniform dense configuration.

(b) Uniform open configuration.

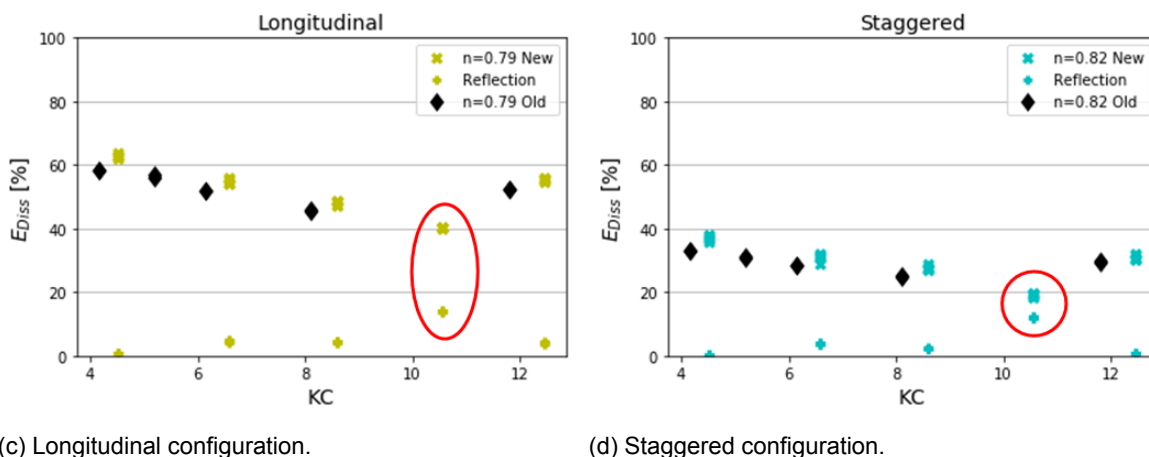


Figure 8.1: Comparison of the energy dissipation with the results of the first set. The red circle at  $KC = 10.5$  marks the 1.75s wave, for which a strange behaviour was observed during the experiments. Here it shows a exceptional high reflection from the model.

Not only the reflection from the model showed a different behaviour for the wave period of 1.75 seconds. Also during the experiments with the empty flume an abnormality was observed. As a check of the instruments, a comparison was made for the velocities of the EMF and ADV in an empty flume. The measured velocities were of the same order for most wave cases, as expected without a model in the flume. However, for the wave period of 1.75 seconds, the behaviour was different. After the reflected wave from the back of the flume reaches the instruments, the velocity for the EMF increases, but for the ADV it decreases. This causes a difference in measured velocity up to 30%. The behaviour might be caused by resonance in the flume. For the 1.75-seconds wave, the distance between the wave board and the model is about 5 wave lengths, the total length of the flume is close to 10 wave lengths.

As the deviations also have an effect on the calibrated amplification factors and force coefficients, the calculated values for the 1.75 seconds wave should be used with care.

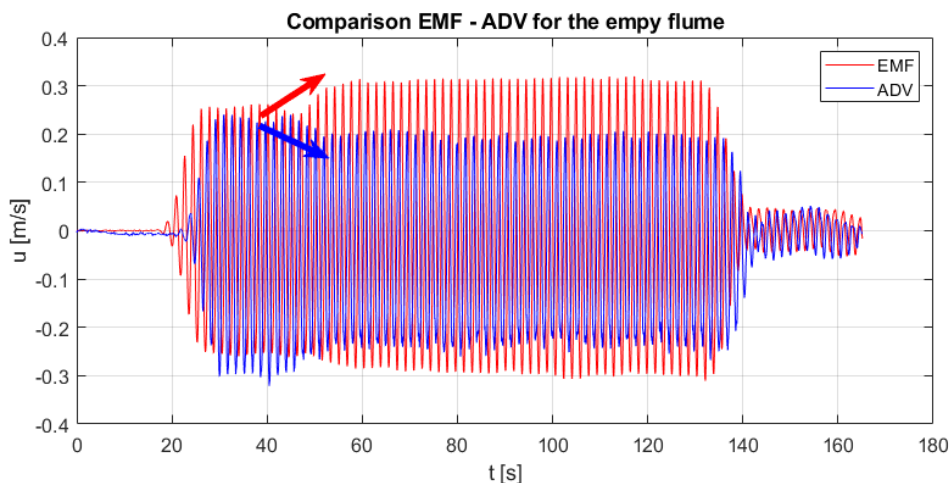


Figure 8.2: Comparison of the velocity measurements from the EMF and ADV for the empty flume with a wave period of  $T = 1.75s$ . After the reflection from the back of the flume reaches the sensors, the measurements show a large deviation.

### 8.1.1. Wave transmission

Based on the Morison equation and linear wave theory, Dalrymple developed a model to describe the decay in wave height along the structure, as explained in Section 2.2. According to this method the wave height decay is given by:

$$K_v = \frac{1}{1 + \beta x} \quad (8.1)$$

With:

$$\beta = \frac{4}{9\pi} C_d D N H_i k \frac{\sinh(kh_v)^3 + 3\sinh(kh_v)}{(\sinh(2kh) + 2kh)\sinh(kh)} \quad (8.2)$$

From the experiments, the transmitted wave height is known for four different structure widths (0.04, 0.28, 0.56 and 0.78m) for the longitudinal and uniform dense configuration. The results from these four experiments are combined to predict the wave height decay over the structure. To compare the theory of Dalrymple with the measured data, the transmission coefficient for the measurements is calculated with:

$$K_v = \frac{H_t}{H_i} \quad (8.3)$$

in wave reflection was subtracted from  $H_i$  for comparison purposes. The results are presented in Figure 8.3, together with the predictions of Dalrymple for two different values of the drag coefficient.

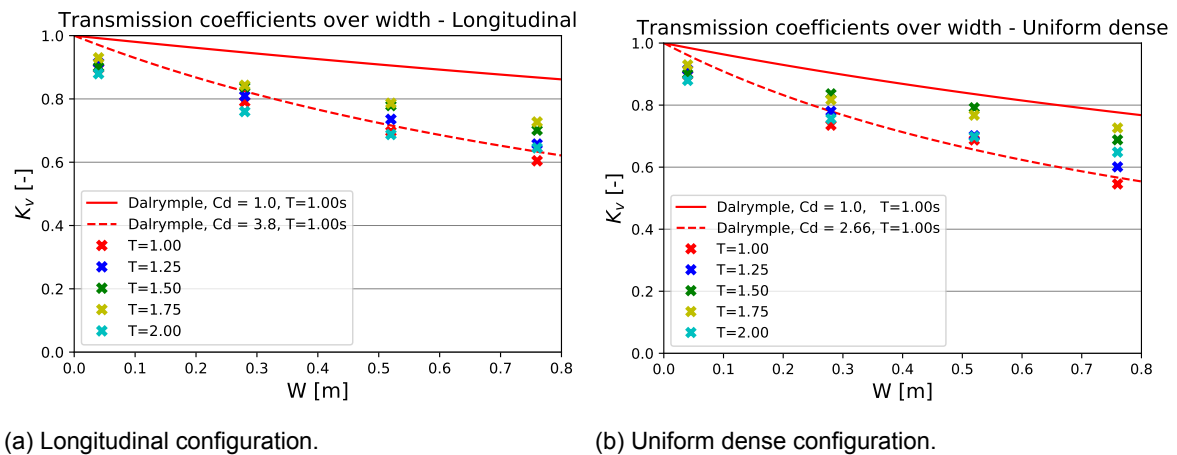


Figure 8.3: Reduction of the wave height inside the structure relative to the incoming wave height, compared with the theory of Dalrymple et al. (1984).

The solid line in Figure 8.3 presents the prediction of the wave height decay by Dalrymple for a  $T = 1.0$ s wave with a drag coefficient of  $C_d = 1.0$ . This is the lower value for  $Re = 10^3 - 10^4$  (Figure 2.11, Munson (2002)). From the comparison with the measured transmission, it is observed that the measured transmission shows the same trend as Dalrymple, but the values are lower. The decay predicted by Dalrymple over-predicts the transmission. The prediction of the energy dissipation based on this profile will result in a value that is lower than measured.

In Section 4.2.3, the drag coefficient in equation 8.2 is calibrated to match the measured energy dissipation. Using the values obtained from the first set of experiments of 3.8 (longitudinal) and 2.66 (uniform) to predict the wave height decay for a 1.0 seconds wave results in the dashed lines in Figure 8.3a and 8.3b respectively. The profile gives a reasonable prediction of the wave height decay for total structure, as the coefficients are calibrated for this width. However, the shape of the profile changes and it still over-predicts the transmission coefficient for the first half of the structure.

## 8.2. Velocity and force signal

### 8.2.1. Mean negative current

During the reference experiments with the empty flume, the observed negative velocities were slightly larger than the positive velocities. By calculating the mean of the depth-average velocity over a wave period, a negative velocity of 0.01-0.03 m/s was observed for the different wave cases, suggesting a negative current in the flume.

The same phenomenon was observed in similar experiments by Pujol et al. (2013) and Hu et al. (2014). Figure 8.4 shows the conceptual profile of the mean current for an empty flume and for a flume with rigid vegetation by Pujol et al. Positive velocities are observed near the bed and near the water surface, while negative velocities are observed in the middle of the water column.

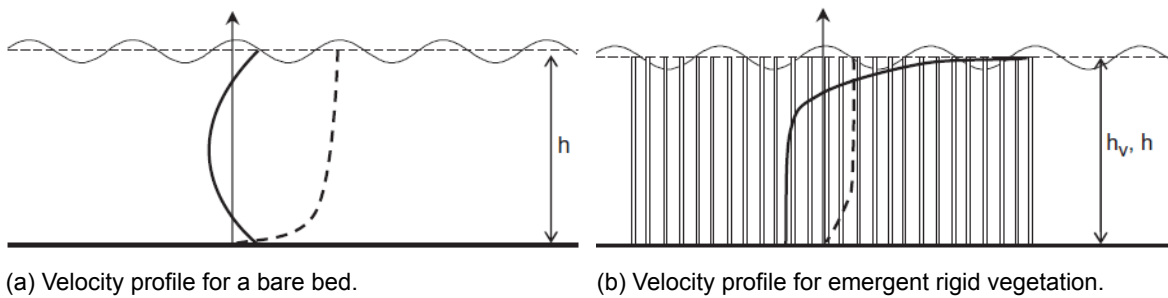


Figure 8.4: Velocity profiles over depth for a situation with only waves and a situation with only current. The solid line is the wave-only situation, the dashed line is the current-only situation. (Pujol et al., 2013)

If velocities are measured between the still water level and the wave crest, the recording will only show positive velocities and only for a part of the wave cycle. For a measurement between the wave trough and still water level, the average values over a wave period will also be positive (Bosboom and Stive, 2015). This results in a transport of momentum in positive direction. As the flume is a system with closed boundaries, the net transport has to be zero, resulting in a transport of momentum in negative direction below the wave trough.

The elevations of the velocity measurements in this research are 0.15, 0.25 and 0.40m, which are in the negative part of the velocity profile in Figure 8.4a. As the positive parts of the profile are not measured, this results in a mean negative velocity. In his study, Pujol et al. suggested that this effect might even increase for emergent rigid vegetation, as depicted in Figure 8.4b. However, as measurements in current study already showed asymmetry due to the measurement location as shown in Figure 6.8, this could not be verified.

### 8.2.2. Amplification factors for the velocity

From Section 7.3 it is observed that the velocity inside the structure increases in relation to the undisturbed flow. To compare the increase in velocity with results from literature, the amplification factor is calculated according to:

$$AF = \frac{u_2}{u_1} \quad (8.4)$$

in which  $u_1$  is the undisturbed velocity and  $u_2$  is the velocity measured inside the structure. In the past, different studies have been done to come up with a description of the velocity inside an array of cylinders/ vegetation based on porosity or element spacing. A study by Huang et al. (2011) assumed the velocity inside the structure to be dependent on the porosity of the structure, according to:

$$u_2 = \frac{1}{1 - \phi} * u_1 \quad (8.5)$$

in which  $u_1$  is the undisturbed velocity,  $u_2$  is the velocity inside the structure and  $\phi$  is the solid fraction of the structure. Another approach is the law of conservation of mass, which states that for an incompressible fluid the incoming mass is equal to the outgoing mass, resulting in:

$$u_1 A_1 = u_2 A_2 \quad (8.6)$$

in which location 1 is the undisturbed flow and location 2 is inside the model.  $A$  is the cross sectional area of the flow. Under the assumption that there is no set-up in wave height, the velocity between the elements for the front row can be calculated according to:

$$u_2 = AF * u_1 \quad \text{with} \quad AF = \frac{A_1}{A_2} \quad (8.7)$$

Figure 8.5 presents the results of the two approaches, together with the amplification factor for the velocity of the front row. The results of the middle and back row are not presented, as these are also influenced by the wave dissipation inside the structure. For the front row, it is assumed that the wave height is still undisturbed and the increase in velocity is only due to a decrease in the cross sectional area of the flow.

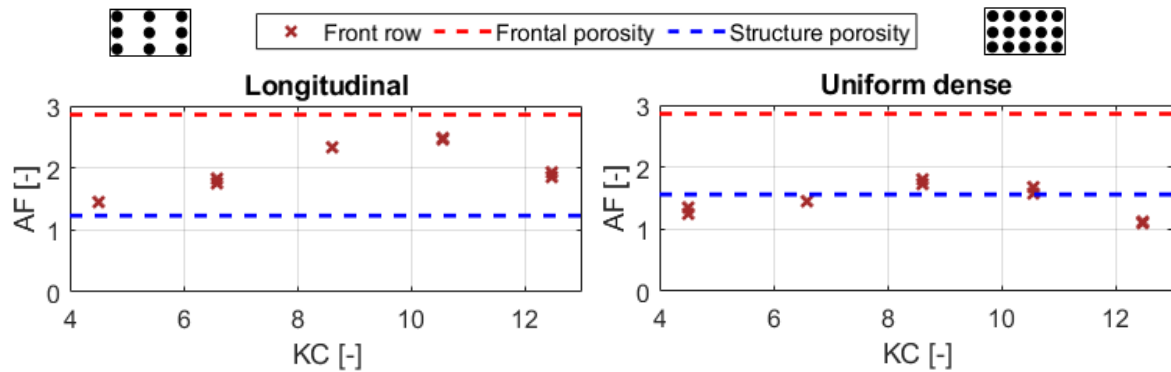


Figure 8.5: Amplification factor for the measured velocity of the front row, compared with theoretical values.

From the figure, it can be concluded that using the frontal porosity of Equation 8.7 results in an over-prediction of the velocity for both configurations, serving as an upper limit for the amplification factor. Using the structure porosity suggested by Huang et al. results in an under-prediction for the longitudinal configuration and a reasonable prediction for the uniform dense configuration. This suggests that the structure porosity of Equation 8.5 might serve as a lower limit for the amplification factor of the velocity.

The figure also shows that velocities inside the structure increase, from which can be concluded that the assumption of undisturbed velocities for the determination of the drag coefficient and dissipation is invalid for structures with a frontal porosity close to 0.35.

### 8.2.3. Amplification factor for the force

To discover the relationship between the velocity and the force, the amplification factor for the force is calculated in relation to the force on a single element:

$$AF = \frac{F_2}{F_1} \quad (8.8)$$

in which  $F_1$  is the force measured on the single element and  $F_2$  is the force measured inside the structure. To make a consistent comparison, also the velocity factor is recalculated with the velocity measured next to a single element. The results are presented in Figure 8.6.

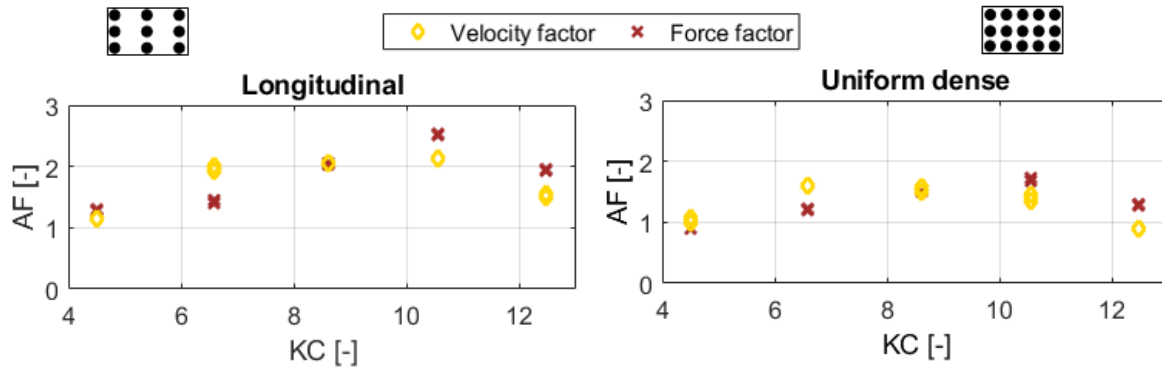


Figure 8.6: Amplification factor for the force in relation to a single element, compared with the amplification factor for the velocity.

The results show that the amplification factors for the velocity and force have the same trend and magnitude, concluding that the velocity and force have a linear relationship. Considering the components of the in-line force described in Section 2.2.2, it can be concluded that the force is inertia dominated:

$$F = F_m + F_d = \frac{1}{4} C_m \rho \pi D^2 \dot{u} + \frac{1}{2} C_d \rho D u |u|$$

As the waves tested in this research are in the low  $KC$ -range, the domination of the inertia component is no surprise. For the longest waves tested, the amplification factor for the force is slightly larger, suggesting that these waves are in the transitional regime from inertia to drag dominated (Etminan et al., 2019). For a drag dominated regime, the forces are related to the velocity squared.

### 8.3. Colour convention

In the following sections, the different configurations and location with the structure are compared. When the comparison is based on the configuration, the colours red and blue are used for the longitudinal and uniform dense configuration respectively (Figure 8.7).

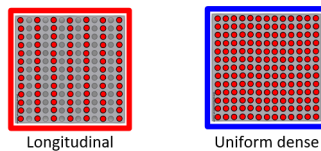


Figure 8.7: Colour convention for the configurations.

When the comparison is based on the location within the model, the colours brown, magenta and green are used for the front, middle and back rows respectively (Figure 8.8). The results for the longitudinal and uniform dense configuration are plotted in separate figures.

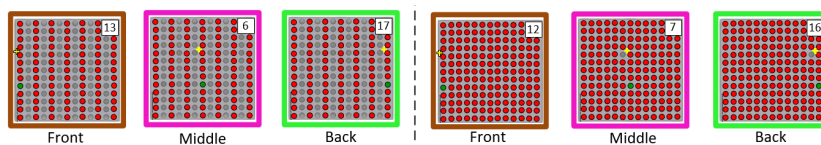


Figure 8.8: Colour convention for the location within the structure.

## 8.4. Method 1 - Calibration from dissipation

Based on a constant pair of coefficient and the measured energy dissipation, an amplification factor for the linear velocity is determined. This factor accounts for deviations from the undisturbed velocities. As it is calibrated on the dissipation, method 1 shows a good agreement between the predicted and measured dissipation ( $R^2 = 0.98$ ). The results are shown in Appendix G.1. The next sections discuss the implications of the obtained results.

### 8.4.1. Amplification factor for the velocity

The calibrated amplification factors for the velocity of the longitudinal and uniform dense configuration have a more or less constant value of 1.4-1.5 and 1.1-1.3 respectively for  $KC < 11$ , although the factor based on the measured data showed a dependency on wave period (Figure 8.5). For  $KC = 12.5$  ( $T = 2.00s$ ), the calibrated factor shows a larger value (Figure 8.9).

From the analysis of the experiments with a current-only condition (see Appendix H), an amplification factor is found related to the frontal porosity of the structure, as described by equation 8.7. The current-only condition can be considered as a wave with an infinite period, resulting in an infinite  $KC$ -number. As the obtained amplification factors show an increase for the larger  $KC$ -number, the factor might increase with increasing  $KC$ , with the factor obtained from the current-only conditions serving as an upper limit for  $KC = \infty$ . However, as this research focused on the low  $KC$ -range and only the 2 seconds wave shows an increase, this hypothesis cannot be validated with the collected data.

Another possible cause can be found in the velocity profile. The calculated amplification factor is valid under the assumption of linear wave theory. However, as the longer wave periods tested in this research tend towards cnoidal waves, the use of linear velocity might not be suitable for this wave condition. This effect is tested by using the undisturbed velocity in Section 8.7.

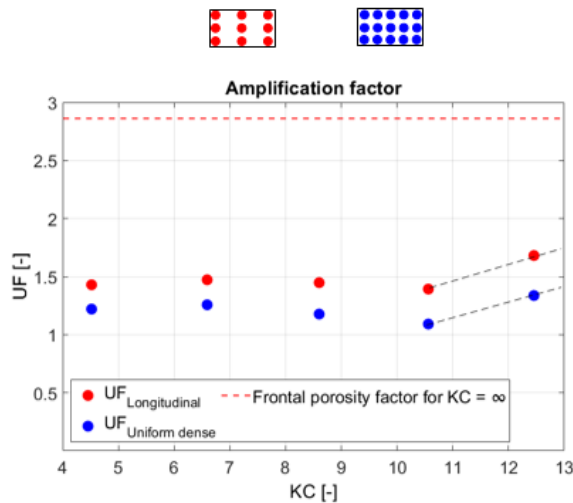


Figure 8.9: Calibrated amplification factors for the velocity.

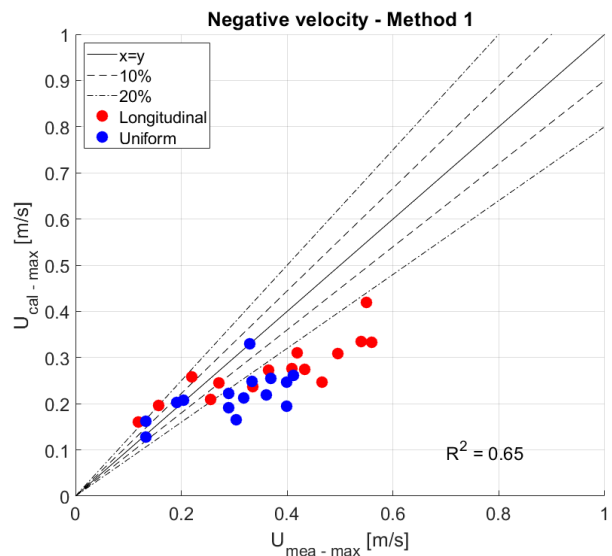


Figure 8.10: Comparing the calculated negative velocity with the measured negative velocity for method 1.

The velocities obtained when using the amplification factors are plotted against the measured values in Figure 8.10. For the lower velocities, the calculated values coincide with the measured values. As the velocities increase, the differences between the calculated and measured velocity also increases. This suggests that sheltering of the elements starts playing a role, as the velocity required for the amount of dissipation is lower than the measured one. For the larger velocities, the excursion length becomes larger. This might result in a more stream-

lined flow between the elements, creating a difference between the velocity experienced by the element and the velocity in the gap between the elements. A sketch of this process was already provided in Figure 5.6 and is further elaborated in Section 9.2 in the discussion.

### 8.4.2. Cross-check: predicted forces

To assess the reliability of the model, the cross-check as described in Section 6.4 is performed. With the constant pair of coefficients and the enlarged linear velocity, the force signal is reconstructed. Based on the mean amplitude, a comparison is made with the measured force. However, the reconstructed force is based on a symmetric velocity signal, while the measured force signal shows asymmetry. It is therefore decided to compare both the positive and negative magnitudes separately. The results are shown in Figure 8.11a and 8.11b, plotted against the measured forces. A visualization of the reconstructed forces can be found in Appendix G.2.

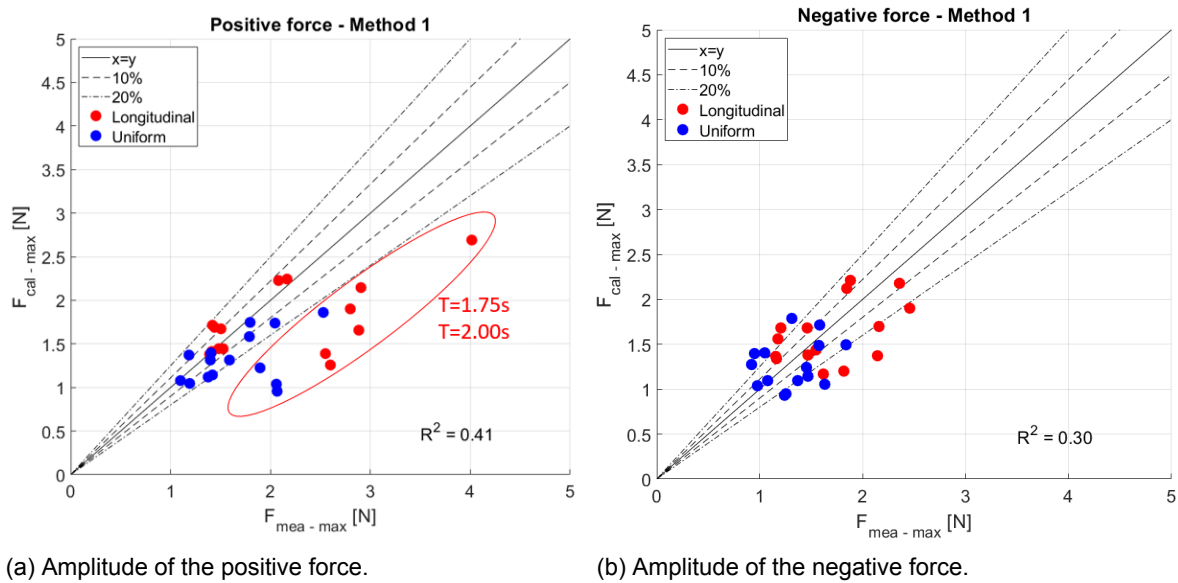


Figure 8.11: Comparing the calculated forces with the measured forces for the longitudinal and uniform dense configuration for method 1.

For the shorter wave periods in this research, the method gives a reasonable prediction for the positive force. Although the scatter in the results is still large, the values show a relation between the measured and the predicted force ( $R^2 = 0.67$  when leaving out the 1.75s and 2.00s waves).

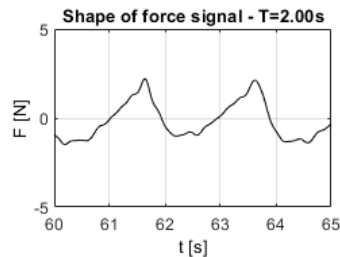


Figure 8.12: Example of the asymmetric shape of the force signal for a  $T = 2.00$  seconds wave.

For the longer wave periods in this research ( $T = 1.75s$  &  $T = 2.0s$ , in the red circle) the differences between the calculated and measured force become larger. This can be explained by the change in the shape of the wave, which was already shown in Figure 6.3. As the wave

period becomes longer, the waves tend towards cnoidal waves. The crest of the wave becomes sharper and higher, while the trough becomes longer and flatter. The high crest results in a sharp positive peak force, which cannot be reproduced with the sinusoidal velocity signal (see Figure 8.12 and Appendix G.2).

## 8.5. Method 2 - Calibration from forces

Based on linear velocity and the measured force, the force coefficients in the Morison equation are determined. Method 2 also shows a good agreement when assessed for its own quantity ( $R^2 \approx 0.9$ ), although it is less than for method 1 ( $R^2 = 0.98$ ). The results are shown in Appendix G.1. The next sections discuss the implications of the obtained results.

### 8.5.1. Force coefficients

#### Comparison with first set

In Section 4.2.3, the drag coefficients for the first set of experiments are determined with the calibration method, as described by Dalrymple et al. (1984). The obtained drag coefficients are in the order of 2.5-5.0. In method 2, the drag coefficients are calculated for the second set of experiments, now based on a semi-direct measurement method. As this is based on the measured force signal, it is expected that this method results in lower and more realistic values of the coefficients. The results of both approaches are plotted in Figure 8.13.

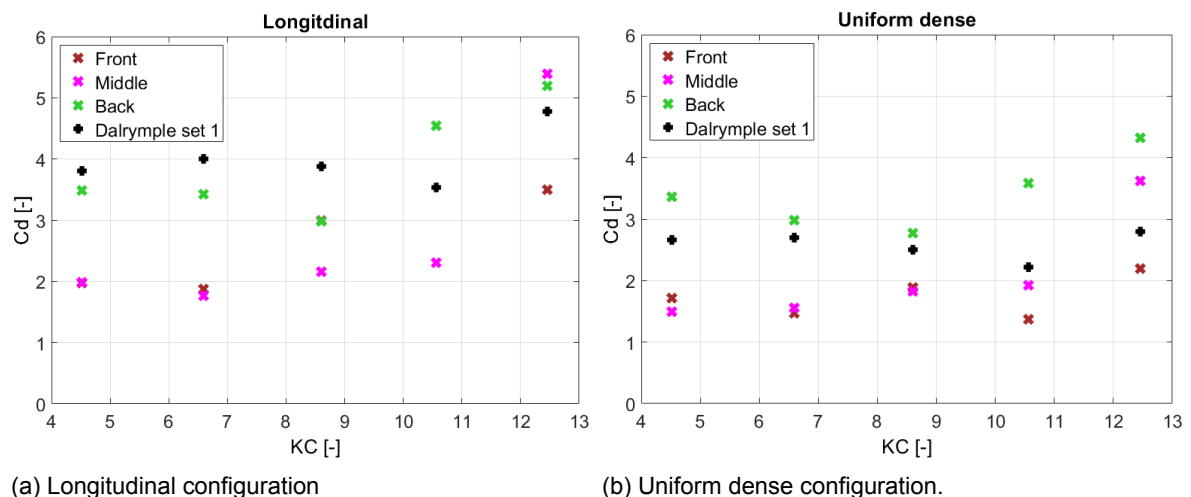


Figure 8.13: Comparison of the drag coefficients obtained by the semi-direct measurement method in experiment set 2 with the coefficients obtained by the calibration method in experiment set 1.

From the figure, it is observed that the drag coefficients for the front and middle row are indeed lower than the calibrated drag coefficient, except for the 2.0 seconds wave ( $KC = 12.5$ ).

However, for the back row the coefficients from method 2 are even higher for some wave cases. This can be caused by an error in the assumption of the velocity inside the model. For the calculation of the velocity, the wave height at the end of the model is assumed to be equal to the wave height measured by the wave gauges 2.5m behind the model. Due to interaction between the wave and the elements, the wave height decay inside the model might be less than assumed, resulting in a larger velocity and lower coefficients.

#### Comparison with literature

In the past, many studies have been done on the effect of vegetation in waves and current, as discussed in Section 2.3. For this research, which focuses on rigid elements in waves, the study of Ozeren et al. (2014) is most comparable. In the study by Ozeren et al., the vegetation was schematized as rigid wooden cylinders subjected to regular waves. The drag coefficient was then calibrated based on transmitted wave height as described by Dalrymple

et al. (1984). The results obtained in this study by a semi-direct measurement method are plotted in Figure 8.14, on top of the results by Ozeren et al.

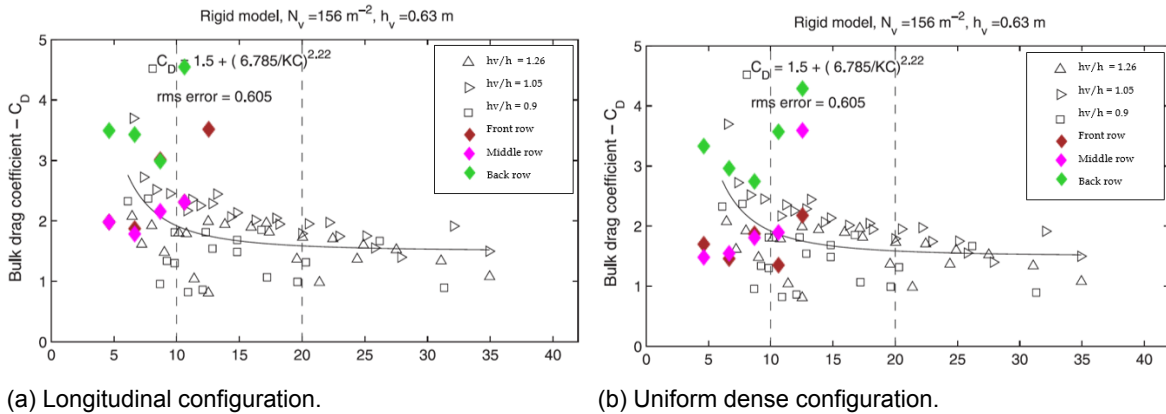


Figure 8.14: Comparison of the drag coefficients for the front, middle and back row with the results of Ozeren et al. (2014).

Although the density and diameter is different, the obtained results are comparable. For the front and middle row, the obtained coefficients lay on top of the results of Ozeren et al. The values for the back row are somewhat larger, especially for the longer waves.

Another study with rigid wooden cylinders is the study by Hu et al. (2014), who obtained the drag coefficients by the direct force measurement method. In this study, the cylinders are subjected to a combination of waves and current, which results in a relationship between  $C_d$  and  $Re$ . A more recent study by Chen et al. (2018) used the results obtained by Hu et al. and the model of Losada et al. (2016) to come up with a relationship between  $C_d$  and  $KC$ , for both pure wave cases and current-wave cases. The results are plotted in Figure 8.15. The plot shows results for both emergent and submerged cylinders in pure wave cases and combinations of waves and current.

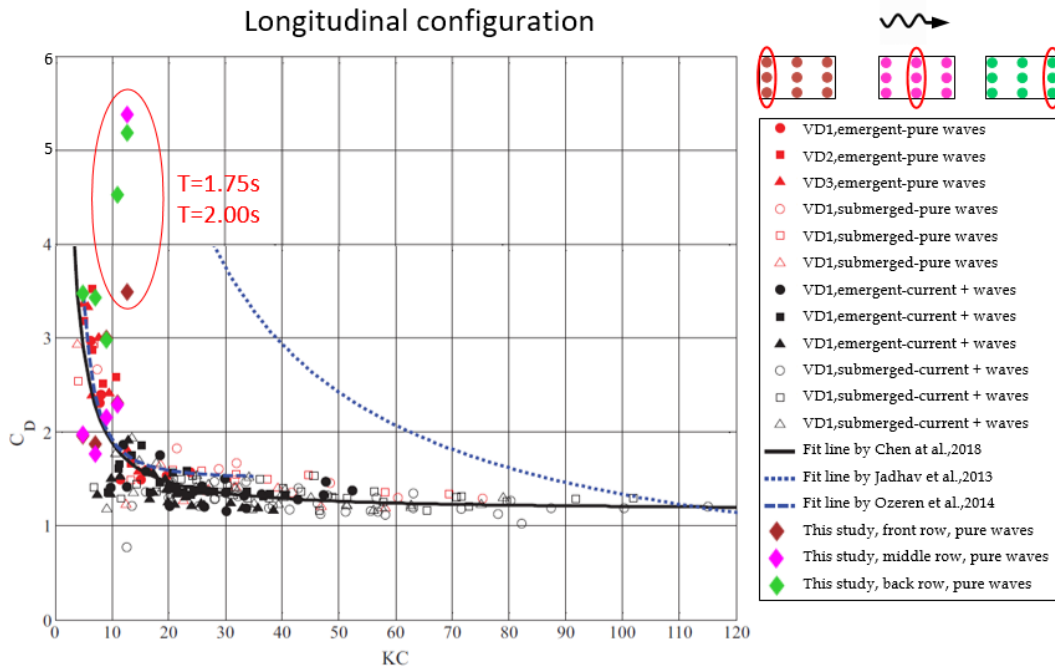


Figure 8.15: Drag coefficient as a function of  $KC$  for both wave-only and wave-current conditions. (Chen et al., 2018). Results of this study for the longitudinal configuration lay within the range of previous results.

For both configurations, the obtained drag coefficients lay within the range of the results by Chen et al. (2018). Only exception are the long waves, for which high drag coefficients were found. But as these waves tend to cnoidal wave, the assumption of linear theory for the determination of the force coefficient might cause the high values.

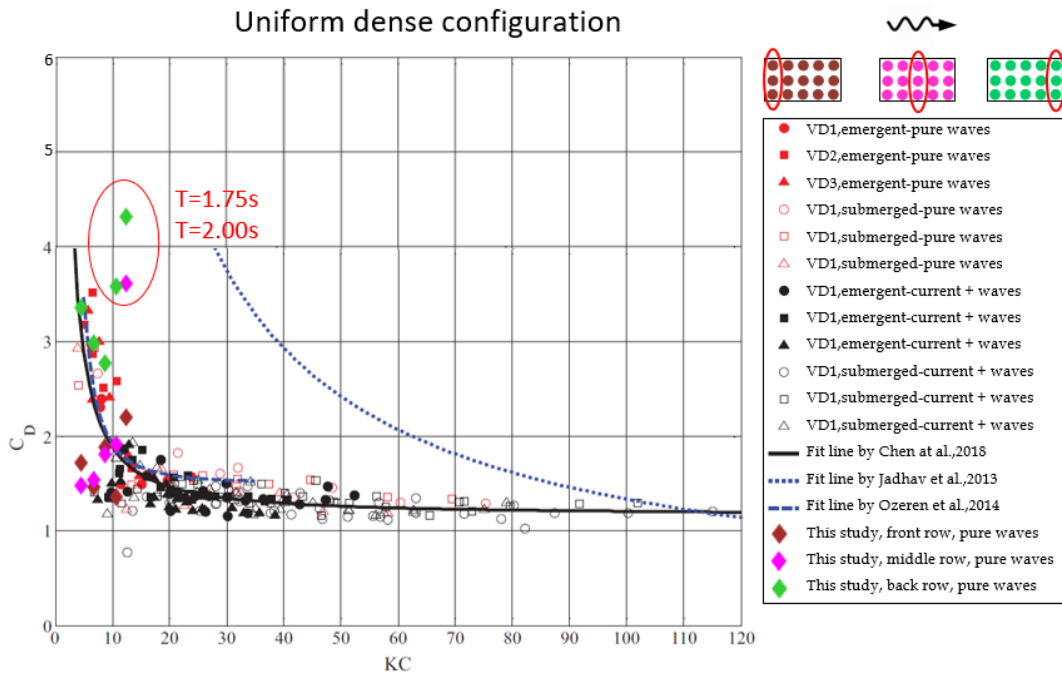


Figure 8.16: Drag coefficient as a function of KC for both wave-only and wave-current conditions. (Chen et al., 2018). Results of this study for the uniform dense configuration lay within the range of previous results.

### 8.5.2. Velocity signal

For method 2, the velocity signal used for the calculations is the velocity of linear theory, adapted for the wave height inside the structure. Figure 8.17 shows that for the low velocities, the values coincide with the measured values. For the larger velocities however, the calculated velocity is much lower than the measured velocity.

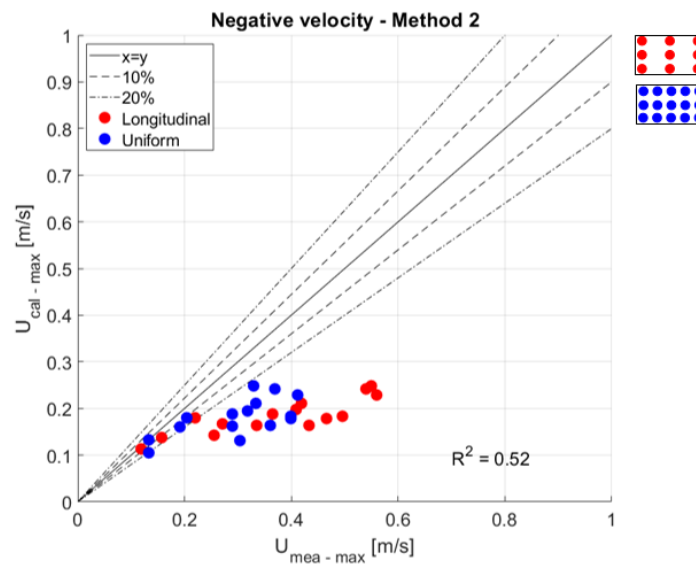


Figure 8.17: Comparing the calculated negative velocity with the measured negative velocity for method 2.

### 8.5.3. Cross-check: predicted energy dissipation

The reliability of the model is checked by performing a cross-check as described in Section 6.4. Based on the velocity of linear theory and the obtained force coefficients, the energy dissipation is calculated, as explained in Appendix F. The results are plotted against the measured energy dissipation in Figure 8.18.

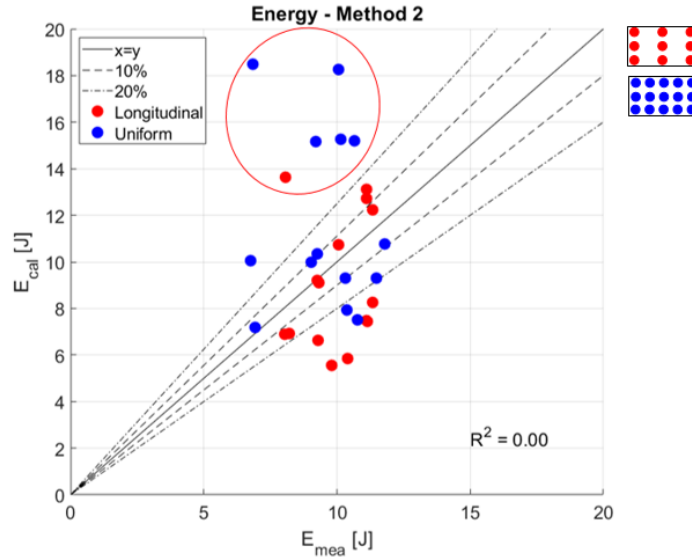


Figure 8.18: Comparing the calculated energy dissipation with the measured energy dissipation for method 2.

The results shows that force coefficients, which accurately predict the forces, do not results in a good prediction of the energy dissipation. The prediction shows a large spread and an  $R^2$  value of 0.0. For most wave cases, the dissipation is under-predicted. When the coefficients of the last row are used, the dissipation is over-predicted (red circle).

It can be concluded that method 2 cannot be used for the prediction of the energy dissipation and is not representative for what happens in reality.

### 8.6. Comparison of both methods

The two methods analyzed in previous sections are based on two different principles. Method 1 is based on the assumption that increase in energy dissipation for the different configurations is due to an increase in velocity inside the model. Method 2 is based on the assumption that the velocity does not increases, but that the drag of the elements increases due to interaction of the elements.

Both methods perform well when assessed for their own quantity. The  $R^2$  value for method 1 is 0.98, for method 2 it is around 0.9 (see Appendix G.1). The lower value for method 2 is no surprise, as the predicted force is calculated based on a symmetric sinusoidal velocity signal, whereas the measured force signal shows asymmetry (see Appendix G.3). Comparing the velocities it is observed that for both methods, the velocities used in the calculations are lower than the measured velocities. However, in method 1 an amplification factor for the velocity is calibrated, which brings the calculated velocities closer to the measured ones.

The performed cross-checks give more insight into the performance of both methods. For method 1, the prediction of the force is not ideal, but it is within reasonable bounds. It shows a relation with the measured force, especially for wave periods around  $T = 1.0s$ . For method 2 however, the prediction of the energy dissipation does not match with the measured energy dissipation. From this analysis, it is concluded that method 1 has overall a better performance and is a better representation of reality, although it shows considerable scatter.

If the energy dissipation due to the inertia force is considered negligible (Dalrymple et al., 1984; Mendez and Losada, 2004) and the increase in dissipation is due to an increase in velocity as stated in method 1, the drag coefficient obtained by method 2 can be converted into an amplification factor for the velocity. The drag force responsible for the energy dissipation is given by:

$$F_d = \frac{1}{2} \boxed{C_{d,cal}} \rho D u^2$$

with in the red box the calibrated factor of method 2. Under the assumption that the increase in drag force is caused by the increase in velocity, the drag coefficient is assumed to be 1.0 (blue box). The calibrated drag coefficient is then used as amplification factor for the velocity squared (red box):

$$F_d = \frac{1}{2} \boxed{1.0} \rho D \boxed{C_{d,cal} u^2}$$

To compare the factor with the amplification factors for linear velocity obtained in method 1, the square root of the drag coefficient is taken (red box):

$$F_d = \frac{1}{2} \boxed{1.0} \rho D \boxed{(\sqrt{C_{d,cal}} u)^2}$$

From this derivation then follows:

$$UF = \sqrt{C_d}$$

This derivation is the applied on the coefficients obtained in method 2. The results of the calculation are shown in Figure 8.19 for the front, middle and back row.

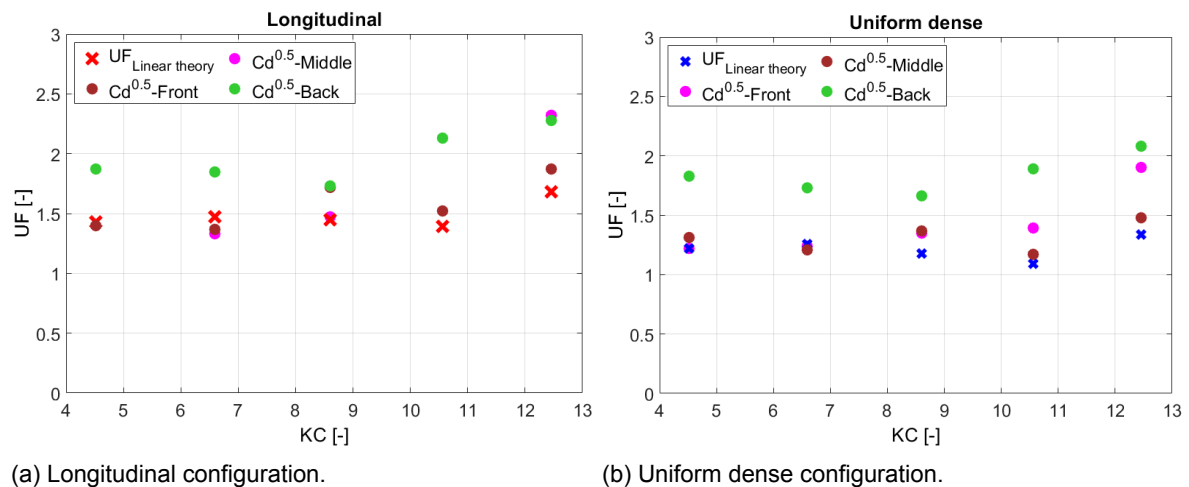


Figure 8.19: Comparing the amplification factor for the velocity from method 1 with the factor derived from method 2.

From Figure 8.19 is observed that for the front row, the square root of the drag coefficients results in an amplification factor that is comparable to the values obtained in method 1. For the short waves, this is also valid for the coefficients of the middle row. Only for the 2 seconds wave ( $KC = 12.5$ ), the factor increases. The factors for the back row are larger, which might be due to an error in the assumption of the wave height, as discussed in Section 8.5.1.

As both methods now result in an amplification factor of the same magnitude, this strengthens the conclusion that the drag coefficients has a value close to 1.0 and that the increase in energy dissipation is due to the increase in velocity for the different configurations.

### 8.7. Method 1 with measured velocity of empty flume

In reality, it is more beneficial for application purposes to link the velocity inside the model to the undisturbed velocity. Therefore, method 1 is also executed with the velocity of the empty flume as input. The results are shown in Figure 8.20, together with the amplification factor for linear theory and the front row as described in Section 8.6. The measured velocities for the empty flume were close to linear wave theory, resulting in amplification factors that are of the same order as the ones obtained in method 1.

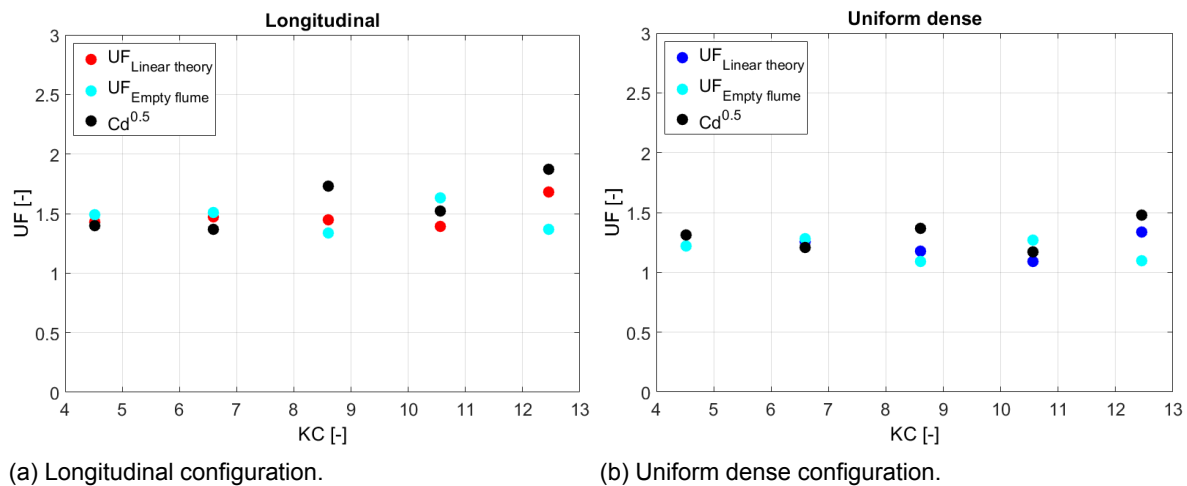


Figure 8.20: Comparing the amplification factor for linear theory with the factor for undisturbed flow.

For the longitudinal configuration, Figure 8.20a shows a constant value around 1.5. The increase that was observed for the 2.0 seconds wave ( $KC = 12.5$ ) when using linear theory, is not observed when the measured velocity is used. This suggests that the increase is indeed due to the assumption of the velocity profile, as discussed in Section 8.4.1. For the uniform dense configuration, even a slight decrease is observed in the amplification factor in Figure 8.20b.

## 8.8. Executive summary

This section summarizes the most important points and observations of the analysis of the second set of experiments.

- The dissipation results of the second set are comparable with the results of the first set, concluding that the experiments are repeatable.
- For the  $T = 1.75$  seconds wave, a strange behaviour is observed during the experiments. The measured reflection from the model shows a large increase in relation to the other wave conditions. Also the velocity measured by the ADV and EMF without a model in the flume shows a difference of around 30%.
- The velocity inside the structure increases in relation to the undisturbed velocity, making that the theory of Dalrymple based on linear theory is not valid for present application.
- An amplification factor based on the structure porosity can serve as a lower limit for amplification factor of the velocity, whereas a factor based on the frontal porosity of the structure can serve as an upper limit.
- The amplification factor for the velocity and force show the same trend and magnitude, concluding the experiments are in the inertia dominated regime.
- Method 1 results in a accurate prediction of the energy dissipation and a reasonable prediction of the forces. It can be concluded that the drag coefficient is close to the value of a single cylinder and that higher values are due to a wrong assumption of the velocity inside the array.
- The amplification factor calibrated in method 1 shows a constant value over the wave periods for both the longitudinal and uniform dense configuration, with a larger value for the longitudinal configuration. The amplification of the velocity is a function of both the frontal porosity and the structure porosity.
- Drag coefficients obtained with method 2 show a good agreement with values from literature.
- Method 2 results in a good prediction of the forces, but cannot predict the energy dissipation. This leads to the conclusions that an increase in drag coefficient is not representative for what happens in reality.



# 9

## Discussion

*In this chapter, an evaluation of the experiments, methods and results is presented. This includes a discussion about the reliability of the measured data and the assumptions made in the calculations. The first Section (9.1) focuses on the performance of the experiments, the second Section (9.2) on the data processing. It concludes with a connection between the different part of the research by discussing the relevance in Section 9.3.*

### 9.1. Performance of experiments

#### Use of the ADV

During the experiments, an ADV sensor was used to measure the velocity inside the structure. The instrument determines the velocity by emitting an acoustic signal and measuring the reflected signal from particles in the water. By placing the instrument inside the model, it is surrounded by the aluminum elements and an aluminum bottom plate. As this is a hard and smooth material, it also reflects the emitted signal, resulting in some noise in the velocity signals. The reflection from the bottom plate resulted also in an interference of the signals, making it impossible to measure at certain heights in the water column (below 0.14m and between 0.27-0.34m). In this research, a plastic triangle was placed at the bottom to deflect the reflection from the bottom. This improved the signal, but was still not optimal. The use of softer materials or elements with an irregular surface (like bamboo) will reduce the noise.

In this research, the ADV was located at the front of the row under consideration, as discussed in Section 6.1. The recorded velocity signal showed the amplification of the velocity between the element for the negative part of the wave cycle, but did not record it for the positive part. In order to apply the direct-force measurement method, it is important that the velocity signal has the same shape as the force signal.

#### Sensitivity of force sensor

For the measurement of the force signal, a force sensor with a range of 0-122N (12.5kg) was used. However, maximum measured forces were only up to 6N, using only 5% of the range of the sensor. Also, the displacements of the element were very small, which required an amplifier of 3080x. The combination of a large range for the force sensor and the use of the amplifier might result in measurement inaccuracies in the force signal.

#### Wave absorber

To reduce the effects of a reflected wave from the back of the flume, a wave absorber with a slope of approximately 1:3 was applied. This reduced the amount of reflection significantly. However, still an interaction between the incoming and reflected wave was observed (see for example 8.2), which has an effect on the measured velocity and force inside the model. In reality, the foreshores on which the structures will be build have slopes up to 1:1000, for which wave reflection can be neglected. The use of a milder or more porous wave absorber in the flume might reduce the reflection, which results in a better representation of reality. However, a milder slope requires more space, which is not available in most wave flumes.

### Experiments with current-only

As a reference situation for an infinite  $KC$ -number, a few experiments with a current-only condition were performed. Also for these experiments, the ADV was located at the front of the row under consideration, which means that the ADV measured the incoming flow before it was accelerated between the elements. The amplification factor for the velocity is then obtained in an indirect way by assuming that the drag coefficient is close to  $C_d = 1.0$ . If the ADV is located at the back of the row under consideration, it will capture the effect of the jet generated between the element and the increase in velocity can be obtained directly.

Due to time limitations, no actions were taken to create a smooth inflow of water, resulting in a non-uniform flow. The flow through the model itself also generated a lot of small-scale turbulence. As a result, the measured force and velocity signals measured inside the model showed fluctuations over time. However, during the calculations the signals are averaged over time, ignoring the local fluctuations.

### Measurement of the lift force (transverse direction)

Due to vortex-shedding, as discussed in Section 2.2.2, a force component in the transverse direction is also present, which is called the lift force (Equation 2.13). A study by Etminan et al. (2019) found that these forces are negligible for low  $KC$ -numbers ( $KC < 7$ ), but then start increasing with increasing  $KC$  due to the increase in vortex-shedding (see Figure 9.1). For a single cylinder, the resultant mean force of the lift force is assumed to be zero due to the symmetry of the wave. However, as Figure 9.1 shows that the density of the structure has an effect on the magnitude of the lift force, it might also cause an asymmetry contributing to the energy dissipation.

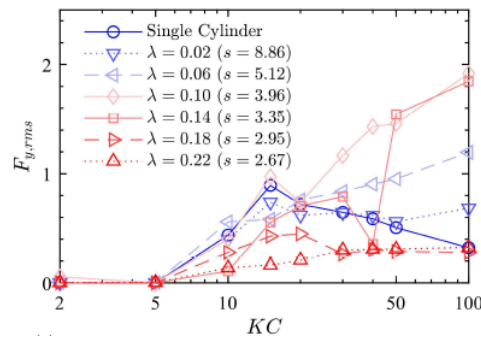


Figure 9.1: The root-mean-square of the lift force plotted against  $KC$ , for different structure densities (Etminan et al., 2019).

During the experiments, forces were only measured in the direction of wave propagation. To study the possible effect of an asymmetric lift force on energy dissipation, it is advised to measure the force also in transverse direction.

## 9.2. Data processing

### Comparison of the models with different diameter

In this study, a comparison is made between the obtained results and the results of Haage (2018), who uses a model with an element diameter of 2 centimeter, to assess the effect of the element diameter on the energy dissipation. A direct comparison of the amount of dissipation was not possible, as with the change in diameter also the porosity of the structure had changed. A comparison is made based on a simplified drag coefficient. This includes the number of elements and the diameter, but is based on the assumption of linear theory. However, from the second set of experiments it follows that the velocity inside the structure is a function of frontal porosity and structure porosity, which are different for both models. A correction for the acceleration inside the models might lead to different results than obtained in this study.

### Filtering of the signals

For the processing of the force and velocity signal, a low-pass frequency filter was applied with a maximum frequency of  $5\text{Hz}$ , based on the natural frequency of the system. As in this research all the quantities were considered depth-averaged, local fluctuations on the scale of turbulence were ignored and this method of filtering was applicable. However, when interested in the local turbulence and peaks in the velocity signal, a filter with a larger pass-band might be more suitable.

### Effect of negative mean current

During the experiments without a model in the flume, a mean negative velocity of  $0.01\text{--}0.03\text{m/s}$  was observed. However, the calculations of the energy dissipation were based on a linear velocity profile, which is a perfect sinusoidal signal around zero, neglecting a possible return current. Research by Pujol et al. (2013) even stated that for an array of rigid emerged cylinders, the mean negative current was stronger inside the array compared to the situation without cylinders. If a return current is present, this might influence the comparison between the measured and calculated velocities, as the measured values will include this effect and show a larger value.

### Calculation of the velocity profile over depth

In the present study, the velocity profile over depth is calculated based on the velocity measurements from three different experiments, through which the profile of linear theory is fitted. The profile is a reasonable representation of the magnitudes of the velocity, but ignores local variations over height and over time. Figure 9.2 gives an example of the fitting for which the errors are larger. By measuring the velocity at three points over height in the same experiments, variations in time are cancelled out.

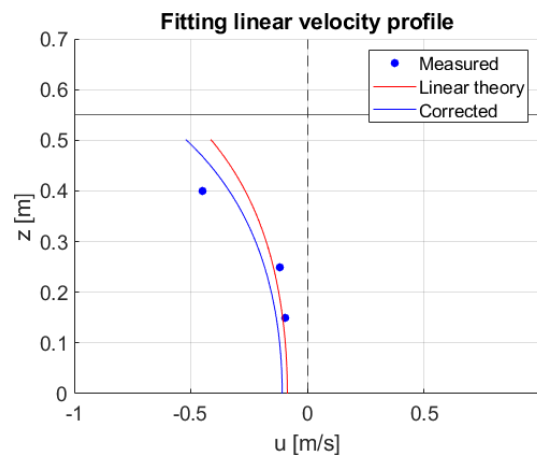


Figure 9.2: Example of a fitting of the velocity for which the deviations are larger.

### Assumption of decreasing wave height inside the structure

To calculate the velocity inside the model, a profile for the decay of the wave height inside the structure is assumed based on the transmission factors ( $K_v$ ) for different structure widths. The factor is based on the measured incoming and transmitted wave height. The incoming wave height is corrected for the reflection measured for each width, but this approach neglects the interaction that the each row may have with the rest of the structure. From the data it is observed that not only the dissipation increases with an increasing width, but also the reflection from the structure. The behaviour of a wave halfway a full configuration may be different from the behaviour of a wave at the end of half a configuration, although the location is the same. For the full configuration, the wave might interact with the second half of the structure in the form of reflection, whereas for half the configuration the wave can travel undisturbed.

The calculation of the velocity based on the wave height in the model also causes a disadvantage for the model used for the calibration of the amplification factor of the velocity (method 1). As the wave height is a measured quantity, the model is still not predictive. It can explain what happens in the tested configurations, but cannot make a prediction if the characteristics of the structure change, as the decay of the wave height will be different.

#### Assumption of constant force coefficients in method 1 (Calibration from dissipation)

To calculate the amplification factor for the velocity in method 1, a constant pair of force coefficients of respectively  $C_d = 1.0$  and  $C_m = 2.0$  is assumed. From literature, these coefficients can be assumed to be valid for a single cylinder. However, for the coefficients inside an array of cylinders, a wide variety of values is found (Ozereen et al., 2014; Hu et al., 2014). A study by Nepf (1999) investigated the effect of the relative distance of 2 cylinders on the value of the drag coefficient. The contours obtained for the coefficient are shown in Figure 9.3a. The plot shows a decrease in drag coefficient when the distance becomes smaller.

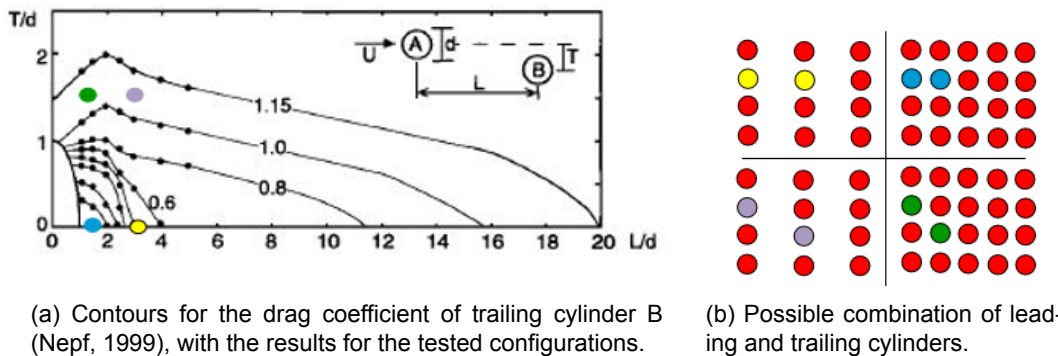


Figure 9.3: Influence of the relative element distance on  $C_d$ .

Nepf (1999) conducted her experiments with 2 cylinders. However, in an array of cylinders, the leading cylinder (A in Figure 9.3a) might have an effect on more than 1 cylinder. In Figure 9.3b, two different combinations of the leading and trailing cylinder are shown for the longitudinal and uniform dense configuration. If the trailing cylinder is under an angle, the drag coefficient is slightly larger than 1.0 (Nepf (1999) assumes a drag coefficient of  $C_d = 1.17$  for an isolated cylinder). For the trailing cylinder in line with the leading cylinder, he finds  $C_d$ -values that are significantly lower. Using these low values of the drag coefficient in the calibration of method 1 results in larger amplification factors for the velocity.

### Sheltering of the elements

In Section 8.4.1, the calibrated amplification factor is used to calculate the velocities. From Figure 8.10, it is then concluded that for the lower velocities, the calculated values coincide with the measured values. However, for the longer waves, the calculated values are lower than the measured ones.

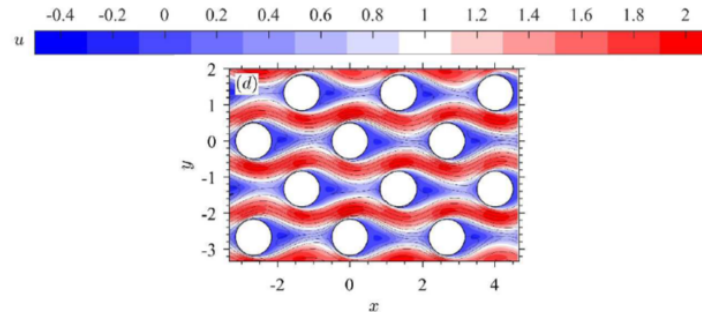


Figure 9.4: Instantaneous stream-wise velocity component contours at  $KC = 15$  (Etminan et al., 2019).

A possible explanation for this can be found in the velocity experienced by the element. As the elements are close together, the trailing cylinder might be in the wake of the leading cylinder, resulting in an experienced velocity that is lower than the velocity measured between the elements. The difference in velocity is also observed in computations by Etminan et al. (2019) for a staggered configuration. Figure 9.4 shows the velocity profile, with a streamlined flow between the elements and wake areas generated around the elements.

A similar phenomenon might happen in the performed experiments. A sketch of the possible processes for a short and a long wave for the tested configurations is shown in Figure 9.5. For the short waves, the flow might diffuse more as the velocities are lower and the period is shorter, resulting in only a small difference between the velocity experienced by the element and the measured velocity. For the longer waves, the flow might become more streamlined between the elements, causing a larger difference between the velocity experienced by the element (in the blue area) and the measured velocity (in the red area). If the drag force (and with that the dissipation) is governed by the velocities in the blue area and the measured velocity is in the red area, this might explain the differences between the calculated and measured velocities when the velocities become larger.

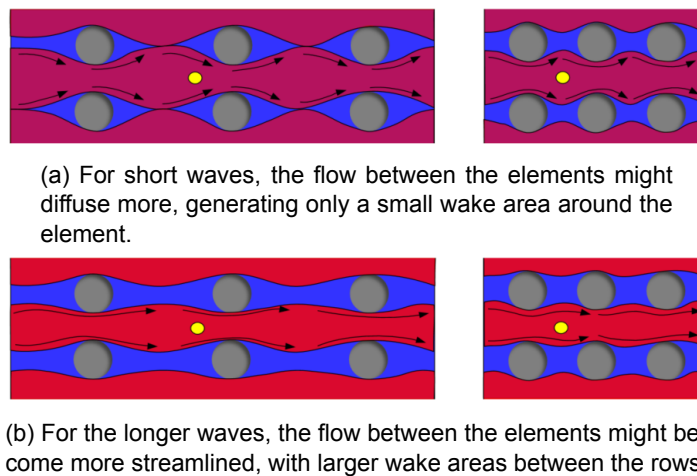


Figure 9.5: Sketch of possible sheltering processes. The red area marks the high velocities, the blue area the wake of the elements. The yellow circle marks the location of the velocity measurement during the experiments.

### Performance of method 2 (Calibration from forces)

The force coefficients obtained in method 2 showed an accurate prediction of the force, but could not predict the energy dissipation. For the front and middle row the results were too low and for the back row the results were too high. The high values could be explained by an error in the assumption of the velocity inside the model, as explained in Section 8.5.1. A possible explanation for the low values can be found in the calibration. The drag coefficients are calibrated to match the force signal, based on a velocity signal of linear wave theory. The drag force is proportional to the drag coefficient times the velocity squared:

$$F_d \propto C_d u^2 \quad (9.1)$$

However, the analysis showed that the increase in force was due to the increase in velocity, instead of an increase in drag coefficient. In the calibration, the drag coefficients are compensating for this increase in velocity. In the calculation of the dissipation, the energy dissipation is proportional to the drag coefficient times the velocity to the power of 3:

$$E_{diss} \propto C_d u^3 \quad (9.2)$$

Using the drag coefficient calibrated to  $u^2$  in a calculation with  $u^3$  will result in values that are too low, as the drag coefficient is only compensating for the velocity squared. The same principle was applied in the comparison of the two methods in Section 8.6.

### 9.3. Relevance of the results

This section discusses the relevance of the results and explains how the different parts link to each other. The research is performed as part of the PhD project of A. Gijón Mancheño, which itself is part of the Building with Nature project BioManCo. The PhD project focuses on the use of permeable structures to restore the mangroves forests. Current work continued on the work of Haage (2018), who conducted experiments similar to the first experimental set conducted in this research (Chapters 3-5), on a model with elements with a diameter of 2cm. Her research compared the total amount dissipation for different configurations, to see which one was to most effective. The present work includes a similar analysis, but for a model with elements with a diameter of 4cm, to see possible effects of the diameter. In experiment set 2, the measurements are expanded with a force and velocity sensor to validate the assumption of linear wave theory.

In Section 4.2.1, the total amount of energy dissipation was compared to assess the model performance. This resulted in two configurations that were most effective in terms of energy dissipation; the longitudinal and uniform dense configuration. By comparing their effectiveness in Section 5.2.3, it was concluded that the longitudinal configuration was the most effective per element, whereas the uniform dense configuration was the least effective. However, what caused this difference in effectiveness was still unknown. Also a calibration of the drag coefficients with the theory of Dalrymple could not explain it, as the obtained values were relatively large in relation to literature. This implies that the velocity used in the calculation (the undisturbed velocity) is too low and that the theory of Dalrymple is not applicable in the applied test conditions.

The analysis of the second set of experiments then showed in Section 8.2.2 that the assumption of linear wave theory is not valid for the applied porosities. An increase in velocity and force was observed for both configurations, with larger values for the longitudinal configuration. For the velocity, a lower and upper limit for the amplification factor was found based on structure porosity and frontal porosity respectively. During the analysis of the two methods, shown in Section 8.4, it was concluded that the increase in velocity is an important factor in the energy dissipation. Section 8.5 showed that the drag coefficients fitted to the measured forces were smaller than the ones obtained from the energy dissipation in set 1. However, the coefficients could not predict the energy dissipation, as they are not interchangeable between force and energy dissipation. This was further elaborated in the previous section.

The results and analysis of this research show a step forward in the understanding of the processes inside the structure, with the increase in velocity inside the structure as an important factor. At the same time the results make it clear that a lot is still unknown, as it was also discussed in previous sections. The applied methods are able to explain some of the processes, but they still lack the possibility to predict the energy dissipation when the characteristics of the structure change. Further research is required and should focus on the longitudinal configuration. Recommendations for this are given in Section 10.2.

### **Relation to other studies**

As shown in Table 2.3, many studies have been done on vegetation/ cylinders under wave loading, in order to determine a relationship for the drag coefficient based on  $Re$  or  $KC$ . One of the studies that is quite similar to current research is the one of Hu et al. (2014). In their research, Hu et al. (2014) performed both the calibration and direct force measurement method on wooden rods of 1cm diameter. They developed a relationship between  $C_d$  and  $Re$ , with a decreasing drag coefficient for an increasing Reynolds number. Later, Chen et al. (2018) used the data of Hu et al. (2014) to obtain a relation between  $C_d$  and  $KC$ , which was shown in Figure 8.15 and 8.16. The results obtained from calibration on the force signal in current research showed the same magnitude.

To compare the calibration method and the direct force measurement method, Chen et al. (2018) used an approach similar to Figure 6.9 (which was adapted from his work). They concluded that both methods perform well for their own linked quantity (dissipation and force respectively), but do not perform so well for their counterpart. The same was observed in this study, when comparing the calibration of an amplification factor for the velocity and the calibration of the force coefficients. The conclusion of Chen et al. (2018) was that the direct force measurement method was, although not optimal, the best method to obtain the drag coefficient.

These previous studies focused on the determination of the force coefficients. The current study focused however on the behaviour of the velocity when going from undisturbed flow (flow without the influence of the structure) to the flow inside the structure. A drag coefficient of 1.0 was assumed (Hu et al. (2014) gives a value close to 1.0 for the range of Reynolds numbers applied in this research), for which an amplification factor for the velocity was calibrated. The measurements and calculations show that the velocity significantly increases for lower porosities, which leads to the conclusion that method 1 (calibration of an amplification factor) is closest to reality.

The combination of this research and previous research shows that both the values of the drag coefficient and the velocity are important in making a prediction of the energy dissipation inside a permeable structure. As the dissipation is related to  $C_d u^3$ , it is even more important to understand the behaviour of the velocity. This research provides a step forward in that understanding.



# 10

## Conclusion and recommendations

*This chapter is the closing of the research and contains the conclusions on the research questions in Section 10.1, based on the results of Chapters 4 and 7 and the analysis of these results in Chapters 5 and 8. Based on the obtained results and the knowledge gaps still existing, recommendations for further research are presented in Section 10.2.*

The goal of this research was to obtain a better understanding of the processes that cause the energy dissipation within a permeable structure and validate assumptions made in previous research, such as using linear wave theory for the determination of the drag coefficient.

The main question of this research was formulated as:

**How do the *physical processes of drag force, velocity increase and possible non-linearity's influence the wave dissipation inside a permeable structure?***

The following sub-questions supported the main research question:

1. How does the dissipation of wave energy change for different configurations and wave conditions?
2. What is the influence of element\* diameter on wave energy dissipation?
3. What is the relative importance of the physical processes causing the wave dissipation?
  - (a) How does the relative importance of the processes change for different wave conditions?
  - (b) How do those processes change for vertical/horizontal orientations? And for different arrangements?

These research questions will be addressed one by one, supported with conclusions following from the analysis.

## 10.1. Conclusions on the research questions

### 1. *How does the dissipation of wave energy change for a change in structure width, orientation, configuration or wave condition?*

An increase in structure width causes an increase in energy dissipation. However, the relationship between energy dissipation and structure width is non-linear, with most energy dissipation taking place in the first half of the structure. This non-linearity is strongest for the horizontal orientation, with only a small increase in energy dissipation for increasing width. Based on the required amount of dissipation, a design for the structure width can be made.

When changing the orientation of the model from vertical to horizontal, the amount of energy dissipation increases, as energy is dissipated by both vertical and horizontal drag forces. The effect is strongest for wave periods around  $T = 1.0s$  and decreases with increasing wave period. In relation to the field conditions (3-5s waves), using a horizontal orientation does not have an added value in terms of additional energy dissipation, as the effect on energy dissipation decreases with increasing wave period.

If the uniform open configuration is taken as the reference case (see Figure 5.2), adding more elements to it to obtain the uniform dense, longitudinal and staggered configuration causes an increase in the total amount of energy dissipation because of the increase in the number of elements (for both vertical and horizontal orientation). However, in terms of the amount of dissipation per element, the measure is only effective for the longitudinal configuration. For the uniform dense and staggered configuration, the extra elements create sheltering which decreases the amount of dissipation per element. In the longitudinal configuration, the distance is larger, reducing this effect. Considering both the total energy dissipation and the energy dissipation per element, the longitudinal configuration is the most effective one.

With respect to the effect of the wave period, larger periods cause in general a decrease in wave energy dissipation. The ratio of wavelength to structure width becomes larger, which reduces the effect of the structure on the wave. Also the excursion length becomes longer, resulting in a more streamlined flow between the elements as shown in Figure 9.5b.

So, based on the measurements with the wave conditions applied in this research, the longitudinal configuration with a horizontal orientation is the most effective when considering both the total amount of dissipation and the dissipation per element. However, when taking into account the wave conditions in the field, the increase in dissipation for the horizontal orientation is only marginal. As the horizontal elements also require more maintenance, the longitudinal configuration with vertical orientation is considered to be the best solution.

### 2. *What is the influence of element diameter on wave energy dissipation?*

To assess the effect of a change in element diameter, a comparison is made between the results of Haage (2018) and the results of this research. A simplified drag coefficient was plotted against  $KC^*$ , which is based on the ratio of the excursion length to the element spacing. From the analysis of the drag coefficients for the 2cm and 4cm model, no direct effect of the diameter is observed. The values for both models overlap and show the same trend, with large  $C_d$  values for low  $KC^*$ -values and a decrease for increasing  $KC^*$ . However, a larger diameter results in smaller  $KC^*$ -values when the same wave conditions are applied, which results in higher drag coefficients.

3. *What is the relative importance of the physical processes causing the wave dissipation?*

During this study, the focus was on the distinction between an increase in drag coefficient and an increase in velocity inside the structure. From the velocity measurements, it is concluded that the velocity inside the structure increases significantly. This makes that the theory of Dalrymple, which determines the drag coefficient based on the assumption of linear wave theory, is not valid for the present application. The assumption underestimates the velocity, which will lead to values of the drag coefficient that are too high.

The amplification factors for the velocities obtained from the measurements were compared with velocity parameterizations from literature. For the velocity inside the model, the amplification factor based on the porosity of the structure serves as a lower limit. From the measurements with waves and the measurements with currents, the factor based on the frontal porosity is found to be an upper limit for the velocities.

To understand the processes causing the differences in energy dissipation, two methods were adopted, based on two different principles. Method 1 is based on a constant pair of coefficients, assuming that the differences are due to a difference in velocity inside the model. Method 2 is based on a constant velocity adopted from linear wave theory and assumes that the differences are due to an increase in force coefficients.

From the analysis of method 1, it is concluded that the increase in velocity is a key component in the determination of the force signal and energy dissipation. The assumption of a constant pair of coefficients and an amplification factor for the velocity resulted in a good prediction of the energy dissipation and a reasonable prediction of the forces. From this can be concluded that the drag coefficient for an element in an array of cylinders is close to the value of a single cylinder and that higher values are due to wrong assumptions of the velocities inside the array.

The calibration of the force coefficients is method 2 resulted in a good prediction of the force signal. However, using these coefficients to predict the energy dissipation was not possible, as it lead to a large spread in results. A possible explanation can be found in the calibration procedure, which is explained in Section 9.2. From this can be concluded that the increase in force coefficients does not represent what happens in reality.

The sub-question then leads to two extra questions.

*(a) How does the relative importance of the processes change for different wave conditions?*

The calibrated amplification factor for the linear theory showed a constant value for the different waves conditions, with only an increase for the 2-seconds wave. However, when the undisturbed velocity was used, this increase was not seen, suggesting a constant value over the wave conditions. The increase could be due to wave non-linearity, which shows that is it important to take this into account.

For the higher velocities, which are caused by the longer waves, the difference between the calculated velocity and the measured velocity became larger. As the velocities are measured in the jet between the elements, it can be concluded that a more streamlined flow is generated between the elements, causing the elements to be sheltered (See Section 9.2 in the Discussion). This effect is larger for the longer waves.

*(b) How do those processes change for different configurations?*

In this research, an elaborate study has been done on the longitudinal and uniform dense configuration. Both configurations showed an increase in velocity inside the structure. The trend of the increase over the different wave conditions was similar for both arrangements, although larger for the longitudinal configuration. The larger velocities resulted in the fact

that longitudinal configuration produces approximately the same amount of energy dissipation as the uniform configuration, with less elements. It can be concluded that both frontal and structure porosity play a role in the amplification of the velocity and therefore in the amount of dissipation.

## 10.2. Recommendations for further research

Following from the results and problems encountered in this research, a number of recommendations are made for further research for both the experiments and the calculation model.

### Experiments

The present study compares the results of Haage (2018) on a 2cm model and the results on a 4cm model, to study the effect of the diameter. However, due to a change in porosity it is not possible to make a direct comparison, as discussed in Section 9.2. To verify the conclusions in this research, it is recommended to perform tests on 2 models with the same porosity, but a different diameter.

Based on the results of the energy dissipation, it is concluded that the placement of the elements in rows perpendicular to the direction of wave propagation is the most effective in terms of total dissipation and dissipation per element. In the experiments a single value of 12cm is used for the heart-to-heart distance of the rows, with a constant incoming wave height of 13cm. This resulted in a variation in the amount of dissipation over the different wave periods/ lengths. To study the relation between amount of dissipation and the distance of the rows, it is recommended to gradually increase the heart-to-heart distance of the rows ( $L/d$  in Figure 9.3a) for different wave lengths/ heights. At the same time, these measurements can be used to study the relation between the velocity increase and the ratio of frontal porosity to structure porosity, as it was concluded that the amplification factor is dependent on both porosities.

For the longer waves and for uniform flow, the amplification factor for the velocity tends towards a factor based on the frontal porosity  $n_f$ . To study the relationship between the velocity increase and  $n_f$ , it is recommended to also apply a gradual increase in lateral distance ( $T/d$  in Figure 9.3a). An advantage of this is also that by applying a larger lateral distance, the velocity measurement can be done in between the elements in lateral direction, resulting in a symmetric velocity signal. This can be used for a better study of the force-velocity relation.

As discussed in Section 9.2, Nepf (1999) assumes a that the drag coefficient becomes lower when an element is sheltered. In this research, it is assumed that the drag coefficient stays close to 1.0 and that the experienced velocity by the element is lower than the velocity between the elements. To study the sheltering effect better, it is recommended to used flow visualization techniques (like Particle Image Velocimetry, PIV) to study the velocity field around an element and link this to the force signal.

From the point of view of present work, the longitudinal configuration seems to be a promising solution. However, the focus was purely on the amount of energy dissipation, neglecting other effects that might play a role in restoration of the mangrove forests. Also, as the velocities increase in the structure, so do the velocities at the bottom. This might lead to scour between the elements, causing instability of the structure. It is therefore recommended to investigate the effect of the structure in a broader perspective, including the effects it might have on the bottom and sediment transport.

**Energy dissipation model**

In the calculations, the velocity inside the model is linked to the measured transmitted wave height for 4 structure widths, as discussed in Section 9.2. This approach neglects local effects that can happen inside the structure, such as set-up and interaction with a reflected wave component. It is recommended to study the wave height decay inside the structure better by analyzing the video recordings made from the side view. Also the use of the mentioned flow visualisation techniques to analyse the flow field inside the model can help to improve/verify the assumptions made for the velocity based on the wave height.

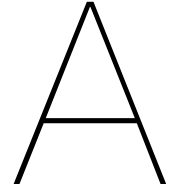
In the calculations and analysis in current work, all the results that are used are on the model scale. To make a link with the field conditions, it is recommended to scale the results to prototype scale.



# Bibliography

- Bokaian, A. and Geoola, F. (1984). Wake-induced galloping of two interfering circular cylinders. *Journal of Fluid Mechanics*, 146:383–415.
- Borgman, L. (1972). Statistical Models for Ocean Waves and Wave Forces. *advances in Hydrosience*, 8:139–181.
- Bosboom, J. and Stive, M. J. (2015). *Coastal dynamics I*. Delft Academic Press, Delft.
- Bradley, K. and Houser, C. (2009). Relative velocity of seagrass blades : Implications for wave attenuation in low-energy environments. *Journal of geophysical research*, 114(August 2008):1–13.
- Brielle, A. C. (2014). Assessment of the application of permeable pile groins as coastal protection. MSc Thesis, Delft University of Technology.
- Chaplin, J. R. (1988). Loading on a cylinder in uniform oscillatory flow : Part II - Elliptical orbital flow. *Applied Ocean Research*, 10(3):120–128.
- Chen, H., Ni, Y., Li, Y., Liu, F., Ou, S., Su, M., and Peng, Y. (2018). Deriving vegetation drag coefficients in combined wave-current flows by calibration and direct measurement methods. *Advances in Water Resources*, 122(135):217–227.
- Dalrymple, R. a., Kirby, J. T., and Hwang, P. A. (1984). Wave Diffraction Due To Areas of energy dissipation. *Journal of Waterway, Port, Coastal, and Ocean Engineering*, 110(1):67–79.
- Ecoshape (2015). Building with nature Indonesia (securing eroding delta coastlines): Design and engineering plan. Technical report.
- Etminan, V., Lowe, R. J., and Ghisalberti, M. (2019). Canopy resistance on oscillatory flows. *Coastal Engineering*, 152.
- FAO (2008). The world's mangroves 1980-2005. *FAO Forestry Paper 153*, page 89.
- Giri, C., Ochieng, E., Tieszen, L. L., Zhu, Z., Singh, A., Loveland, T., Masek, J., and Duke, N. (2011). Status and distribution of mangrove forests of the world using earth observation satellite data. *Global Ecology and Biogeography*, 20:154–159.
- Graham, J. (1980). The forces on sharp-edged cylinders in oscillatory flow at low Keulegan-Carpenter numbers. *Journal of Fluid Mechanics, part 1*, 97:331–346.
- Haage, S. S. (2018). Wave Flume Experiments on Permeable Structures. MSc Thesis, Delft University of Technology.
- Holthuijsen, L. H. (2007). *Waves in oceanic and coastal waters*. Cambridge University Press, Cambridge.
- Hu, Z., Suzuki, T., Zitman, T., Uittewaal, W., and Stive, M. (2014). Laboratory study on wave dissipation by vegetation in combined current-wave flow. *Coastal Engineering*, 88:131–142.
- Huang, Z., Yao, Y., Sim, S. Y., and Yao, Y. (2011). Interaction of solitary waves with emergent, rigid vegetation. *Ocean Engineering*, 38(10):1080–1088.
- Hudspeth, R., Nath, J., and Khare, P. (1988). Wave phase/ amplitude effects on force coefficients. *Journal of Waterway, Port, Coastal, and Ocean Engineering*, 114(1):34–49.

- Isaacson, M., Subbiah, K., and Baldwin, J. (1991). Force coefficient estimation from random wave data. *International Journal of Offshore and Polar Engineering*, 1(4):11–16.
- Jadhav, R. S., Chen, Q., and Smith, J. M. (2013). Spectral distribution of wave energy dissipation by salt marsh vegetation. *Coastal Engineering*, 77:99–107.
- Justesen, P. (1989). Hydrodynamic forces on large cylinders in oscillatory flow. *Journal of Waterway, Port, Coastal, and Ocean Engineering*, 115(4):497–514.
- Li, Y. and Lin, M. (2010). Hydrodynamic coefficients induced by waves and currents for submerged circular cylinder. *Procedia Engineering*, 4:253–261.
- Losada, I. J., Maza, M., and Lara, J. L. (2016). A new formulation for vegetation-induced damping under combined waves and currents. *Coastal Engineering*, 107:1–13.
- McIvor, A. L., Spencer, T., Möller, I., and Spalding, M. (2013). The response of mangrove soil surface elevation to sea level rise. *The Nature Conservancy ...*, page 59.
- Mendez, F. J. and Losada, I. J. (2004). An empirical model to estimate the propagation of random breaking and nonbreaking waves over vegetation fields. *Coastal Engineering*, 51(2):103–118.
- Morison, J., O'Brien, M., Johnson, J., and Schaaf, S. (1950). The Force Exerted by Surface Waves on Piles. *Journal of Petroleum Technology*, 2(05):149–154.
- Nepf, H. M. (1999). Drag, Turbulence, and Diffusion in Flow Through Emergent Vegetation. *Water Resources Research*, 35(2):479–489.
- Nepf, H. M. (2011). Flow Over and Through Biota. In *Treatise on Estuarine and Coastal Science*, volume 2, pages 267–288.
- NOAA (2017). Mangrove forests. Retrieved 30-10-2018 from <https://www.noaa.gov/>.
- Ozeren, Y., Asce, A. M., Wren, D. G., Asce, M., Wu, W., and Asce, M. (2014). Experimental Investigation of Wave Attenuation through Model and Live Vegetation. *Journal of Waterway, Port, Coastal, and Ocean Engineering*, 140(5):1–12.
- Pujol, D., Serra, T., Colomer, J., and Casamitjana, X. (2013). Flow structure in canopy models dominated by progressive waves. *Journal of Hydrology*, 486:281–292.
- Schriereck, G. J. (2001). *Introduction to bed, bank and shore protection*. Delft Academic Press, Delft.
- Singha, A. and Balachandar, R. (2011). Structure of wake of a sharp-edged bluff body in a shallow channel flow. *Journal of Fluids and Structures*, 27(2):233–249.
- Stone, B. M. and Shen, H. T. (2002). Hydraulic Resistance of Flow in Channels with Cylindrical Roughness. *Journal of Hydraulic engineering*, 128(5):500–506.
- Sumer, B. M. and Fredsoe, J. (2006). *Hydrodynamics Around cylindrical structures*, volume 26. World Scientific Publishing Co. Pte. Ltd.
- Suzuki, T., Hu, Z., Kumada, K., Phan, L. K., and Zijlema, M. (2019). Non-hydrostatic modeling of drag, inertia and porous effects in wave propagation over dense vegetation fields. *Coastal Engineering*, 149(135):49–64.
- Williamson, C. (1985). Sinusoidal flow relative to circular cylinders. *Journal of Fluid Mechanics*, 155:141–174.
- Winterwerp, J. C., Erftemeijer, P. L. A., Suryadiputra, N., Van Eijk, P., and Zhang, L. (2013). Defining eco-morphodynamic requirements for rehabilitating eroding mangrove-mud coasts. *Wetlands*, 33(3):515–526.
- Zhang, H. and Qi, X. (2016). Heat transfer analysis and modification of thermal probe for gas-solid measurement. *Mathematical Problems in Engineering*, 2016.



## Method of Goda and Suzuki (1976)

The method described is developed by Goda and Suzuki (1976). Based on this method, a Matlab program is written by Klaasman in 2005 for the Environmental Fluid Mechanics laboratory at Delft University of Technology. The program calculates the incoming and reflected wave heights based on the data of two wave gauges. For a regular wave with wave gauges at location  $x = x_1$  and  $x = x_2$ , the basic equations are given by:

$$\eta(x_1, t) = \sum_{n=1}^N a_{i,n} \cos(k_n x_1 - \omega_n t + \phi_{i,n}) + \sum_{n=1}^N a_{r,n} \cos(k_n x_1 + \omega_n t + \phi_{r,n}) \quad (\text{A.1})$$

$$\eta(x_2, t) = \sum_{n=1}^N a_{i,n} \cos(k_n x_2 - \omega_n t + \phi_{i,n}) + \sum_{n=1}^N a_{r,n} \cos(k_n x_2 + \omega_n t + \phi_{r,n}) \quad (\text{A.2})$$

in which:

- $\eta$  - Elevation of the water surface relative to the mean water level
- $t$  - Time
- $a_{i,n}, a_{r,n}$  - Wave amplitude of the incoming and reflected wave of the n-th harmonic
- $k_n$  - Wave number of the n-th harmonic
- $\omega_n$  - Angular frequency of the n-th harmonic
- $\phi_{i,n}, \phi_{r,n}$  - Phase of the incoming and reflected wave of the n-th harmonic

The Refreg program only takes into account the first harmonic, which simplifies equation A.1 and A.2:

$$\eta(x_1, t) = a_i \cos(kx_1 - \omega t + \phi_i) + a_r \cos(kx_1 + \omega t + \phi_r) \quad (\text{A.3})$$

$$\eta(x_2, t) = a_i \cos(kx_2 - \omega t + \phi_i) + a_r \cos(kx_2 + \omega t + \phi_r) \quad (\text{A.4})$$

Equation A.3 can then be rewritten as:

$$\eta(x_1, t) = a_i \{ \cos(kx_1 + \phi_i) \cos(\omega t) + \sin(kx_1 + \phi_i) \sin(\omega t) \} + a_r \{ \cos(kx_1 + \phi_r) \cos(\omega t) - \sin(kx_1 + \phi_r) \sin(\omega t) \} \quad (\text{A.5})$$

or even simpler:

$$\eta(x_1, t) = A_1 \cos(\omega t) + B_1 \sin(\omega t) \quad (\text{A.6})$$

In the same way, equation A.4 can be rewritten as:

$$\eta(x_2, t) = A_2 \cos(\omega t) + B_2 \sin(\omega t) \quad (\text{A.7})$$

With in these equations:

$$A_1 = a_i \cos(kx_1 + \phi_i) + a_r \cos(kx_1 + \phi_r) \quad (\text{A.8})$$

$$B_1 = a_i \sin(kx_1 + \phi_i) - a_r \sin(kx_1 + \phi_r) \quad (\text{A.9})$$

$$A_2 = a_i \cos(kx_2 + \phi_i) + a_r \cos(kx_2 + \phi_r) \quad (\text{A.10})$$

$$B_2 = a_i \sin(kx_2 + \phi_i) - a_r \sin(kx_2 + \phi_r) \quad (\text{A.11})$$

Combining Equation A.8 - A.11 gives the following complex equations:

$$A_1 + iB_1 = a_i e^{ik_1} e^{i\phi_i} + a_r e^{-ik_1} e^{-i\phi_r} \quad (\text{A.12})$$

$$A_2 + iB_2 = a_i e^{ik_2} e^{i\phi_i} + a_r e^{-ik_2} e^{-i\phi_r} \quad (\text{A.13})$$

where  $i = \sqrt{-1}$ .

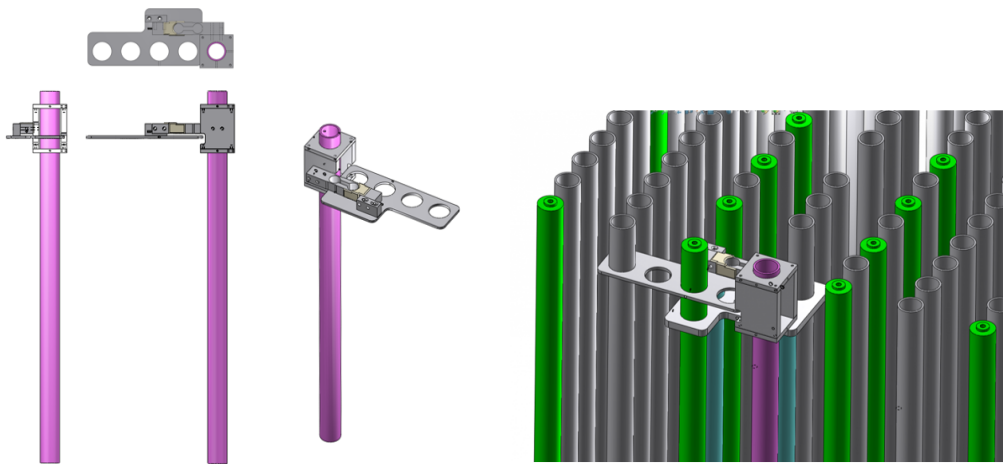
Or in matrix form:

$$\begin{pmatrix} e^{ik_1} & e^{-ik_1} \\ e^{ik_2} & e^{-ik_2} \end{pmatrix} \begin{pmatrix} a_i e^{i\phi_i} \\ a_r e^{-i\phi_r} \end{pmatrix} = \begin{pmatrix} A_1 + iB_1 \\ A_2 + iB_2 \end{pmatrix}$$

Using a Fast Fourier Transformation (FFT), the coefficients  $A$  and  $B$  can be obtained by a harmonic analysis of the water surface. The length of the series to be analyzed is determined by one zero crossing at the beginning and one zero crossing at the end of the first data series, both of the same sign. The FFT function in Matlab is then used on the data series of the two wave gauges. The base period is found by the period with the maximum modulus of the Fast Fourier Transformation.

## Instrument specifications

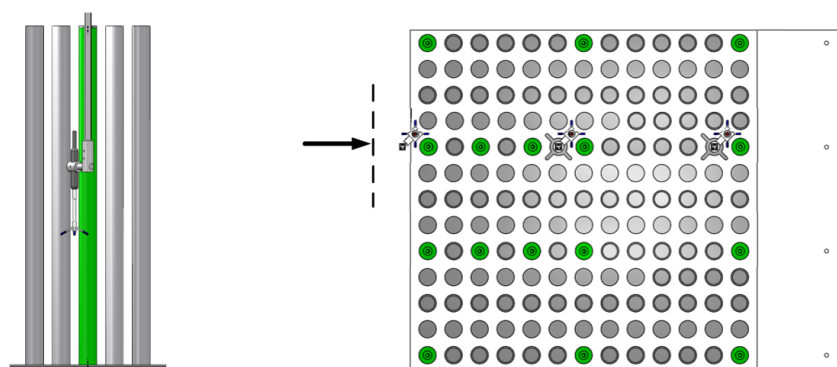
### B.1. Framework FT and ADV



(a) Different view of the force transducer.

(b) The force transducer placed in the model.

Figure B.1: Framework to place the force transducer in the model.



(a) Side view of the ADV in the model.

(b) Top view of the ADV placed at the three measurement locations

Figure B.2: Framework to place the ADV in the model.

## B.2. Wave gauges (WG)

### 4. Specifications.

#### a. Probe.

Level-electrodes : rods, stainless steel, type 316,  
 4 mm. diam., electrode spacing 23 mm,  
 electrode length 59 cm.  
 Ref. electrode : platinum, 5 x 2 mm diam..  
 Non-linearity : 0.5% of selected range, b.s.l..  
 Liquid medium : all liquids compatible with above-  
 mentioned materials.  
 Conductivity-  
 influence : - minimum required conductivity 0.08 mS  
 - sensitivity change <1% for variations  
 between 0.1 and 2 mS.  
 Dimensions : incl. electronics 70 x 8 x 9 cm.  
 Weight : 0.7 kg.  
 in container (12 x 73 x 14 cm), 3 kg.  
 Output : 0.05 VDC/cm level-variation.  
 Power : +/- 15 VDC, +/- 100 mA.

#### b. Control-unit.

Input : 0.05 VDC/cm.  
 (+/- 15 VDC for probe electronics is  
 supplied via input-connector.).  
 Ranges : 5, 10, 20 and 50 cm.  
 Output-shift : between + and - 10 VDC, within the  
 limits of the standard output-voltage.  
 Freq. response : 0 to 10 Hz.  
 Output : +/- 10 VDC, 2 mA max. for the range  
 selected.  
 Power : 220 VAC, 50-60 Hz., 20 VA, incl. probe.  
 Dimensions : portable case, 26 x 15 x 32 cm,  
 (for 2 plug-in units Euro-frame)  
 Weight : portable case 5 kg  
 nett shipping weight per set 10 kg.

## B.3. Acoustic doppler velocimeter (ADV)

### Technical Specifications

#### Water Velocity Measurements

Range:	$\pm 0.01, 0.1, 0.3, 1, 2, 4 \text{ m/s}^*$ (user selectable)
Accuracy:	$\pm 1\%$ of measured value $\pm 1 \text{ mm/s}$
Sampling rate (output):	1–25 Hz (standard firmware), 1–200 Hz (Plus firmware)

\*) The velocity range is not the same in the horizontal and vertical direction. Please refer to the configuration software.

#### Sampling Volume

Distance from probe:	0.05 m
Diameter:	6 mm
Height (user selectable):	3–15 mm

#### Echo Intensity

Acoustic frequency:	10 MHz
Resolution:	Linear scale
Dynamic range:	25 dB

#### Sensors

Temperature:	Thermistor embedded in probe
Range:	$-4^{\circ}\text{C}$ to $32^{\circ}\text{C}$
Accuracy/Resolution:	$1^{\circ}\text{C}/0.1^{\circ}\text{C}$ 5
Time response:	min

#### Data Communication

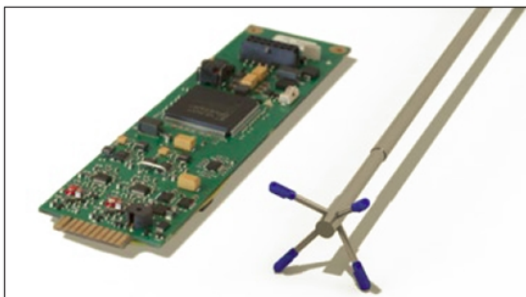
I/O:	RS 232. The software supports most commercially available USB–RS 232 converters.
Communication Baud rate:	300–115 200 Baud
User control:	Handled via Vectrino Win32* software, ActiveX* function calls, or direct commands.
Analog outputs:	3 channels standard, one for each velocity component.
Output range:	0–5 V, scaling is user selectable.
Synchronization:	SynchIn and SynchOut

#### Multi Unit Operation

Software:	Polysync
I/O:	RS 232–USB support for devices with 1, 2, 4, and 8 serial ports.

#### Software ("Vectrino")

Operating system:	Windows* XP, Windows* 7
Functions:	Instrument configuration, data collection, data storage. Probe test modes.



The Vectrino consists of two basic elements: the probe attached to a cylindrical housing and the processor inside the housing. From here the processed data is sent over a serial line or analog signals can be sent to an A/D converter.

#### Power

DC Input:	12–48 VDC
Peak current:	2.5 A at 12 VDC (user selectable)
Max. consumption:	200 Hz 1.5 W

#### Connectors

Bulkhead:	MCBH-12-FS, bronze (Impulse)
Cable:	PMCIL-12-MP – see also options below.

#### Materials

Standard model:	Delrin* housing, Stainless steel (316) probe and screws.
-----------------	--

#### Environmental

Operating temperature:	$-4^{\circ}\text{C}$ to $40^{\circ}\text{C}$
Storage temperature:	$-15^{\circ}\text{C}$ to $60^{\circ}\text{C}$
Shock and vibration:	IEC 721-3-2

#### Dimensions

See drawings on page 2-3 for dimensions

Weight in air:	1.2 kg
Weight in water:	Neutral

#### Options

- Standard or Vectrino Plus firmware
- 4-beam down-looking probe or side-looking probe. Fixed stem or flexible cable
- 10, 20, 30 or 50 m cable with Impulse underwater connector
- RS 232–USB converter (one-to-one, four-to-one or eight-to-one)
- Combined transportation and storage case





## B.5. Electromagnetic Flowmeter (EMF)

### 3. Specifications.

Unless specified, otherwise the data apply to:

- X- and Y-axis
- reference conditions  
(medium : water, 20° C.  
Conductivity 0.5 mS/cm  
ambient temp. 20° C.).

#### 3.1 Probes. (Figure 9)

- Sensors
- electromagnetic, bi-directional, 4-quadrants
  - "E" type 30 mm diam.:
    - ellipsoid, 11 x 33 mm
    - rod 10 mm diam.
    - max. immersion length 850 mm
    - electronics unit 65 x 150 x 35 mm
    - total probe length 1090 mm
    - max. pressure 3 Bar
    - cable length to control-unit  
100 m max. (std. 10 m.)
  - "E" type 40 mm diam.:
    - ellipsoid, 11 x 43 mm
    - rod 10 mm diam.
    - conn. box 35 mm diam., l = 160 mm
    - fully immersible
    - max. pressure 3 Bar
    - connector: waterproof or cable-gland
    - cable length to control-unit or if  
applied, field-box 100 m max.  
(std. 25 m.)
    - cable length field-box to control-  
unit 1000 m max. (std. 25 m)
    - Conditioning-unit 12 x 22 x 9 cm
  - "S" type :
    - sphere, diam. 40 mm
    - rod 10 mm diam.
    - conn. box 35 mm diam., l = 160 mm
    - fully immersible
    - max. pressure 3 Bar
    - connector: waterproof or cable-gland
    - cable length to control-unit or if  
applied, field-box 100 m max.  
(std. 25 m.)
    - cable length field-box to control-  
unit 1000 m max. (std. 25 m)
    - Conditioning-unit 12 x 22 x 9 cm
- Materials - materials exposed to the medium:
- Stainless steel 316
  - Ampco 45
  - Platinum
  - p.v.c.

Medium		- clean and dirty liquids, including slurries - minimum conductivity 0.2 mS/cm - max. temperature 50° C. (water)
Range	- "E"-30 type - "E"-40 type - "S" type	0 to +/- 100 cm/s 0 to +/- 250 cm/s 0 to +/- 250 cm/s

### 3.2 Control-unit (Figure 2)

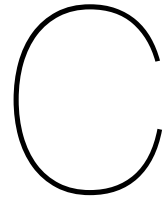
Output		- 0 to +/- 10 V for range selected, min. load 2 k $\Omega$
Dynamic response		- 1 Hz (70 %); ( 5 Hz selectable)
Range		- 0 to +/- 100 or 250 cm/s, switch selectable
Range-shift		- $\pm$ 20 % of range selected
Display		- analog meter, X or Y selectable, scale length +/- 16 mm
Dimensions (cassette)		- 106 x 127 x 210 mm (w x h x d)
Weight (complete control-unit)		- 1 kg - 300 x 170 x 380 cm (w x h x d)
Weight		- 2 kg

### 3.3 System

Accuracy	- "E" types :	$\pm$ 1 % of f.s. $\pm$ 0.5 cm/s for tilt angles between + and - 10° and $V \leq 20$ cm/s
	- "S" type :	$\pm$ 4 % of f.s. $\pm$ 0.5 cm/s + tilt response error

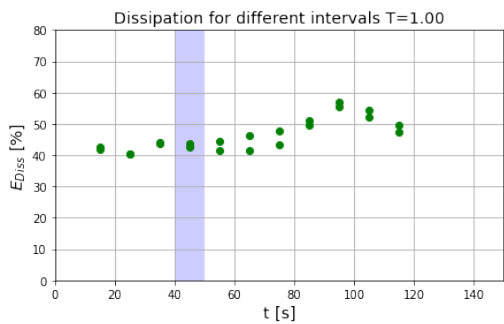
Specified accuracy applies to reference conditions and includes non-linearity and zero-stability.

Tilt response	- "S" type :	max. error $\pm$ 5% of reading for angles between + and - 30 degrees and $V \leq 30$ cm/s
---------------	--------------	---

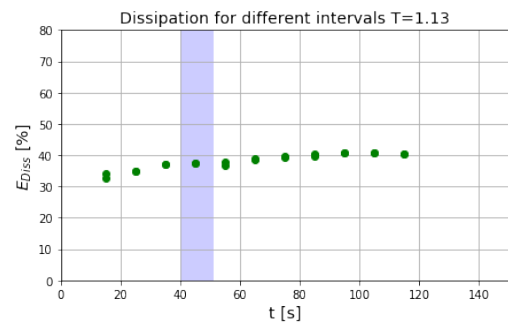


# Dissipation for different intervals

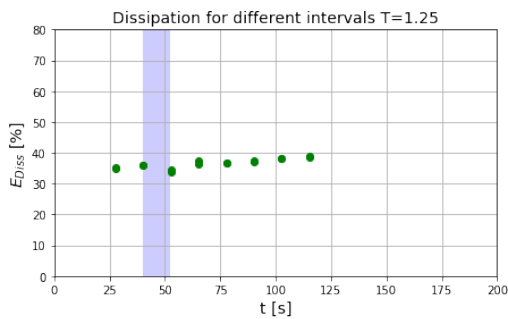
## C.1. V035L



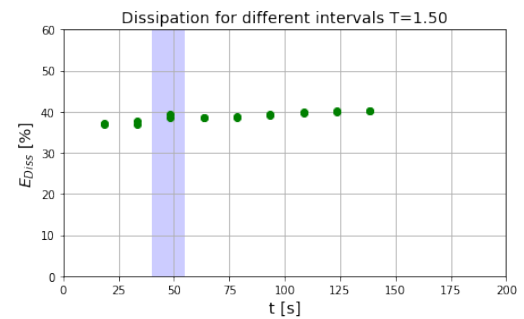
(a) 1 seconds wave period.



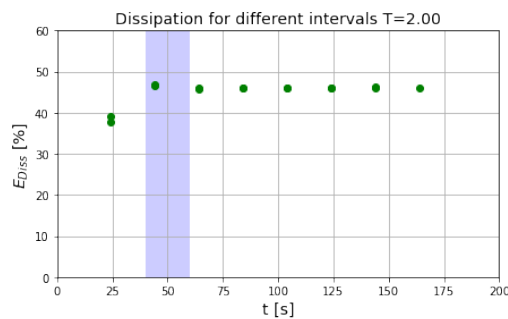
(b) 1.13 seconds wave period.



(c) 1.25 seconds wave period.



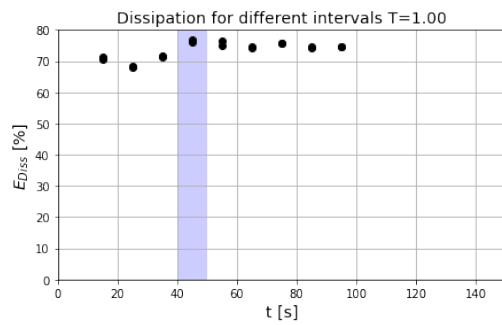
(d) 1.50 seconds wave period.



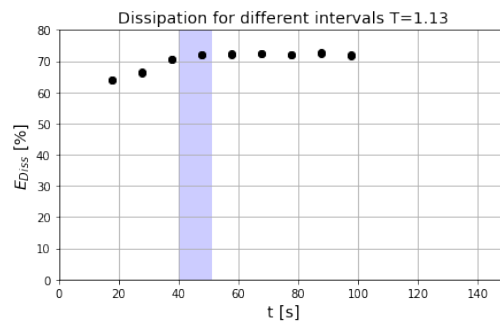
(e) 2 seconds wave period.

Figure C.1: Dissipation as a percentage of the incoming energy, calculated for successive intervals in different wave conditions. The first movement of the water surface observed by the wave gauges is at  $t = 0$  s. The interval marked in blue is the interval used for further calculations.

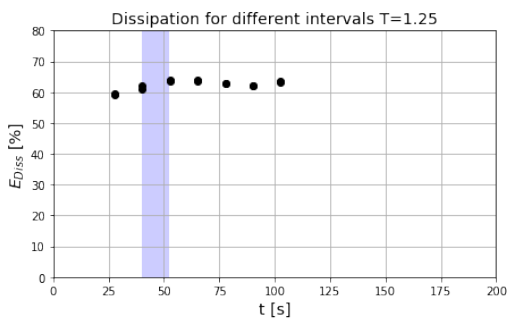
## C.2. H068L



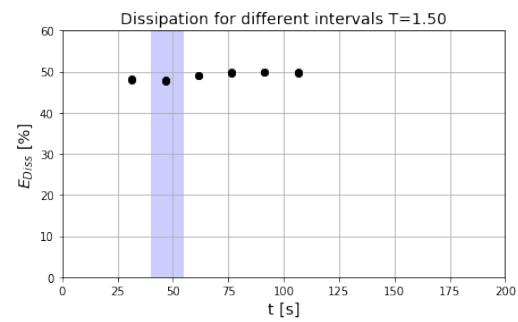
(a) 1 seconds wave period.



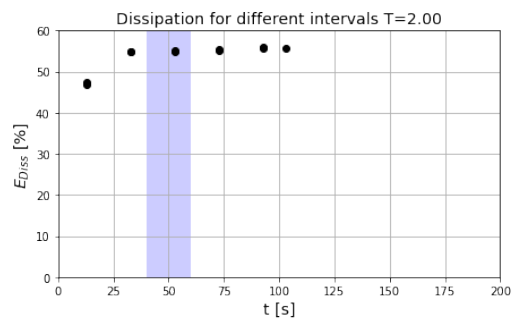
(b) 1.13 seconds wave period.



(c) 1.25 seconds wave period.



(d) 1.50 seconds wave period.



(e) 2 seconds wave period.

Figure C.2: Dissipation as a percentage of the incoming energy, calculated for successive intervals in different wave conditions. The first movement of the water surface observed by the wave gauges is at  $t = 0$ s. The interval marked in blue is the interval used for further calculations.

### C.3. ADV velocity measurements

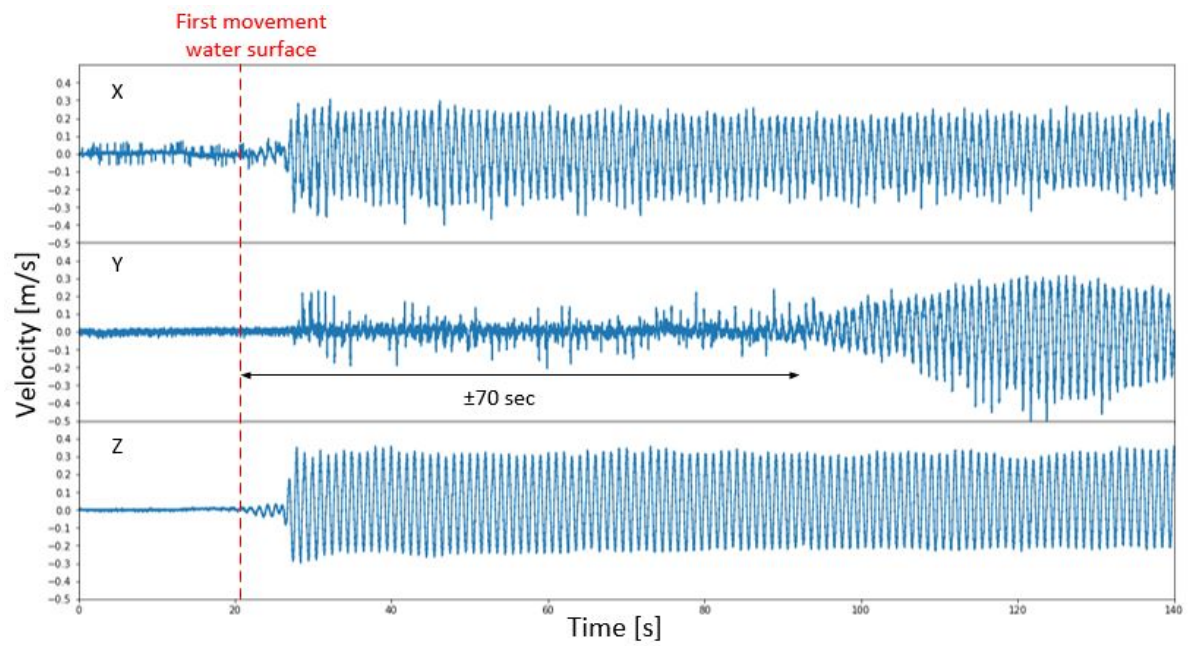
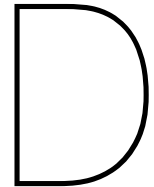


Figure C.3: Development of transverse velocity observed for a wave period of  $T = 1.00$  second.





## List of performed experiments

*This appendix presents a list of all the experiments performed during the experiments phase. The total number of experiments is larger than used in the analysis, due to time limitations in the processing of the results.*

### D.1. Experiments set 1

Table D.1: Test conditions with different combinations of configuration and wave period. Every combination from left to right forms an experiment.

Orientation	Configuration	Take	Water depth [m]	Wave height [m]	Wave period [s]
-	Empty flume				
Vertical	Uniform dense half width	1 / 2	0.60	0.13	1.00
	Uniform open half width				1.13
	Longitudinal half width				1.25
	Staggered half width				1.50
	Uniform dense full width				2.00
	Uniform open full width				3.00
	Longitudinal full width				
	Staggered full width				
	Changing density				
Horizontal	Uniform dense half width	1 / 2	0.60	0.13	1.00
	Uniform open half width				1.13
	Longitudinal half width				1.25
	Staggered half width				1.50
	Uniform dense full width				2.00
	Uniform open full width				3.00
	Longitudinal full width				
	Staggered full width				

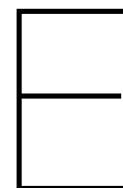
## D.2. Experiments set 2

Table D.2: Test conditions with different combinations of configuration and wave period/ current velocity. Every combination from left to right forms an experiment.

Orientation	Configuration	Location ADV/FT <sup>2</sup>	ADV height [m]	Take	Water depth [m]	Wave height [m]	Wave period [s]
-	Empty flume			1			
Vertical with waves <sup>1</sup>	1 element Open row Dense row	-	0.15/0.25/0.40	1/2	0.55	0.13	1.00
	3 rows long. 5 rows long. 5 rows dense 9 rows dense	M					1.13
	Uniform dense Uniform open Longitudinal Staggered	F/M/B					1.25
							1.50
							2.00
			3.00				
Orientation	Configuration	Location ADV/FT	ADV height [m]	Take	Water depth [m]	Wave height [m]	Velocity [m/s]
Vertical with current	1 element Open row Dense row	-	0.40	1	0.55	-	0.10
	Uniform dense Uniform open Longitudinal Staggered	M					0.20
							0.40
Orientation	Configuration	Location ADV/FT	ADV height [m]	Take	Water depth [m]	Wave height [m]	Wave period [s]
Horizontal with waves	1 element Open row Dense row	-	0.355/0.385	1/2	0.55	0.13	1.00
	Uniform open Longitudinal	M					1.13
							1.25
							1.50
							2.00
							3.00

<sup>1</sup>Video recordings from the side view available.

<sup>2</sup>F - Front row, M - Middle row, B - Back row.



## Results experiments: First set

*This appendix presents the results of the first set of experiments. The first part presents graphs with the energy balance for the reflected, dissipated and transmitted wave energy in relation to the incoming energy, followed by the numerical values in a table for each configuration. The second part contains the comparison of the different diameters.*

### E.1. Results of reflected, dissipated and transmitted energy

#### **Vertical configurations half width**

- V040U064 Uniform with  $n = 0.64$
- V040U089 Uniform with  $n = 0.89$
- V040L Longitudinal with  $n = 0.79$
- V040S Staggered with  $n = 0.82$

#### **Vertical configurations full width**

- V076U064 Uniform with  $n = 0.64$
- V076U089 Uniform with  $n = 0.89$
- V076L Longitudinal with  $n = 0.79$
- V076S Staggered with  $n = 0.82$

#### **Horizontal configurations half width**

- H040U064 Uniform with  $n = 0.64$
- H040U089 Uniform with  $n = 0.89$
- H040L Longitudinal with  $n = 0.79$
- H040S Staggered with  $n = 0.82$

#### **Horizontal configurations full width**

- H076U064 Uniform with  $n = 0.64$
- H076U089 Uniform with  $n = 0.89$
- H076L Longitudinal with  $n = 0.79$
- H076S Staggered with  $n = 0.82$

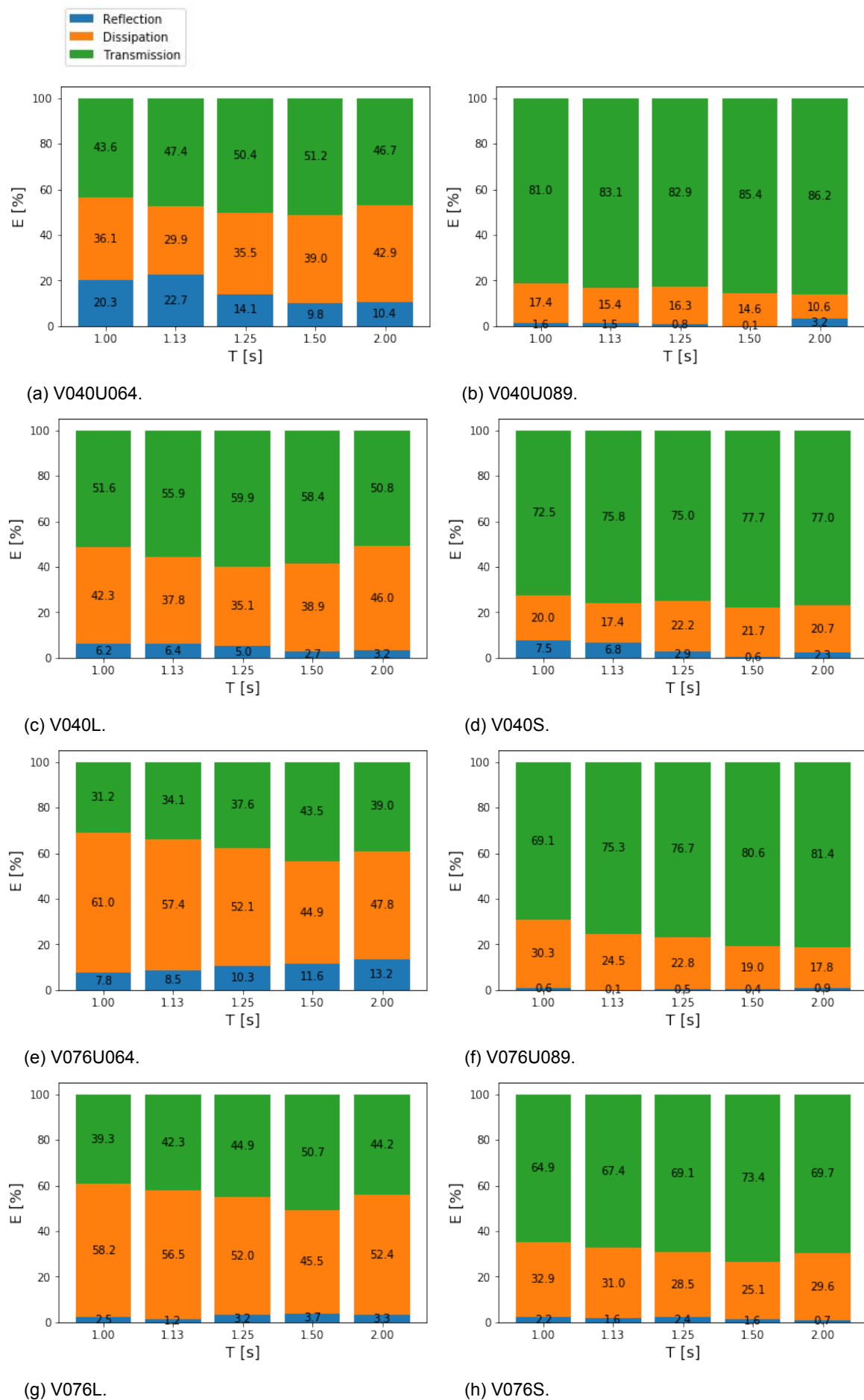


Figure E.1: Energy balance for the vertical configurations.

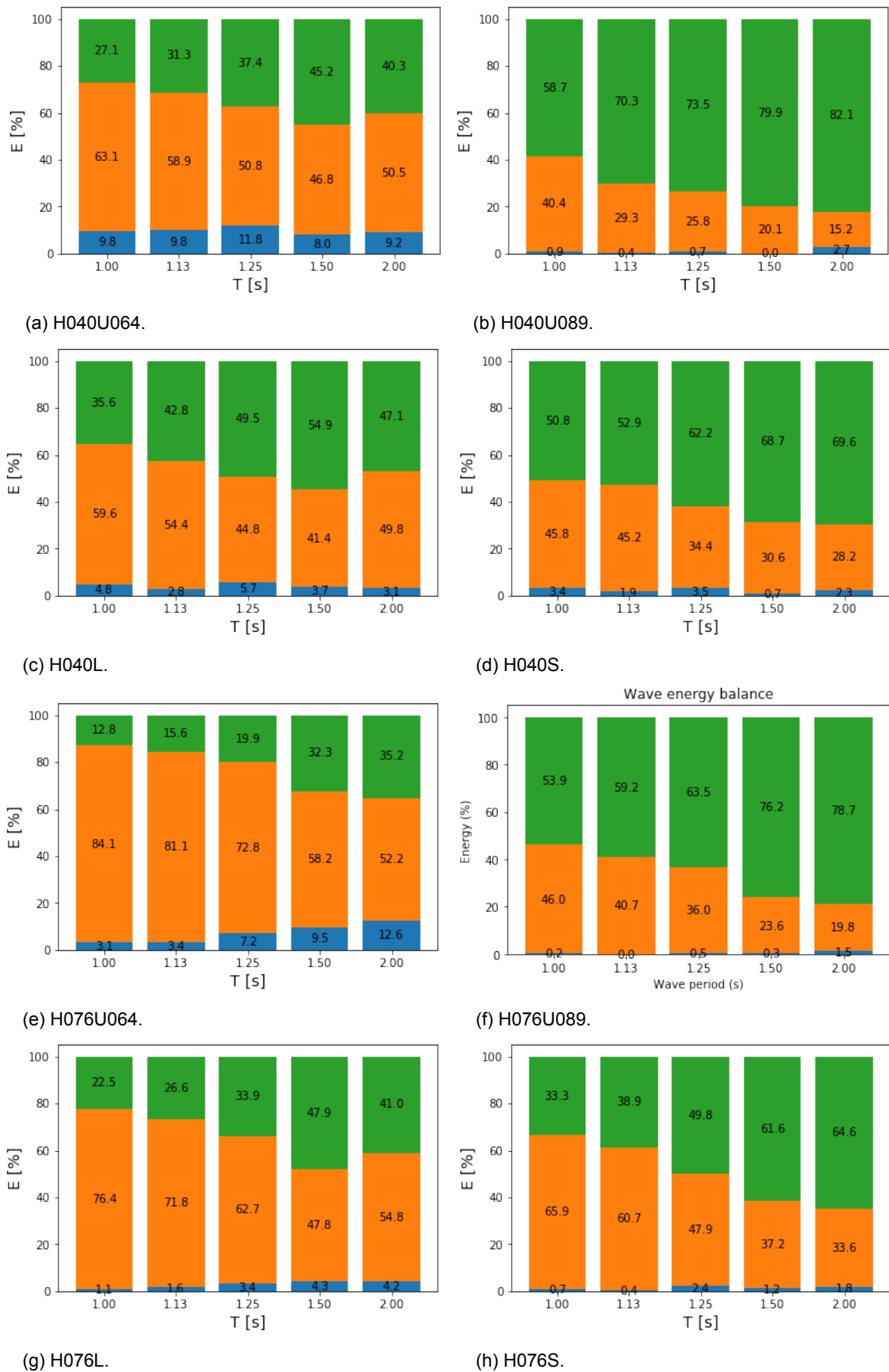


Figure E.2: Energy balance for the horizontal configurations.

Table E.1: V040U064 - Vertical uniform dense configuration, half width. n=0.64

Test	$T[s]$	$H_{in}[m]$	$H_{r1}[m]$	$H_T[m]$	$H_{r2}[m]$	$C_{r1}^2[\%]$	$C_T^2[\%]$	$C_{diss}^2[\%]$	$C_{r2}^2[\%]$
1	1.0	0.117	0.052	0.077	0.003	20.1	43.7	36.2	0.0
2	1.0	0.117	0.053	0.077	0.003	20.5	43.5	36.0	0.0
1	1.13	0.122	0.058	0.084	0.005	22.5	47.6	29.9	0.4
2	1.13	0.122	0.053	0.084	0.005	22.8	47.3	29.0	0.3
1	1.25	0.126	0.048	0.089	0.008	14.3	50.5	35.2	0.4
2	1.25	0.126	0.047	0.089	0.008	14.0	50.2	35.8	0.4
1	1.50	0.125	0.039	0.090	0.013	9.8	51.5	38.7	0.8
2	1.50	0.126	0.040	0.090	0.012	9.9	50.9	39.2	0.9
1	2.0	0.121	0.039	0.083	0.025	10.3	47.0	42.7	3.7
2	2.0	0.122	0.039	0.083	0.025	10.5	46.5	43.0	3.7

Table E.2: V040U089 - Vertical uniform open configuration, half width. n=0.89

Test	$T[s]$	$H_{in}[m]$	$H_{r1}[m]$	$H_T[m]$	$H_{r2}[m]$	$C_{r1}^2[\%]$	$C_T^2[\%]$	$C_{diss}^2[\%]$	$C_{r2}^2[\%]$
1	1.0	0.114	0.016	0.104	0.004	1.9	82.0	16.1	0.1
2	1.0	0.116	0.013	0.104	0.003	1.2	80.1	18.7	0.1
1	1.13	0.121	0.015	0.110	0.008	1.5	83.2	15.4	0.4
2	1.13	0.121	0.015	0.110	0.008	1.6	82.9	15.5	0.5
1	1.25	0.123	0.011	0.112	0.011	0.8	83.5	15.8	0.8
2	1.25	0.123	0.011	0.112	0.011	0.7	82.4	16.9	0.8
1	1.50	0.122	0.003	0.113	0.017	0.1	85.5	14.4	2.0
2	1.50	0.123	0.003	0.113	0.018	0.1	85.3	14.7	2.1
1	2.0	0.121	0.022	0.113	0.033	3.2	86.0	10.8	7.6
2	2.0	0.121	0.022	0.113	0.034	3.2	86.3	10.4	7.7

Table E.3: V040L - Vertical longitudinal configuration, half width. n=0.79

Test	$T[s]$	$H_{in}[m]$	$H_{r1}[m]$	$H_T[m]$	$H_{r2}[m]$	$C_{r1}^2[\%]$	$C_T^2[\%]$	$C_{diss}^2[\%]$	$C_{r2}^2[\%]$
1	1.0	0.117	0.030	0.084	0.005	6.6	51.7	41.7	0.2
2	1.0	0.117	0.028	0.084	0.005	5.8	51.4	42.8	0.2
1	1.13	0.123	0.031	0.092	0.008	6.4	55.8	37.8	0.5
2	1.13	0.122	0.031	0.091	0.009	6.4	55.9	37.7	0.5
1	1.25	0.122	0.027	0.095	0.008	5.0	60.0	35.1	0.5
2	1.25	0.123	0.028	0.095	0.008	5.1	59.8	35.2	0.5
1	1.50	0.123	0.021	0.094	0.014	2.8	58.7	38.5	1.3
2	1.50	0.124	0.020	0.094	0.014	2.6	58.1	39.3	1.3
1	2.0	0.122	0.022	0.087	0.026	3.2	50.8	46.1	4.6
2	2.0	0.122	0.022	0.087	0.026	3.1	50.9	46.0	4.7

Table E.4: V040S - Vertical staggered configuration, half width. n=0.82

Test	$T[s]$	$H_{in}[m]$	$H_{r1}[m]$	$H_T[m]$	$H_{r2}[m]$	$C_{r1}^2[\%]$	$C_T^2[\%]$	$C_{diss}^2[\%]$	$C_{r2}^2[\%]$
1	1.0	0.115	0.032	0.098	0.002	7.7	72.6	19.7	0.0
2	1.0	0.115	0.031	0.098	0.002	7.3	72.4	20.3	0.0
1	1.13	0.121	0.032	0.105	0.009	7.0	75.3	17.7	0.6
2	1.13	0.120	0.031	0.105	0.009	6.6	76.3	17.1	0.6
1	1.25	0.124	0.021	0.108	0.010	2.9	75.6	21.5	0.6
2	1.25	0.125	0.021	0.108	0.010	2.8	74.4	22.8	0.6
1	1.50	0.124	0.010	0.109	0.016	0.6	77.8	21.6	1.6
2	1.50	0.124	0.010	0.109	0.015	0.6	77.6	21.8	1.5
1	2.0	0.121	0.018	0.107	0.032	2.3	77.1	20.6	7.0
2	2.0	0.122	0.018	0.107	0.032	2.3	76.9	20.8	6.9

Table E.5: V076U064 - Vertical uniform dense configuration, full width. n=0.64

Test	$T[s]$	$H_{in}[m]$	$H_{r1}[m]$	$H_T[m]$	$H_{r2}[m]$	$C_{r1}^2[\%]$	$C_T^2[\%]$	$C_{diss}^2[\%]$	$C_{r2}^2[\%]$
1	1.0	0.115	0.032	0.064	0.001	7.7	31.1	61.3	0.0
2	1.0	0.115	0.032	0.064	0.002	8.0	31.3	60.8	0.0
1	1.13	0.122	0.035	0.071	0.007	8.4	34.1	57.5	0.4
2	1.13	0.121	0.036	0.071	0.007	8.6	34.1	57.3	0.3
1	1.25	0.127	0.041	0.078	0.008	10.4	37.5	52.2	0.4
2	1.25	0.126	0.040	0.078	0.008	10.2	37.8	52.0	0.4
1	1.50	0.126	0.043	0.083	0.012	11.5	43.3	45.3	0.8
2	1.50	0.125	0.043	0.083	0.012	11.7	43.8	44.5	0.9
1	2.0	0.123	0.045	0.077	0.024	13.1	39.1	47.8	3.7
2	2.0	0.123	0.045	0.077	0.024	13.3	38.9	47.7	3.7

Table E.6: V076U089 - Vertical uniform open configuration, full width. n=0.89

Test	$T[s]$	$H_{in}[m]$	$H_{r1}[m]$	$H_T[m]$	$H_{r2}[m]$	$C_{r1}^2[\%]$	$C_T^2[\%]$	$C_{diss}^2[\%]$	$C_{r2}^2[\%]$
1	1.0	0.120	0.010	0.100	0.001	0.7	69.5	29.8	0.0
2	1.0	0.120	0.009	0.100	0.001	0.6	68.7	30.8	0.0
1	1.13	0.122	0.005	0.106	0.008	0.1	76.0	23.9	0.4
2	1.13	0.122	0.004	0.106	0.008	0.1	74.7	25.2	0.4
1	1.25	0.124	0.009	0.109	0.011	0.5	76.7	22.8	0.8
2	1.25	0.124	0.009	0.109	0.011	0.5	76.7	22.8	0.8
1	1.50	0.124	0.007	0.111	0.016	0.4	80.4	19.2	1.7
2	1.50	0.124	0.008	0.112	0.016	0.4	80.7	18.9	1.7
1	2.0	0.123	0.012	0.111	0.033	0.9	81.2	17.9	7.0
2	2.0	0.123	0.012	0.111	0.033	0.9	81.5	17.6	7.0

Table E.7: V076L - Vertical longitudinal configuration, full width. n=0.79

Test	$T[s]$	$H_{in}[m]$	$H_{r1}[m]$	$H_T[m]$	$H_{r2}[m]$	$C_{r1}^2[\%]$	$C_T^2[\%]$	$C_{diss}^2[\%]$	$C_{r2}^2[\%]$
1	1.0	0.116	0.018	0.073	0.001	2.4	39.5	58.2	0.0
2	1.0	0.116	0.019	0.073	0.002	2.6	39.1	58.3	0.0
1	1.13	0.121	0.014	0.079	0.007	1.3	42.5	56.2	0.4
2	1.13	0.121	0.013	0.079	0.007	1.2	42.1	56.7	0.4
1	1.25	0.125	0.022	0.084	0.008	3.2	44.9	51.9	0.5
2	1.25	0.125	0.022	0.084	0.009	3.1	44.8	52.1	0.5
1	1.50	0.125	0.024	0.089	0.013	3.7	50.6	45.8	1.1
2	1.50	0.124	0.024	0.089	0.013	3.8	50.9	45.3	1.1
1	2.0	0.124	0.023	0.082	0.025	3.4	44.3	52.3	4.0
2	2.0	0.124	0.023	0.082	0.025	3.3	44.2	52.5	4.0

Table E.8: V076S - Vertical staggered configuration, full width. n=0.82

Test	$T[s]$	$H_{in}[m]$	$H_{r1}[m]$	$H_T[m]$	$H_{r2}[m]$	$C_{r1}^2[\%]$	$C_T^2[\%]$	$C_{diss}^2[\%]$	$C_{r2}^2[\%]$
1	1.0	0.115	0.017	0.092	0.001	2.1	65.0	32.9	0.0
2	1.0	0.115	0.017	0.092	0.001	2.3	64.7	33.0	0.0
1	1.13	0.122	0.016	0.100	0.007	1.6	67.4	31.0	0.4
2	1.13	0.121	0.015	0.099	0.008	1.6	67.5	30.9	0.4
1	1.25	0.125	0.019	0.104	0.011	2.3	69.1	28.6	0.8
2	1.25	0.124	0.020	0.103	0.011	2.5	69.0	28.5	0.7
1	1.50	0.125	0.015	0.107	0.016	1.5	73.7	24.7	1.6
2	1.50	0.125	0.016	0.107	0.016	1.6	73.0	25.4	1.6
1	2.0	0.124	0.010	0.104	0.030	0.7	69.6	29.7	5.9
2	2.0	0.124	0.010	0.104	0.030	0.7	69.9	29.5	5.9

Table E.9: H040U064 - Horizontal uniform dense configuration, half width. n=0.64

Test	$T[s]$	$H_{in}[m]$	$H_{r1}[m]$	$H_T[m]$	$H_{r2}[m]$	$C_{r1}^2[\%]$	$C_T^2[\%]$	$C_{diss}^2[\%]$	$C_{r2}^2[\%]$
1	1.0	0.119	0.038	0.062	0.000	10.4	27.0	62.7	0.0
2	1.0	0.118	0.036	0.062	0.000	9.2	27.2	63.6	0.0
1	1.13	0.126	0.039	0.070	0.007	9.8	31.2	59.0	0.3
2	1.13	0.125	0.039	0.070	0.008	9.8	31.3	58.9	0.4
1	1.25	0.126	0.043	0.077	0.011	12.0	37.4	50.7	0.7
2	1.25	0.126	0.043	0.077	0.011	11.7	37.4	51.0	0.7
1	1.50	0.125	0.035	0.084	0.013	8.0	45.0	47.0	1.1
2	1.50	0.125	0.035	0.084	0.013	8.1	45.3	46.6	1.1
1	2.0	0.122	0.037	0.078	0.025	9.1	40.4	50.5	4.0
2	2.0	0.123	0.037	0.078	0.024	9.3	40.3	50.5	4.0

Table E.10: H040U089 - Horizontal uniform open configuration, half width. n=0.89

Test	$T[s]$	$H_{in}[m]$	$H_{r1}[m]$	$H_T[m]$	$H_{r2}[m]$	$C_{r1}^2[\%]$	$C_T^2[\%]$	$C_{diss}^2[\%]$	$C_{r2}^2[\%]$
1	1.0	0.125	0.012	0.095	0.002	0.9	58.4	40.7	0.0
2	1.0	0.124	0.012	0.095	0.001	1.0	59.0	40.0	0.0
1	1.13	0.123	0.008	0.103	0.008	0.4	69.8	29.8	0.5
2	1.13	0.122	0.008	0.103	0.008	0.4	70.7	28.9	0.5
1	1.25	0.123	0.011	0.107	0.009	0.7	74.6	24.6	0.6
2	1.25	0.126	0.010	0.117	0.010	0.7	72.3	27.0	0.6
1	1.50	0.122	0.003	0.109	0.015	0.1	80.2	19.8	1.5
2	1.50	0.122	0.003	0.109	0.015	0.0	79.6	20.4	1.5
1	2.0	0.122	0.020	0.112	0.033	2.7	82.2	15.1	7.4
2	2.0	0.123	0.020	0.111	0.033	2.7	82.0	15.3	7.3

Table E.11: H040L - Horizontal longitudinal configuration, half width. n=0.79

Test	$T[s]$	$H_{in}[m]$	$H_{r1}[m]$	$H_T[m]$	$H_{r2}[m]$	$C_{r1}^2[\%]$	$C_T^2[\%]$	$C_{diss}^2[\%]$	$C_{r2}^2[\%]$
1	1.0	0.128	0.028	0.076	0.001	4.9	35.7	59.4	0.0
2	1.0	0.128	0.028	0.076	0.000	4.8	35.4	59.8	0.0
1	1.13	0.131	0.022	0.086	0.007	2.9	42.8	54.3	0.3
2	1.13	0.131	0.022	0.086	0.007	2.8	42.7	54.5	0.3
1	1.25	0.128	0.031	0.090	0.010	5.8	49.5	44.7	0.6
2	1.25	0.128	0.030	0.090	0.010	5.7	49.4	45.0	0.7
1	1.50	0.125	0.024	0.093	0.014	3.7	54.8	41.5	1.3
2	1.50	0.125	0.024	0.093	0.014	3.8	55.0	41.2	1.2
1	2.0	0.123	0.021	0.085	0.026	3.0	47.3	49.7	4.5
2	2.0	0.123	0.022	0.084	0.026	3.1	46.9	50.0	4.5

Table E.12: H040S - Horizontal staggered configuration, half width. n=0.82

Test	$T[s]$	$H_{in}[m]$	$H_{r1}[m]$	$H_T[m]$	$H_{r2}[m]$	$C_{r1}^2[\%]$	$C_T^2[\%]$	$C_{diss}^2[\%]$	$C_{r2}^2[\%]$
1	1.0	0.117	0.021	0.084	0.001	3.4	51.7	44.9	0.0
2	1.0	0.119	0.022	0.084	0.001	3.4	50.0	46.7	0.0
1	1.13	0.127	0.017	0.093	0.006	1.7	53.3	45.0	0.2
2	1.13	0.128	0.018	0.093	0.006	2.1	52.5	45.4	0.3
1	1.25	0.124	0.024	0.098	0.011	3.7	62.0	34.4	0.8
2	1.25	0.124	0.023	0.098	0.011	3.3	62.4	34.3	0.8
1	1.50	0.124	0.010	0.103	0.015	0.6	68.6	30.8	1.4
2	1.50	0.124	0.010	0.103	0.015	0.7	68.9	30.4	1.4
1	2.0	0.123	0.019	0.103	0.031	2.3	69.6	28.1	6.4
2	2.0	0.123	0.018	0.103	0.031	2.2	69.6	28.2	6.4

Table E.13: H076U064 - Horizontal uniform dense configuration, full width.  $n=0.64$ 

Test	$T[s]$	$H_{in}[m]$	$H_{r1}[m]$	$H_T[m]$	$H_{r2}[m]$	$C_{r1}^2[\%]$	$C_T^2[\%]$	$C_{diss}^2[\%]$	$C_{r2}^2[\%]$
1	1.0	0.123	0.023	0.044	0.002	3.5	12.8	83.7	0.0
2	1.0	0.122	0.020	0.044	0.002	2.8	12.8	84.4	0.0
1	1.13	0.129	0.024	0.051	0.004	3.4	15.6	81.0	0.1
2	1.13	0.129	0.023	0.051	0.004	3.3	15.6	81.1	0.1
1	1.25	0.127	0.034	0.056	0.008	7.2	19.7	73.1	0.4
2	1.25	0.126	0.034	0.056	0.008	7.3	20.2	72.5	0.4
1	1.50	0.122	0.037	0.069	0.011	9.4	32.2	58.4	0.8
2	1.50	0.122	0.038	0.069	0.011	9.6	32.4	58.0	0.8
1	2.0	0.120	0.042	0.071	0.023	12.5	35.1	52.4	3.6
2	2.0	0.120	0.043	0.071	0.023	12.7	35.3	52.2	3.7

Table E.14: H076U089 - Horizontal uniform open configuration, full width.  $n=0.89$ 

Test	$T[s]$	$H_{in}[m]$	$H_{r1}[m]$	$H_T[m]$	$H_{r2}[m]$	$C_{r1}^2[\%]$	$C_T^2[\%]$	$C_{diss}^2[\%]$	$C_{r2}^2[\%]$
1	1.0	0.120	0.005	0.088	0.001	0.2	53.1	46.7	0.0
2	1.0	0.119	0.005	0.088	0.001	0.2	54.6	45.2	0.0
1	1.13	0.123	0.001	0.095	0.005	0.0	59.0	41.0	0.2
2	1.13	0.123	0.001	0.095	0.005	0.0	59.5	40.5	0.2
1	1.25	0.124	0.009	0.099	0.010	0.5	63.3	36.2	0.6
2	1.25	0.124	0.008	0.099	0.010	0.5	63.7	35.8	0.6
1	1.50	0.120	0.006	0.105	0.016	0.3	76.3	23.4	1.7
2	1.50	0.120	0.006	0.105	0.015	0.3	76.0	23.7	1.6
1	2.0	0.120	0.015	0.107	0.032	1.5	78.7	19.8	7.2
2	2.0	0.121	0.015	0.107	0.032	1.5	78.7	19.8	7.2

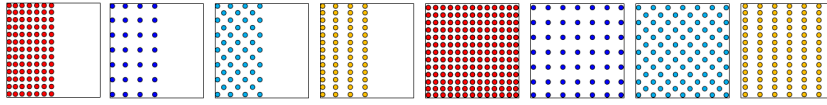
Table E.15: H076L - Horizontal longitudinal configuration, full width.  $n=0.79$ 

Test	$T[s]$	$H_{in}[m]$	$H_{r1}[m]$	$H_T[m]$	$H_{r2}[m]$	$C_{r1}^2[\%]$	$C_T^2[\%]$	$C_{diss}^2[\%]$	$C_{r2}^2[\%]$
1	1.0	0.125	0.013	0.059	0.001	1.1	21.8	77.1	0.0
2	1.0	0.121	0.013	0.058	0.002	1.1	23.1	75.8	0.0
1	1.13	0.131	0.017	0.067	0.004	1.6	26.4	72.0	0.1
2	1.13	0.130	0.017	0.068	0.005	1.6	26.9	71.5	0.1
1	1.25	0.127	0.023	0.074	0.010	3.4	33.7	62.9	0.6
2	1.25	0.127	0.024	0.074	0.010	3.5	34.0	62.5	0.6
1	1.50	0.121	0.025	0.084	0.013	4.2	47.8	48.0	1.1
2	1.50	0.121	0.025	0.084	0.013	4.4	48.0	47.7	1.1
1	2.0	0.120	0.025	0.077	0.024	4.2	40.9	54.9	4.2
2	2.0	0.120	0.024	0.077	0.024	4.2	41.1	54.7	4.2

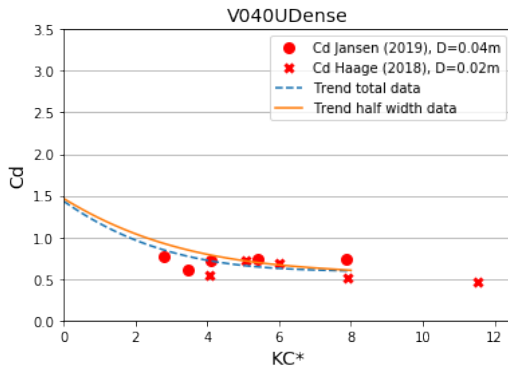
Table E.16: H076S - Horizontal staggered configuration, full width.  $n=0.82$ 

Test	$T[s]$	$H_{in}[m]$	$H_{r1}[m]$	$H_T[m]$	$H_{r2}[m]$	$C_{r1}^2[\%]$	$C_T^2[\%]$	$C_{diss}^2[\%]$	$C_{r2}^2[\%]$
1	1.0	0.119	0.009	0.069	0.001	0.6	34.1	65.3	0.0
2	1.0	0.122	0.011	0.070	0.001	0.9	32.6	66.6	0.0
1	1.13	0.126	0.007	0.078	0.004	0.4	38.8	60.9	0.1
2	1.13	0.125	0.008	0.078	0.004	0.5	39.0	60.5	0.1
1	1.25	0.122	0.019	0.086	0.009	2.4	49.6	48.0	0.5
2	1.25	0.121	0.018	0.085	0.009	2.3	50.0	47.7	0.6
1	1.50	0.120	0.013	0.095	0.014	1.1	61.7	37.1	1.3
2	1.50	0.121	0.013	0.095	0.014	1.2	61.5	37.3	1.3
1	2.0	0.120	0.016	0.096	0.030	1.8	64.8	33.5	6.1
2	2.0	0.120	0.016	0.096	0.030	1.8	64.5	33.6	6.1

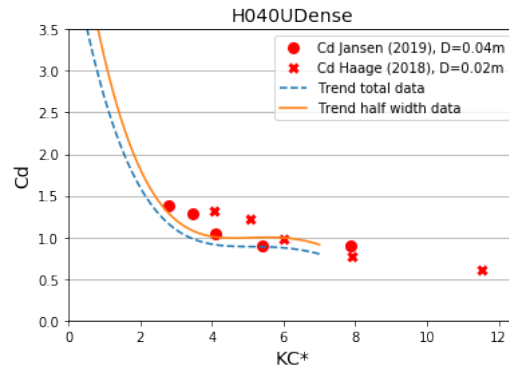
## E.2. Effect of diameter



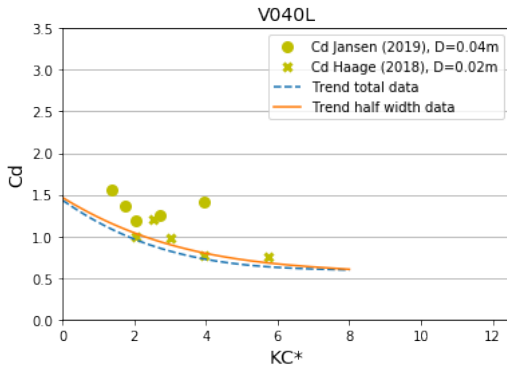
### Half width configurations



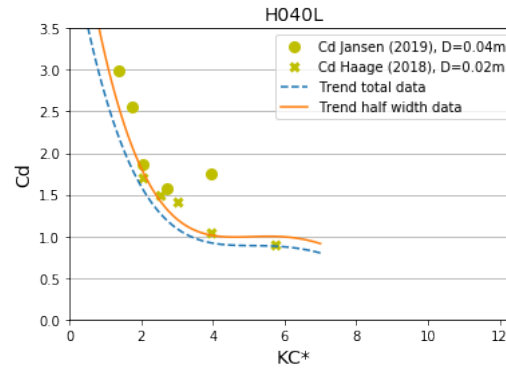
(a) Half width, vertical uniform dense.



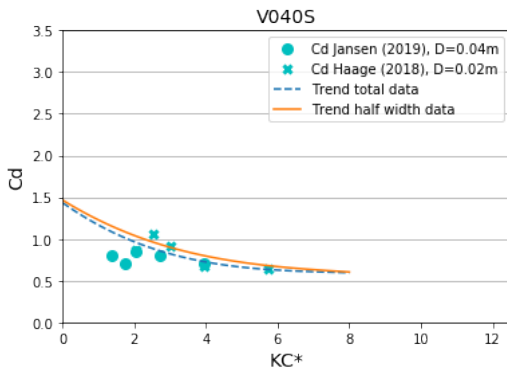
(b) Half width, horizontal uniform dense.



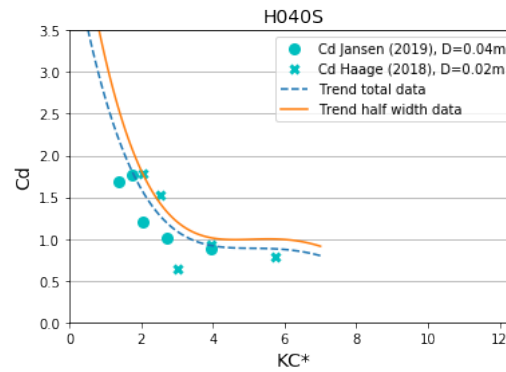
(c) Half width, vertical longitudinal.



(d) Half width, horizontal longitudinal.



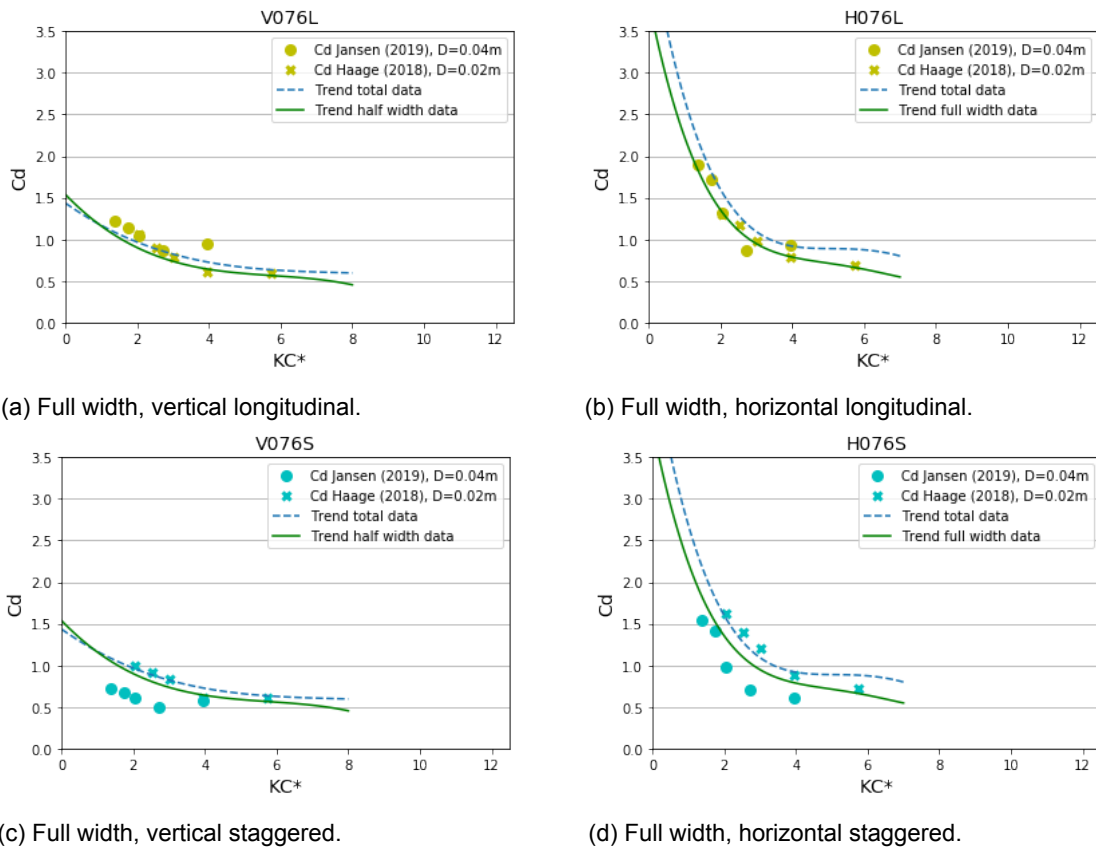
(e) Half width, vertical staggered.



(f) Half width, horizontal staggered.

Figure E.3: Comparison of the dimensionless drag coefficient for the half width configurations. The dashed line is based on the data of both the half and full width configurations. The solid line is based on the data of the half width configurations only.

**Full width configurations**



(a) Full width, vertical longitudinal.

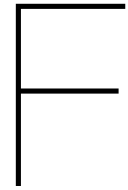
(b) Full width, horizontal longitudinal.

(c) Full width, vertical staggered.

(d) Full width, horizontal staggered.

Figure E.4: Comparison of the dimensionless drag coefficient for the full width configurations. The dashed line is based on the data of both the half and full width configurations. The solid line is based on the data of the half width configurations only.





## Approach with two methods

### F.1. Method 1 - Calibration from dissipation

Method 1 is based on the calculated energy dissipation obtained from the wave gauges in front and behind the model. From the wave gauge signals, the incoming, reflected and transmitted wave height is known. The dissipated energy is calculated with:

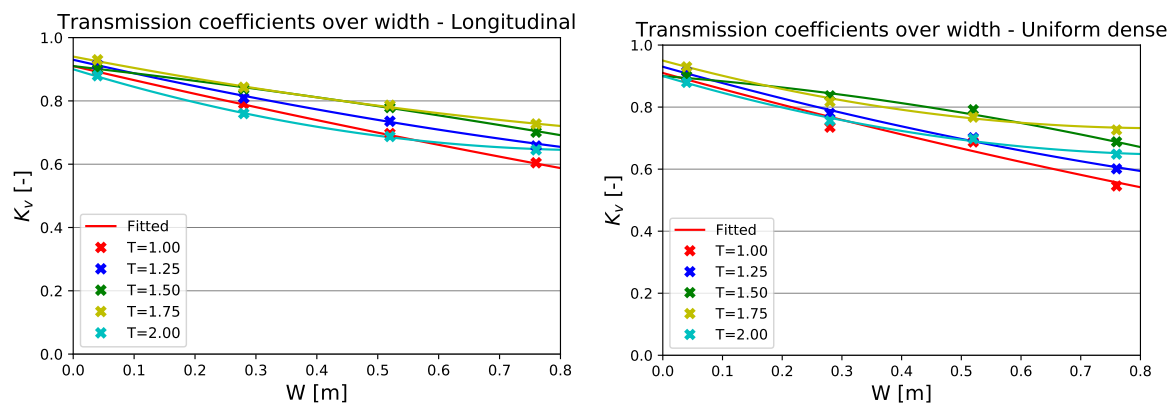
$$E_{diss} = E_i - E_r - E_t \quad (F.1)$$

and

$$E = \frac{1}{8} \rho g H^2 \quad (F.2)$$

The amplification factor ( $UF$ ) is then determined according to the following steps:

1. A profile for the wave height decay in the structure is assumed, based on the transmissions coefficient ( $K_v$ ). From increasing the width, this coefficient is know for 4 point over width. The total profile is obtained by fitting a line through these points for each wave case (See Figure 1). The wave height is obtained by multiplying  $K_v$  with the incoming wave height.



(a) Longitudinal configurations.

(b) Uniform dense configurations.

Figure F.1: Different measurement locations in the model; front, middle and back row.

2. The linear velocity is then calculated for each row in the model, based on the calculated local wave amplitude (see Figure F.2a).
3. The force coefficients  $C_d$  and  $C_m$  are assumed to be respectively 1.0 and 2.0 (theoretical values).

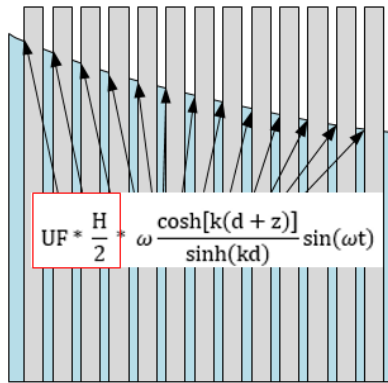
4. With the velocity and coefficients known, the dissipation of each row is calculated with:

$$\epsilon_D = -\frac{\partial(Ec_g)}{\partial x} \quad (\text{F.3})$$

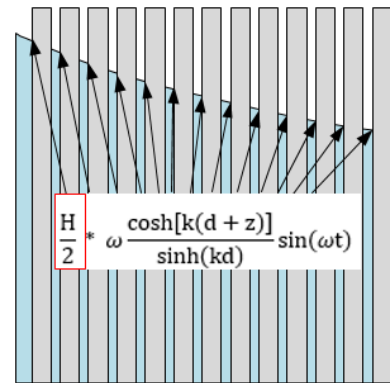
and

$$\epsilon_D = \frac{1}{T} \int_t^{t+T} \int_{-h}^{h+\eta} (F_x u) dz dt \quad (\text{F.4})$$

5. The amplification factor ( $UF$ ) for the linear velocity is calibrated to match the measured energy dissipation.
6. To check the reliability of the model, a cross-check is performed by calculating the force with the pair of force coefficients and the adapted velocity.



(a) Calculating the velocity inside the model for method 1.



(b) Calculating the velocity inside the model for method 2.

Figure F.2: Different methods to calculate the relevant velocity inside the model.

## F.2. Method 2 - Calibration from forces

Method 2 is based on the measured force signal on 1 element and linear wave theory. The force coefficients are determined according to the following steps:

1. The same profile for the wave height as in method 1 is assumed inside the structure.
2. Based on this wave height, the velocity according to linear wave theory is calculated for each row (see Figure F.2b).
3. With the measured force signal and calculated velocity signal, the force coefficients for the front, middle and back row are determined using the Least-square method (see Section 6.3.3).
4. To check the reliability of the model, a cross-check is performed by calculating the the energy dissipation with the calibrated pair of coefficients and the velocity of linear theory according to Formulae F.3 and F.4.



## Results experiments: Second set

### G.1. Assessing the methods for their own quantity

#### Method 1

Figure G.1 shows the calculated energy dissipation by method 1, plotted against the measured energy dissipation. The calibration is done for configuration 6 (longitudinal) and 7 (uniform dense), but the results are also plotted against configuration 10,11, 16 and 17. Those are the same configuration, but with the instruments on a different row. This causes the results to have a slight deviation for some values.

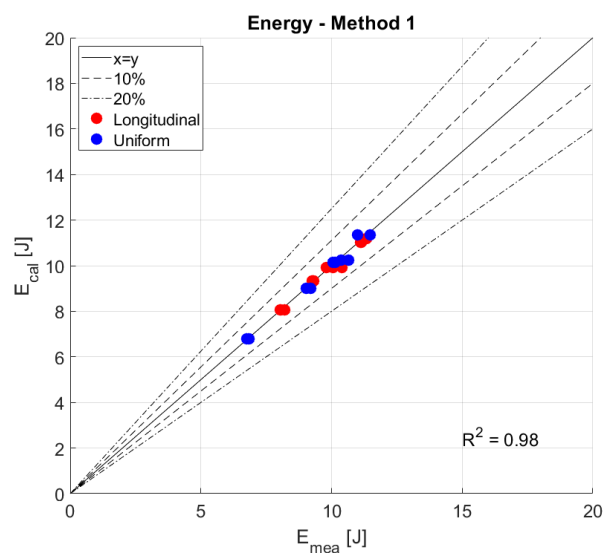


Figure G.1: Comparing the calculated energy dissipation with the measured energy dissipation for method 1.

### Method 2

For each pair of coefficients obtained with the calibration, the force signal is calculated. Figure G.2 shows the amplitude of the positive and negative calculated force, plotted against the measured force.

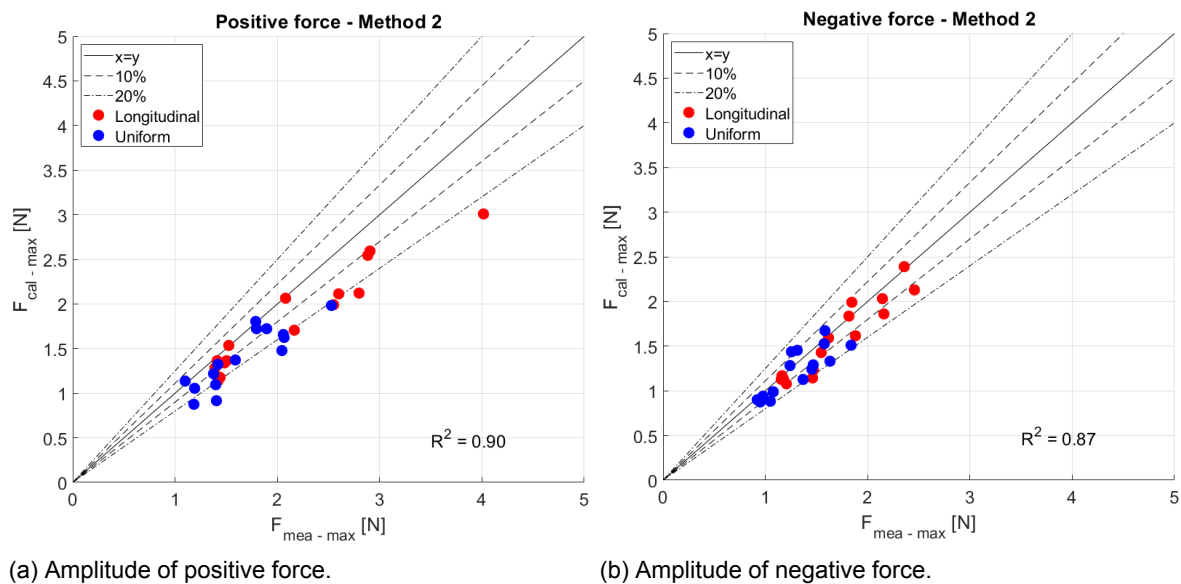


Figure G.2: Comparing the calculated force with the measured force for method 2.

The calculated forces do agree reasonably well with the measured force, as expected. The prediction is not perfect, as it for each time series is based on a constant pair of coefficient and a symmetric velocity signal, but the measured signal shows fluctuations.

## G.2. Force prediction method 1

Table G.1: Force prediction for the longitudinal configuration. Black is the measured force, red is the predicted force.

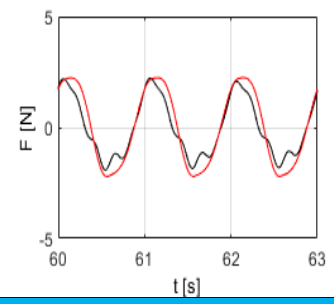
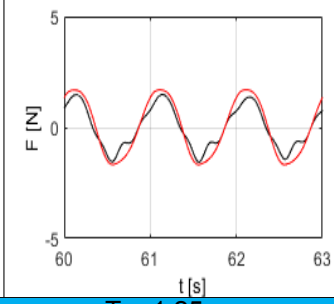
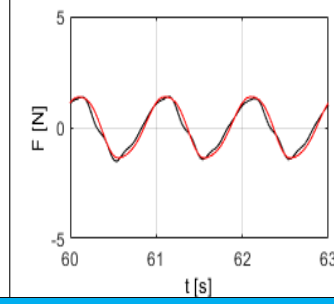
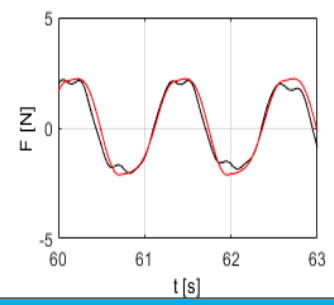
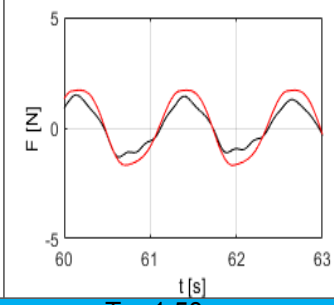
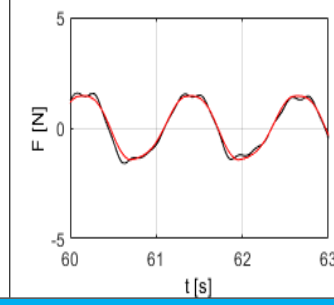
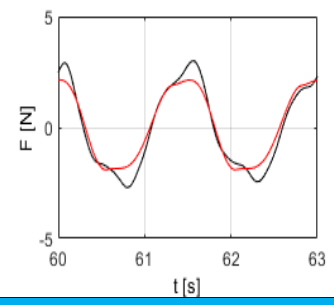
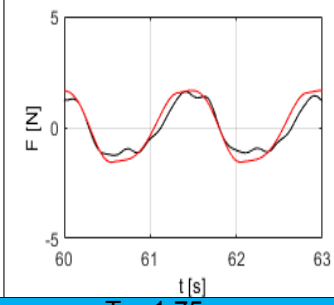
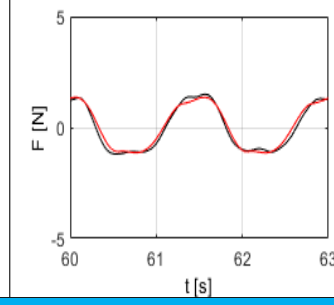
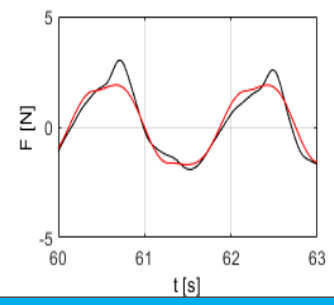
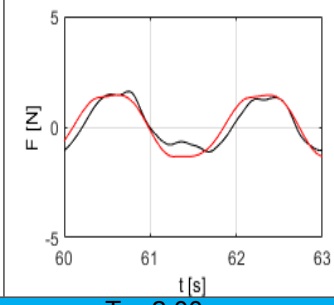
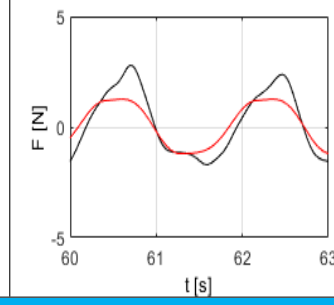
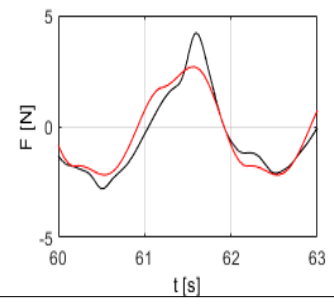
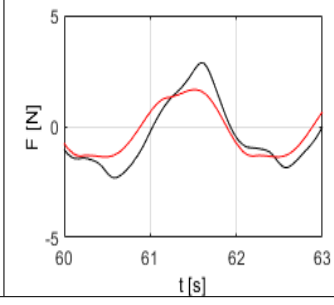
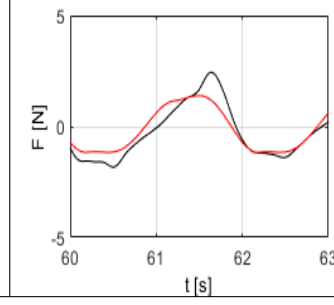
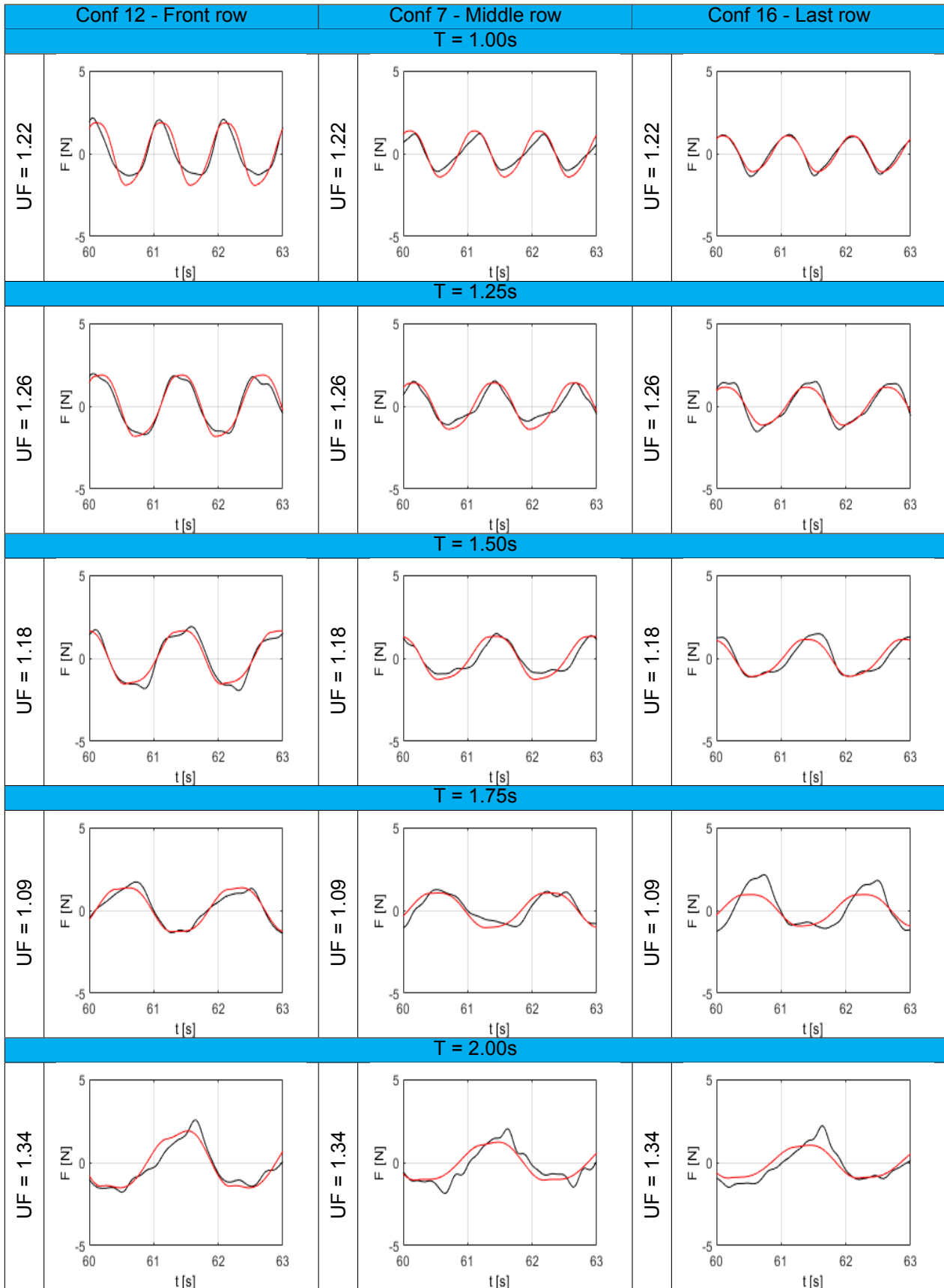
Conf 13 - Front row		Conf 6 - Middle row		Conf 17 - Last row	
<b>T = 1.00s</b>					
UF = 1.43		UF = 1.43		UF = 1.43	
<b>T = 1.25s</b>					
UF = 1.47		UF = 1.47		UF = 1.47	
<b>T = 1.50s</b>					
UF = 1.45		UF = 1.45		UF = 1.45	
<b>T = 1.75s</b>					
UF = 1.39		UF = 1.39		UF = 1.39	
<b>T = 2.00s</b>					
UF = 1.68		UF = 1.68		UF = 1.68	

Table G.2: Force prediction for the uniform dense configuration. Black is the measured force, red is the predicted force.





### G.3. Force prediction method 2

Table G.3: Force prediction for the longitudinal configuration - Method 2. Black is the measured force, red is the predicted force.

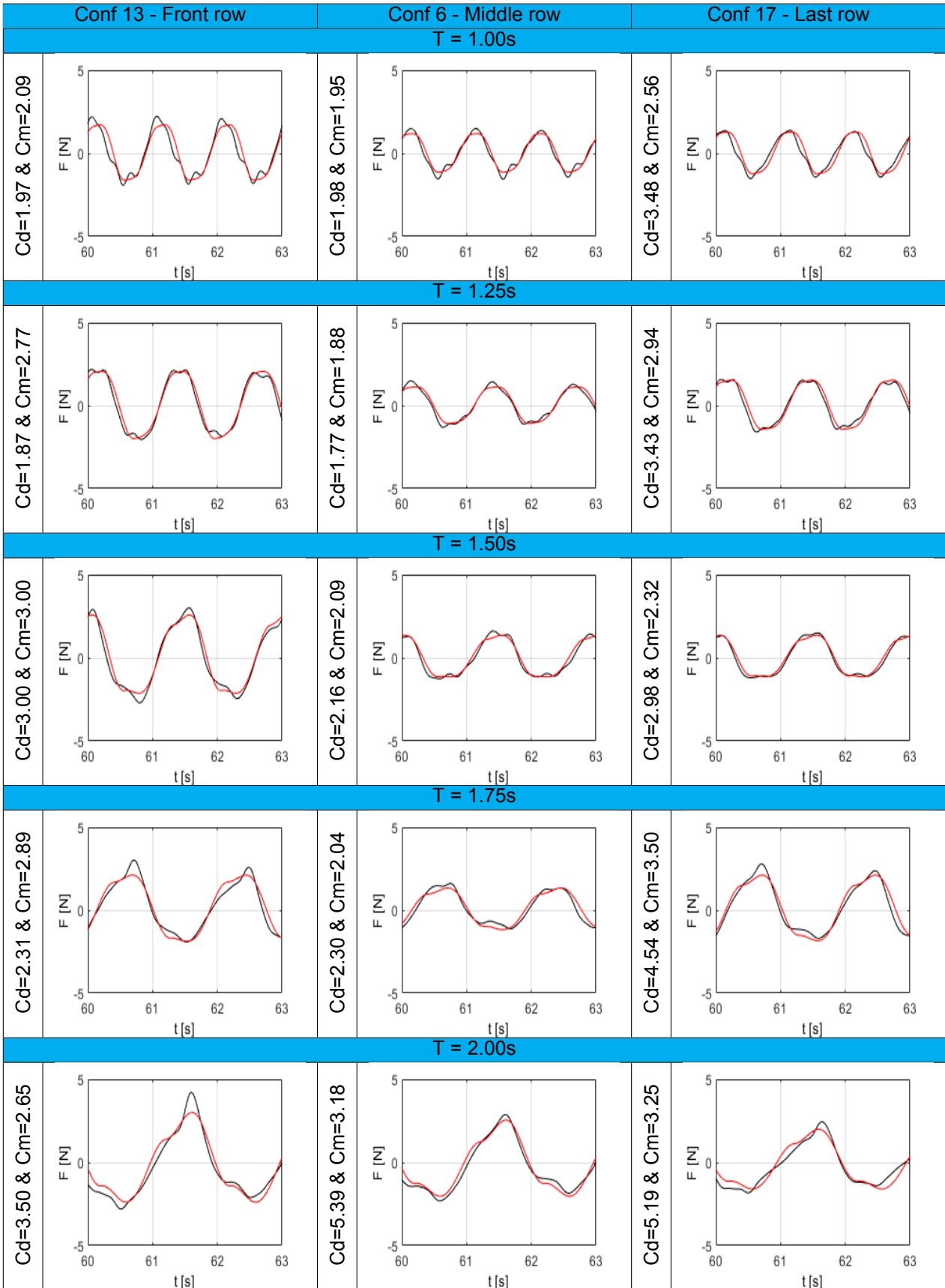
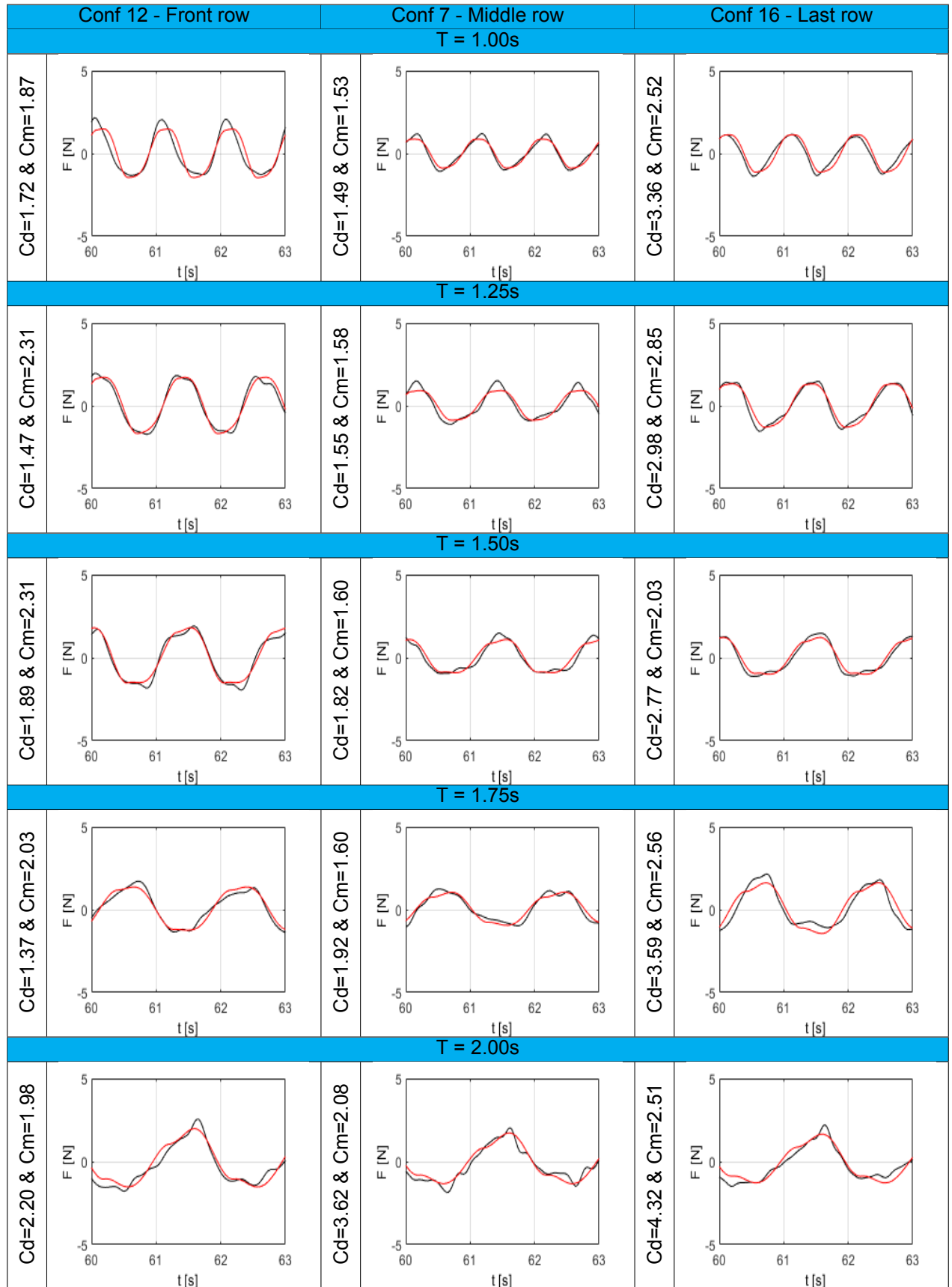
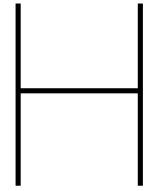


Table G.4: Force prediction for the uniform dense configuration. Black is the measured force, red is the predicted force.







## Analysis of experiments with only current

During the experiments, also tests with current-only conditions were performed for the configurations 1,2,3,6,7,10 and 11 (see Figure H.1). The current-only condition can be seen as a wave with an infinite period, resulting in an infinite  $KC$ -number. During these tests, the location of the ADV was the same as for the wave conditions, located at the front of the row. For the wave cases, the problem of asymmetry in the signal was overcome by considering only the negative part of the wave cycle. However, for a current condition this solution is not possible.

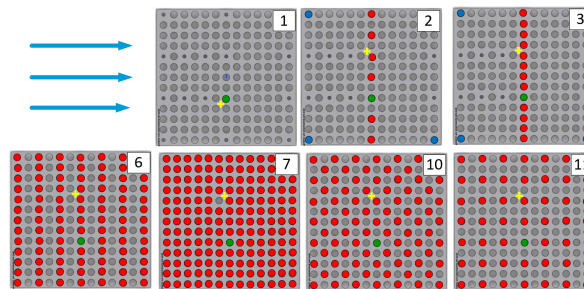


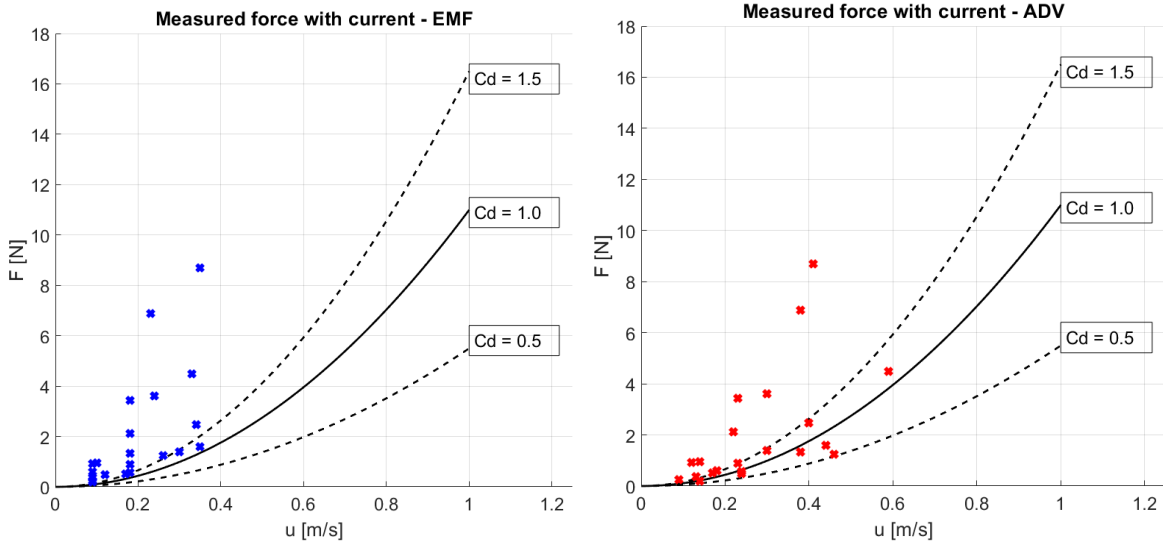
Figure H.1: Configurations which are tested with a current-only condition.

To get an idea of the amplification of the velocity inside the model, an approach comparable to method 1 (see Section F.1) is applied, calibrating on the drag coefficient instead of energy dissipation. As there is no inertia component in a current-only condition with a constant velocity, the force on the element is given by a simple exponential relation:

$$F_d = \frac{1}{2} C_d \rho D u |u| \quad (\text{H.1})$$

This relation is plotted in Figure H.2 for different values of  $C_d$ . As the theoretical value of the drag coefficient is close to  $C_d = 1.0$ , an amplification factor for the velocity can be calculated which makes the measured forces match the exponential relation best.

First, the measured force is plotted against the measured velocity by the EMF and ADV.

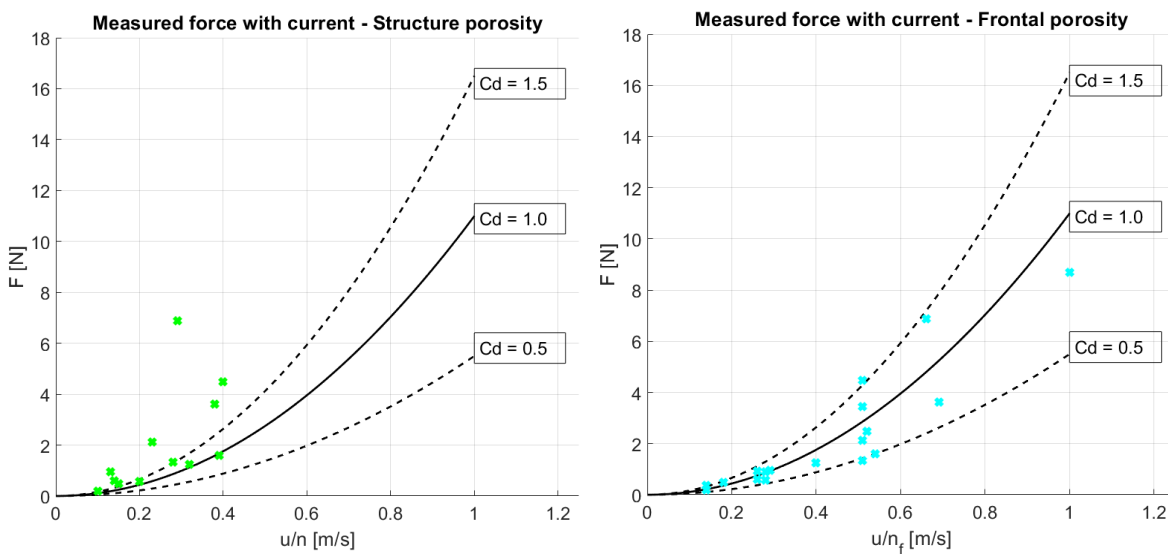


(a) Forces vs. velocities measured by EMF.

(b) Forces vs. velocities measured by ADV.

Figure H.2: The measured force plotted against the velocities measured by the instruments. The plot also shows the exponential relation between the force and velocities for different values of the drag coefficient.

Using the measured velocities of the EMF results in drag coefficients that too high for almost all wave cases. The use of the velocities measured by the ADV result in a better approximation for some wave cases, but still contains large values for  $C_d$ . Next, the amplification factors based on structure porosity and frontal porosity of Section 8.2 are used. For this calculation, the velocity measured by the EMF is taken as the undisturbed velocity.



(a) Velocities measured by EMF, amplified with a factor for the structure porosity.

(b) Velocities measured by EMF, amplified with a factor for the frontal porosity.

Figure H.3: The measured force plotted against the undisturbed velocity measured by the EMF, multiplied by an amplification factor. The plot also shows the exponential relation between the force and velocities for different values of the drag coefficient.

Figure H.3a shows the results when the velocity is based on the structure porosity. The results show hardly any improvement in relation the velocities of the ADV.

However, using the frontal porosity results in a large improvement. The results still show a large spread, but all fall within a drag coefficient range from  $C_d = 0.5 - 1.5$ . As during the

experiments no adaptations were done to create a smooth inflow, it resulted in a turbulent flow. This caused some fluctuations in the measured force and velocity signals. However, for the calculations an average value over time is used, which can cause the spread in the results. From this, the conclusion can be drawn that force on element in a current is related to the undisturbed velocity times a factor based on the frontal porosity.